Title	Fiber-laser-based stimulated-Raman spectral microscopy
Author(s)	能勢, 啓輔
Citation	大阪大学, 2015, 博士論文
Version Type	VoR
URL	https://doi.org/10.18910/52136
rights	
Note	

Doctoral Dissertation

Fiber-laser-based stimulated-Raman spectral microscopy

Keisuke Nose

January 2015

Department of Material and Life Science

Graduate School of Engineering,

Osaka University

Table of Contents

Chapter 4 Fiber-laser-based stimulated Raman scattering (FL-SRS) microscopy with shot-noise limited sensitivity 49

Chapter 5 Development of FL-SRS spectral microscopy 58

Chapter 6 Conclusion 73

Chapter 1

Introduction

In this chapter, the research background for the development of the label-free imaging techniques is described. Current techniques for biological imaging, their significant features, and technical issues are introduced. Raman microscopy, a promising technology for realizing label-free imaging, is introduced. Coherent Raman scattering (CRS) microscopy with coherent anti-Stokes Raman scattering (CARS) and stimulated Raman scattering (SRS) is introduced as a technique that overcomes the limitation of conventional Raman microscopy. The advantages of SRS microscopy and technical issues for improving its practicality are discussed. The objectives of this thesis, i.e., development of fiber-laser-based SRS (FL-SRS) microscopy, are described.

1.1. The research background of label-free imaging

Microscopic imaging is indispensable technique in medicine and biology. In the medical field, diseased tissues are observed and discriminated from normal tissues under an optical microscope. Observed images are then used to arrive at a diagnosis. In cell biology, microscopic imaging is crucial for investigating the kinetics of organelles and single molecules.

Biological specimens, however, are typically so transparent that observing them by basic optical transmission microscopy is difficult. To enhance the image contrast, several techniques are developed, e.g., phase-contrast microscopy and differential interference contrast microscopy. These techniques, however, only emphasize the outline of the samples. Consequently, these techniques cannot discriminate specific constituents in the specimens.

To observe a specific region of samples, cells and tissues are marked with dyes or probe molecules. In pathology and biology, staining based on the introduction of a class-specific dye (e.g., dye for DNA, proteins, lipids, or specific antibodies) is often used. The stained samples are viewed under a transmission optical microscope. In cell and

molecular biology, fluorescent proteins such as a green fluorescent protein are frequently used for labeling. Such proteins are introduced into organisms or cells by transgenic operation or injection operation. Linking of fluorescent proteins to target proteins enable highly specific labeling. The fluorescent proteins fluoresce when ultraviolet or visible light irradiates the sample. Fluorescence detection is so sensitive that it allows observation of even a single molecule.

However, there are remaining issues in staining and labeling techniques. Staining takes at least several tens of minutes to conduct a series of preprocesses. Since some dyes are toxic to cells, they are not always suited for observation of living samples in vivo. Labeling with fluorescent proteins also requires several preprocesses, and labeling affects its protein dynamics. Because of these issues, there is a potential need for the development of label-free imaging techniques.

1.2. Label-free imaging using Raman scattering

Generation of molecule-specific optical signals from unlabeled biological samples is possible through Raman scattering [1], which is an interaction between an electric field and molecular vibrations. Figure 1.1(a) schematically illustrates Raman scattering. When a light wave propagates in a dielectric material, the material becomes polarized. When the polarization varies with the molecular vibration, radiation from the polarization involves different frequency components reflecting molecular vibration. By analyzing the scattering spectrum, we can obtain molecular information. Figure 1.1(b) shows a schematic of the scattering spectrum. The higher-frequency component is called anti-Stokes scattering, and the lower one is called Stokes scattering. By measuring the scattering spectra, we can obtain quantitative molecular information about the sample without using any labeling techniques.

(a)

incident light
(ω_in)

ω_v

scattered light
($\omega_\text{in}, \omega_\text{S}, \omega_\text{AS}$)

(b)

ω_v

ω

ω_S ω_in ω_AS
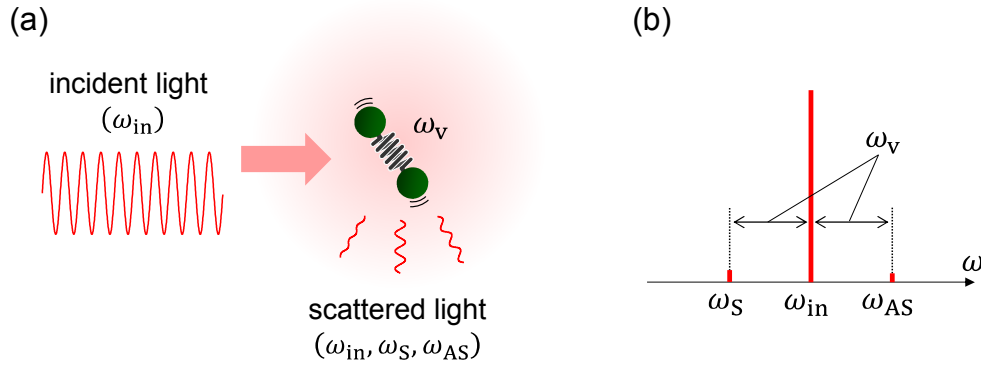
Fig. 1.1. Schematic of spontaneous Raman scattering. (a) When a molecule is Raman active, radiation from the molecule includes different frequency components. (b) The frequency shift from the incident, ω_in, matches the molecular vibrational frequency, ω_v. Blue-shifted light and red-shifted light comprise anti-Stokes scattering (ω_AS) and Stokes scattering (ω_S), respectively.

Raman microscopy, in which a microscope detects Raman scattering, realizes label-free biological imaging and molecular specificity based on vibrational spectroscopy [2, 3]. Figure 1.2 depicts the basic scheme in Raman microscopy in which a monochromatic laser beam is used for excitation of Raman scattering. A microscope objective focuses a laser beam to illuminate the sample and Raman scattering subsequently occurs at the focus. The scattering spectrum (typically Stokes scattering) is analyzed by a spectrometer. Images are taken by scanning the sample position with respect to the focus of the laser beam. A Raman image is reconstructed by assigning the spectral intensity at a specific Raman shift to the pixel intensity such that the image reflects the distribution map of molecules of interest. The main drawback of Raman microscopy is long acquisition time (several tens of minutes per image) due to the very weak scattering intensity. Although several groups have improved the illumination method to shorten its acquisition time [4, 5], further improvement of the imaging speed is still required.

ω_in

OL

ω_S

Spectrometer

F
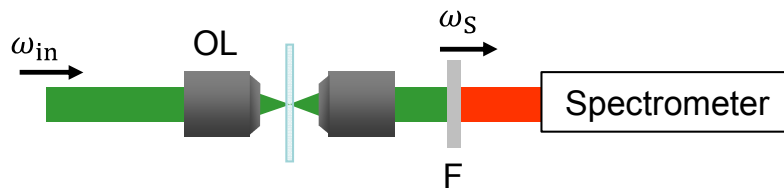
Fig. 1.2. Basic configuration of spontaneous Raman microscopy. OL: objective lens, F: optical filter.

1.3. Signal enhancement by coherent Raman scattering

CRS, a nonlinear optical effect [6], allows observation of intense Raman scattering. For clarity, ordinary Raman scattering is hereafter referred to as spontaneous Raman scattering. Figure 1.3 shows the relation between the input and output spectra with CRS. A distinct difference between CRS and spontaneous Raman scattering is that CRS uses two-color laser beams instead of a single monochromatic laser beam. Conventionally, the higher frequency beam is called "*pump*" and the other is called "*Stokes*," and their angular frequencies are denoted by ω_p and ω_S, respectively. When the difference frequency of the incident lights coincides with a molecular vibrational frequency, ω_v, a resonant oscillation occurs with the aid of the vibrational force originating from the two-color light waves. This leads to drastic enhancement of the interaction between the incident light and molecular vibration. It also results in a scattering spectrum that is different from that obtained with spontaneous Raman scattering (Fig. 1.3). CRS involves two phenomena. One is generation of new frequency components involving the molecular vibration. Its component having a sum frequency between the pump and the molecular vibration is known as CARS. Its other component, which has a difference frequency between the Stokes and the molecular vibration, is known as coherent Stokes Raman scattering (CSRS). The other phenomenon is energy transfer from the pump to the Stokes. As a result, the energy of Stokes increases and that of the pump decreases. These effects are known as stimulated Raman gain (SRG) and stimulated Raman loss (SRL), respectively. Together, both phenomena are called SRS.

Fig. 1.3. CRS. Pump and Stokes lights simultaneously irradiates molecules. When the difference frequency $\left(\omega_p - \omega_S\right)$ matches the molecular vibrational frequency ω_v, Raman scattering is drastically enhanced because of coherent interaction between the light and molecules. CSRS, CARS, and SRS subsequently occur.

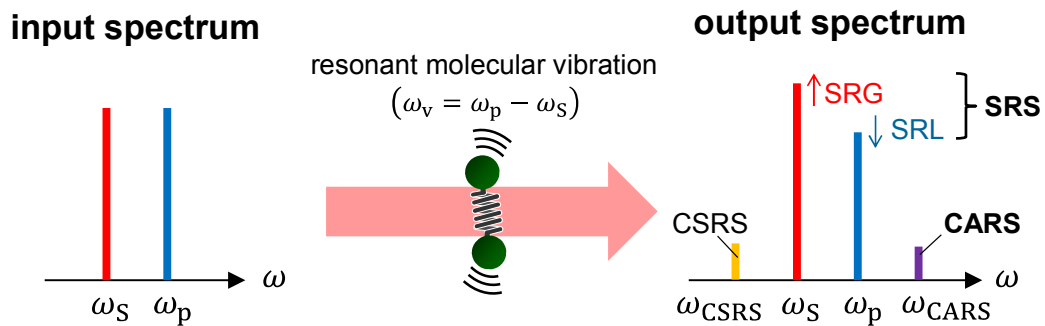To overcome the limitation of sensitivity in spontaneous Raman microscopy, CARS has been employed in microscopy [7–9]. Here, ultrashort pulses are used to effectively induce nonlinear Raman scattering. The basic configuration of CARS microscopy is illustrated in Fig. 1.4. Synchronized two-color pulses are tightly focused in the sample by a microscope objective. When the difference frequency matches ω_v at the focus, a CARS signal is generated and measured simultaneously with a photomultiplier tube (PMT) or with a cooled charge-coupled device. Since the CARS intensity is several orders of magnitude larger than that of spontaneous Raman scattering, this technique is suited for high-speed imaging. Indeed, CARS microscopy can increase the imaging speed to video rates [10, 11]. Furthermore, since CRS is nonlinear interaction, CARS occurs only at the focus, offering three dimensional resolution in space, as well as two-photon excitation microscopy [12]. However, the CARS signal includes nonresonant background in principle, leading to deterioration of the image contrast. Furthermore, nonresonant background distorts the vibrational spectrum. As a result, weak Raman peaks may be hidden near strong Raman peaks. Additionally, the CARS signal is proportional to the square of the molecular concentration because the CARS signal is the square of the Raman scattering component at a frequency of ω_{CARS}. Thus, straightforward analysis of a CARS image is difficult. In the last decade, much effort has been spent to solve this problem of nonresonant background. The reported techniques, however, increase the complexity of the experimental setup or of postanalysis [13–17].
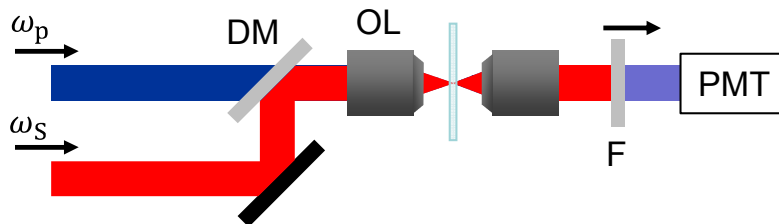
Fig. 1.4. Basic configuration of CARS microscopy. DM: dichroic mirror, OL: objective lens, F: short pass filter, PMT: photomultiplier.

To circumvent the issue of CARS microscopy with nonresonant background, SRS microscopy has been recently and consecutively reported by different groups [18–21]. The basic configuration of SRS microscopy is described in Fig. 1.5. SRS microscopy

also uses pump and Stokes pulses. However, Stokes pulses are amplitude-modulated before introducing them to a microscope. The pulses are then combined on a dichroic mirror and focused in the sample through a microscope. When SRS occurs at the focus, the amplitude modulation is transferred to the other pulses. Such modulation transfer is detected by a photodetector followed by a lock-in amplifier. SRS microscopy offers three dimensional resolution in space as well as CARS microscopy. Comparing to CARS microscopy, SRS microscopy is advantageous for the interpretation of the image contrast because SRS signal is proportional to the molecular concentration due to the heterodyne detection of the amplitude change of the incident lights. Furthermore, the signal-to-noise ratio of SRS is comparable to that of CARS when the shot-noise-limited sensitivity is achieved [20]. Indeed, video-rate SRS imaging with quiet laser sources has been reported [22]. In this manner, SRS microscopy would be a key technology for label-free biological imaging.
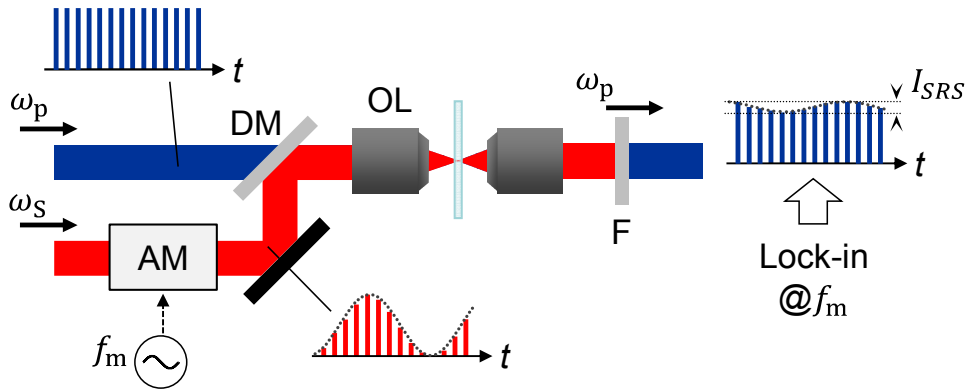
Fig. 1.5. Basic configuration of SRS microscopy. AM: amplitude modulator, DM: dichroic mirror, OL: objective lens, F: Stokes cut filter.

1.4. Technical issues of stimulated Raman microscopy

As described above, SRS microscopy is a powerful technique for label-free biomedical imaging with high quantitativity, high sensitivity, and molecular specificity. To use in practice, there are following two main issues with the technique that need to be solved.

I. Development of a microscope system that is more practical

In clinical use, it is important to develop a handheld microscope system for intraoperative diagnosis instead of ordinary optical microscope. Moreover, portability of the microscope system is desirable for chemical and biological analyses in the field and medical treatment especially for personalized therapy. One of the key developments addressing this issue in SRS microscopy is the laser source.

The laser source in SRS microscopy has the following major requirements:

     i.   Pulse duration of several picoseconds (corresponding to a spectral width of ~4 cm^{-1})

     ii.   High average power (>100 mW for high-speed imaging)

     iii.   Tight synchronization of two-color pulses

     iv.   Shot-noise-limited intensity noise

To satisfy the above requirements, most studies on SRS microscopy have employed an optical parametric oscillator and solid-state lasers such as Ti:sapphire laser [18–28]. Such lasers have advantages such as high average power (several watts) and ultralow intensity noise, which is almost shot-noise limited. On the other hand, there are practical problems such as cost (typically $ 100,000), size (~1 m^2), and difficulty of use. Such solid-state laser-based system hinders the wide spread use of SRS microscopy.

From a practical perspective, fiber lasers (FLs) are an attractive replacement for solid-state lasers [29–31]. The advantages of FLs are low cost, small size, and turnkey operation. There is no need for optical alignment as the laser cavity consists of optical fibers. By employing polarization-maintaining components, FLs can be isolated from mechanical perturbations. In fact, several types of microscopic techniques based on FLs have been developed [32–36]. Figure 1.6 shows a typical solid-state laser and a typical FL to illustrate their difference in size. Table 1.1 compares features of these lasers. If solid-state lasers were replaced by FLs, SRS microscopy would be more attractive and useful tool for non-professions such as biologists and physicians.

To use FLs in SRS microscopy, we need to pay attention to their intensity noise. The output powers of typical FL oscillators are much lower than those required for SRS microscopy. Thus, optical amplification is needed. Such amplification adds a large

amplifier noise to FL pulses, limiting the sensitivity of SRS microscopy. On the other hand, an SRS microscope based on solid-state lasers offers sensitivity that is nearly shot-noise-limited because of its quietness. Thus, it is crucial that the effect of the intensity noise is suppressed down to the shot-noise limit to replace solid-state lasers with FLs. The effect of optical noise can be mitigated by the technique of balanced detection. In microscopy applications, however, such technique can suffer from intensity imbalance due to variation of transmittance in the sample [29–31]. This point will be discussed in detail in Section 3.1.
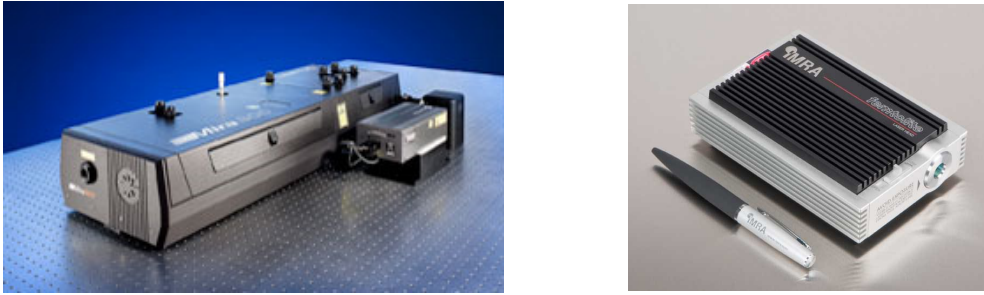
Fig. 1.6. Ultrafast laser sources. The left image shows a typical Ti:sapphire laser oscillator (©Coherent, Inc.) on an optical bench with a size of around several square meters. The right image shows a typical FL oscillator (©IMRA America, Inc.).

Table 1.1. Comparison of the features of solid-state lasers and FLs.

Laser source	Solid-state laser	Fiber laser
Power	~W	~10 mW
SNR	Good (shot noise limited)	Medium
Cost	~$100,000	~$10,000
Size	Large (tabletop)	Small (palmtop)
Handling	Difficult	Turn-key
Robustness	Low	High

II. Further enhancement of molecular specificity

SRS microscopy has limitations in terms of molecular specificity. An SRS image reflects a single vibrational frequency. Although different molecules may have different vibrational spectra, they often overlap with each other. Such molecules cannot always be discriminated from a single SRS image. Spectral imaging is important in discriminating such molecules. SRS spectral images are taken by changing the difference frequency (ω_n) of the incident pulses (i.e., pump or Stokes pulses) as shown in Fig. 1.7. We can obtain a multi-color image, reflecting discriminated molecules and/or specific structures in cells, by superposition of the images obtained at different wavenumbers [24-27]. Combining with spectrum analysis technique further enhances molecular specificity [37, 38]. For instance, such quasi-colored image offers the contrast similar to the conventional technique such as hematoxylin and eosin staining, which is the most popular technique for the tissue staining and giving diagnosis [37, 39]. In this manner, SRS spectral imaging is effective to enhance molecular specificity.

For SRS spectral imaging, wide-wavelength tunability of the laser source, for example ~300 cm^{-1} for covering CH stretching vibration region, which includes Raman peaks of the major constituents in tissue, is effective for achieving higher molecular specificity. It is important that the wavelength tunable source is free from wavelength-dependent group delay to avoid timing mismatch between the pump and Stokes pulses. Furthermore, it is also important to fast tunability, particularly, for observing the intracellular dynamics in living cells [40, 41] and intraoperative diagnosis [42]. Although several groups have proposed various techniques for SRS spectral microscopy, these systems employed solid state lasers. The development of the practical and wavelength-tunable laser, which satisfies above requirements, would make it possible to realize the practical and high-functional SRS microscope.
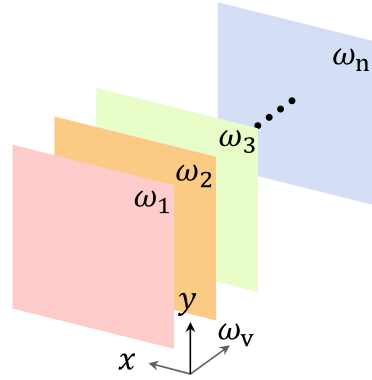
Fig. 1.7. SRS spectral imaging. Spectral images are obtained by changing the difference frequency between pump and Stokes.

1.5.   Objectives and construction of the thesis

This dissertation addresses the development of practical SRS spectral microscopy by using FL-based laser source. **Chapter 1** presents the research backgrounds and objectives. **Chapter 2** gives the fundamental theories for a better understanding of the thesis. To develop FL-based (FL-) SRS microscopy, reducing the effect of the intensity noise of FL pulses down to the shot-noise limit is very important. To address this, I propose and describe in **Chapter 3** a new type of balanced detection technique, "*collinear balanced detection* (CBD)." CBD instead of optical pulse is also applied to nonpolarized optical noise to show its generality. In **Chapter 4**, the sensitivity enhancement of FL-SRS microscopy by CBD is demonstrated. SRS spectral imaging by using the FL-SRS microscope is then demonstrated in **Chapter 5**, where an improved version of a fast tunable FL-based Stokes pulse source that extends the wavelength tunability is described. The performance of the FL-SRS spectral microscope is investigated through spectral imaging of polymers and living samples. This work is finally summarized in **Chapter 6**, where the outlook of SRS microscopy is also presented.

References

[1] C. V. Raman and K. S. Krishnan, *Nature* **121,** 501 (1928).

[2] G. J. Puppels, F. F. M. de Mul, C. Otto, J. Greve, M. Robert-Nicoud, D. J. Arndt-Jovin, and T. M. Jovin, *Nature* **347**, 301 (1990).

[3] G. J. Puppels, M. Grond, and J. Grave, *Appl. Spectrosc.* **47**, 1256 (1993).

[4] C. J. De Grauw, C. Otto, and J. Greve, *Appl. Spectrosco.* **51**, 1607 (1997).

[5] K. Hamada, K. Fujita, N. I. Smith, M. Kobayashi, Y. Inoue, S. Kawata, *J. Biomed. Opt.* **13**, 044027 (2008).

[6] R. W. Boyd, "*Nonlinear optics*" 3rd ed., Academic press (2008).

[7] M. D. Duncan, J. Reintjes, and T. J. Manuccia, *Opt. Lett.* **7**, 350 (1982).

[8] A. Zumbusch, G. R. Holtom, and X. S. Xie, *Phys. Rev. Lett.* **82**, 4142 (1999).

[9] M. Hashimoto, T. Araki, and S. Kawata, *Opt. Lett.* **25**, 1768 (2000).

[10] C. L. Evans, E. O. Potma, M. Puoris'haag, D. Cote, P. Lin, and X. S. Xie, *Proc. Natl. Acad. Sci.* **102**, 16807 (2005).

[11] T. Minamikawa, M. Hashimoto, K. Fujita, S. Kawata, and T. Araki, *Opt. Express* **17**, 9526 (2009).

[12] W. Denk, J. H. Strickler, and W. W. Webb, *Science* **248**, 4951 (1990).

[13] A. Volkmer, J.-X. Cheng, and X. S. Xie, *Phys. Rev. Lett.* **87**, 23901 (2001).

[14] J. -X. Cheng, L. D. Book, and X. S. Xie, *Opt. Lett.* **26**, 1341 (2001).

[15] C. L. Evans, E. O. Potma, and X. S. Xie, *Opt. Lett.* **29**, 2923 (2004).

[16] H. Kano and H. Hamaguchi, *Opt. Express* **13**, 1322 (2005).

[17] F. Ganikhanov, C. L. Evans, B. G. Saar, and X. S. Xie, *Opt. Lett.* **31**, 1872 (2006).

[18] E. Ploetz, S. Laimgruber, S. Berner, W. Zinth, and P. Gilch, *Appl. Phys. B* **87**, 389 (2007).

[19] C. W. Freudiger, W. Min, B. G. Saar, S. Lu, G. R. Holtom, C. He, J. C. Tsai, J. X. Kang, and X. S. Xie, *Science* **322**, 1857 (2008).

[20] Y. Ozeki, F. Dake, S. Kajiyama, K. Fukui, and K. Itoh, *Opt. Express* **17**, 3651 (2009).

[21] P. Nandakumar, A. Kovalev, and A. Volkmer, *N. J. Phys.* **11**, 033026 (2009).

[22] B. G. Saar, C. W. Freudiger, J. Reichman, C. M. Stanley, G. R. Holtom, and X. S. Xie, *Science* **330**, 1368 (2010).

[23] Y. Ozeki, W. Umemura, K. Sumimura, N. Nishizawa, K. Fukui, and K. Itoh, *Opt. Lett.* **37**, 431-433 (2012).

[24] F. -K. Lu, M. Ji, D. Fu, X. Ni, C. W. Freudiger, G. Holtom, and X. S. Xie, *Mol. Phys.* **110**, 1927 (2012).

[25] K. Wang, D. Zhang, K. Charan, M. N. Slipchenko, P. Wang, C. Xu, and J. X. Cheng, *J. Biophotonics* **6**, 815 (2013).

[26] D. Fu, G. Holtom, C. Freudiger, X. Zhang, and X. S. Xie, *J. Phys. Chem. B* **117**, 4634 (2013).

[27] L. Kong, M. Ji, G. R. Holtom, D. Fu, C. W. Freudiger, and X. S. Xie, *Opt. Lett.* **38**, 145 (2013).

[28] K. Seto, Y. Okuda, E. Tokunaga, and T. Kobayashi, *Rev. Sci. Instrum.* **84**, 083705 (2013).

[29] A. Gambetta, V. Kumar, G. Grancini, D. Polli, R. Ramponi, G. Cerullo, and M. Marangoni, *Opt. Lett.* **35**, 226 (2010).

[30] E. Molotokaite, V. Kumar, C. Manzoni, D. Polli, G. Cerullo, and M. Marangoni, *J. Raman Spectrosc.* **44**, 1385 (2013).

[31] C. W. Freudiger, W. Yang, G. R. Holtom, N. Peyghambarian, X. S. Xie, and K. Q. Kie, *Nat. Photonics* **8**, 153 (2014).

[32] N. G. Horton, K. Wang, D. Kobat, C. G. Clark, F. W. Wise, C. B. Schaffer, and C. Xu, *Nat. Photonics* **20**, 205 (2013).

[33] F. Ganikhanov, S. Carrasco, X. S. Xie, M. Katz, W. Seitz, and D. Kopf, *Opt. Lett.* **31**, 1292 (2006).

[34] E. R. Andresen, C. K. Nielsen, J. Thøgersen, and S. R. Keiding, *Opt. Express* **15**, 4848 (2007).

[35] A. C. Millard, P. W. Wiseman, D. N. Fittinghoff, K. R. Wilson, J. A. Squier, and M. Müller, *Appl. Opt.* **38**, 7393 (1999).

[36] C. Xu and F. W. Wise, *Nat. Photonics* **7**, 875 (2013).

[37] Y. Ozeki, W. Umemura, Y. Otsuka, S. Satoh, H. Hashimoto, K. Sumimura, N. Nishizawa, K. Fukui, and K. Itoh, *Nat. Photonics* **6**, 845 (2012).

[38] D. Zhang, P. Wang, M. N. Slipchenko, D. B-. Amotz, A. M. Weiner, and J. -X. Cheng, *Anal. Chem.* **85**, 98 (2013).

[39] C. W. Freudiger, R. Pfannl, D. A. Orringer, B. G. Saar, M. Ji, Q. Zeng, L. Ottoboni, W. Ying, C. Waeber, J. R. Sims, P. L. de Jager, O. Sagher, M. A. Philbert, X. Xu, S. Kesari, X. S. Xie, and G. S. Young, *Lab. Invest.* **92**, 1492 (2012).

[40] D. Fu, F. -K. Lu, X. Zhang, C. Freudiger, D. R. Pernik, G. Holtom, and X. S. Xie, *J. Am. Chem. Soc.* **134**, 3623 (2012).

[41] X. Zhang, M. B. Roeffaers, S. Basu, J. R. Daniele, D. Fu, C. W. Freudiger, G. R. Holtom, and X. S. Xie, *Chem. Phys. Chem.* **13** 1054 (2012).

[42] M. Ji, D. A. Orringer, C. W. Freudiger, S. Ramkissoon, X. Liu, D. Lau, A. J. Golby, I. Norton, M. Hayashi, N. Y. R. Agar, G. S. Young, C. Spino, S. Santagata, S. C-. Piragua, K. L. Ligon, O. Sagher, and X. S. Xie, *Sci. Transl. Med.* **5**, 201ra119 (2013).

Chapter 2

Fundamentals: optical interference and stimulated Raman microscopy

This chapter is dedicated to the theoretical foundations of the work presented in this thesis. I use the interference effect in the Fourier domain to enhance the sensitivity of practical stimulated Raman scattering (SRS) microscopy. The interference effect is important in the generation of optical pulses and in the mechanism of SRS effect. To better understand these effects, the interference effects between different-color waves in time and Fourier domains are explained. Unique features of optical pulses, such as high peak power and susceptibility to dispersion effect, are also introduced. The origins of linear and nonlinear Raman effects are then described by using the classical model of interaction between electric fields and molecules. After introduction of the basic theory of SRS microscopy, photodetection noises are discussed with respect to its sensitivity. I also describe how excess intensity noise hinders the application of practical laser sources to SRS microscopy.

2.1. Behavior of the superposition field of multicolor light waves

2.1.1. Optical beat

Superposition of light waves results in a change in its waveform, resulting in unique optical phenomena such as optical beat, pulse, and spectral fringe. Here, we consider the interference of two-color monochromatic light waves, i.e., generation of an optical beat or simply a beat. On the basis of the mechanism of beats, we shall be concerned with the mechanism of optical pulse, spectral interference, SRS, and laser excess intensity noise in the following sections.

To simply consider the quality of the interference, we assume a temporal evolution of a plane wave propagating along the z axis [1]. We denote an electric field of light E as follows:

$$E(z,t) = E_0 \cos(\omega t - \beta z - \phi),\qquad(2\text{-}1)$$

where t, E_0, β, and ϕ are the time, amplitude, propagation constant, and initial phase, respectively. We consider the interference of light waves at angular frequencies of ω_1 and ω_2. For simplicity, we investigate the time evolution of the following electric fields at a position where $z = 0$:

$$E_1(t) = E_0 \cos(\omega_1 t - \phi_1), \qquad (2\text{-}2)$$

$$E_2(t) = E_0 \cos(\omega_2 t - \phi_2). \qquad (2\text{-}3)$$

Assuming that these fields propagate with the same polarization states, we represent the superposition of these fields by

$$E = 2E_0 \cos\left[\frac{\Delta\omega}{2}t - \frac{\Delta\phi}{2}\right] \cos\left[\frac{(\omega_1 + \omega_2)}{2}t - \frac{(\phi_1 + \phi_2)}{2}\right], \qquad (2\text{-}4)$$

where $\Delta\omega = \omega_1 - \omega_2$ and $\Delta\phi = \phi_1 - \phi_2$. This equation implies that the carrier frequency of E is the average of the frequencies of E_1 and E_2 and that the envelope oscillates at $\Delta\omega/2$.

The optical intensity, I, is defined as the time average of the amount of energy that crosses a unit area perpendicular to the direction of the energy flow in unit time. For a plane wave, I is given by

$$I = \frac{nc\epsilon_0}{2}\langle E^2 \rangle, \qquad (2\text{-}5)$$

where n, c, and ϵ_0 are the refractive index, speed of light in vacuum, and vacuum permittivity, respectively. The intensity of the superposed field is thus obtained by substituting Eq. (2-4) into Eq. (2-5):

$$I \propto E_0^2[1 + \cos(\Delta\omega t - \Delta\phi)]. \qquad (2\text{-}6)$$

This equation shows that superposition of the two-color light waves creates a beat oscillating at the difference frequency. Figure 2.1 shows the relationship between the fundamental electric fields, the superposed field, and its intensity.
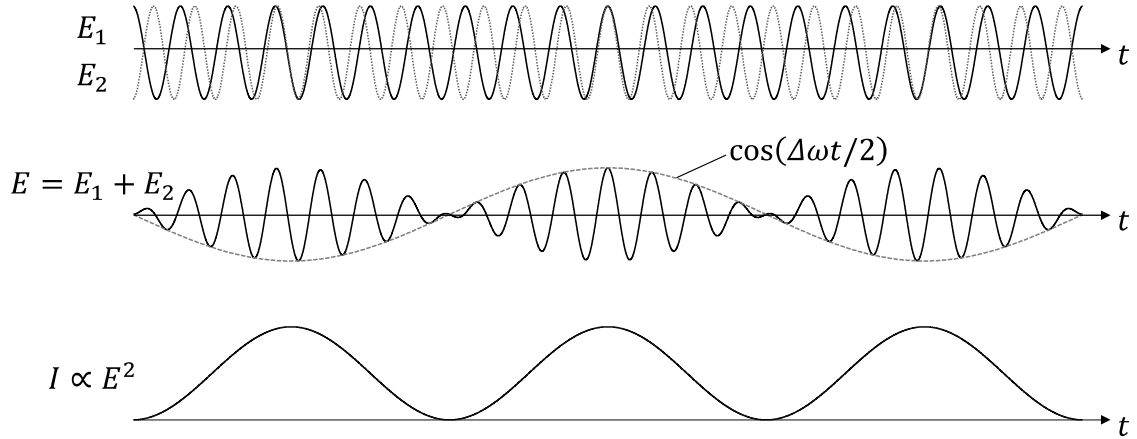
Fig. 2.1. Optical beat. Superposition of electric fields of light waves with slightly different frequencies generates a unique electric field, which is modulated by the half of the difference frequency of the incidents, $\Delta\omega/2$. Its intensity creates an optical beat note, which oscillates at the difference frequency, $\Delta\omega$.

2.1.2. Optical pulse

Here, we expand the principle of optical beat to the generation of optical pulses. The superposition of electric fields is given by

$$E = \sum^{n} E_i .$$

(2-7)

We assume that the electric fields have regularly discrete frequencies, as shown in Fig. 2.2(a). If their spectral phases are random, then superposition of these fields creates a random waveform that resembles Gaussian noise, as shown in Fig. 2.2(b). On the other hand, when their phases are zero, the peaks of sinusoidal waves constructively interfere while the other parts destructively interfere. This interference creates an optical pulse train (Fig. 2.2(c)). This is exactly the principle of generation of ultrashort pulses from mode-locked lasers [2]. Here, many longitudinal modes are simultaneously amplified and radiated with fixed relative phases, although very few longitudinal modes are radiated from a continuous wave laser oscillator.

In contrast to continuous waves, optical pulses show unique optical properties. Because of concentration of optical energy in a short duration due to constructive interference, optical pulses have strong peak power and a moderate average power. This property is advantageous for producing nonlinear optical effects, which are significant when the optical power is high. Assuming rectangular pulses, the peak power (P), the

16

optical power (I), the repetition rate (f_rep) and the pulse duration (Δt) are related to each other by the following equation:

$$P = \frac{I}{f_\text{rep} \cdot \Delta t}.$$ (2-8)

As for the optical energy per pulse,

$$E_\text{pulse} = P \cdot \Delta t.$$ (2-9)

To estimate how intense the peak power is, we assume that the average power, the repetition rate, and the pulse duration are 10 mW, 50 MHz, and 1 ps, respectively. The peak power and pulse energy are found to be 200 W and 0.2 nJ, respectively. The instantaneous optical power is four orders of magnitude larger than its average power, indicating the effectiveness of the optical pulse for producing the nonlinear optical effect. Furthermore, use of relatively low pulse energy avoids photodamage of irradiated materials.

As shown in Eq. (2-8), a much shorter pulse duration is intuitively more effective for nonlinear signal generation. However, such duration results in broad bandwidth, according to the time–bandwidth product, which indicates the relation of minimum pulse width and its bandwidth (described in Appendix C in detail). Therefore, in SRS microscopy, a much shorter pulse results in a lower spectral resolution. Typically, the resolution bandwidth in Raman microscopy is required to be as small as a few wavenumbers, corresponding to a pulse duration of a few picoseconds.
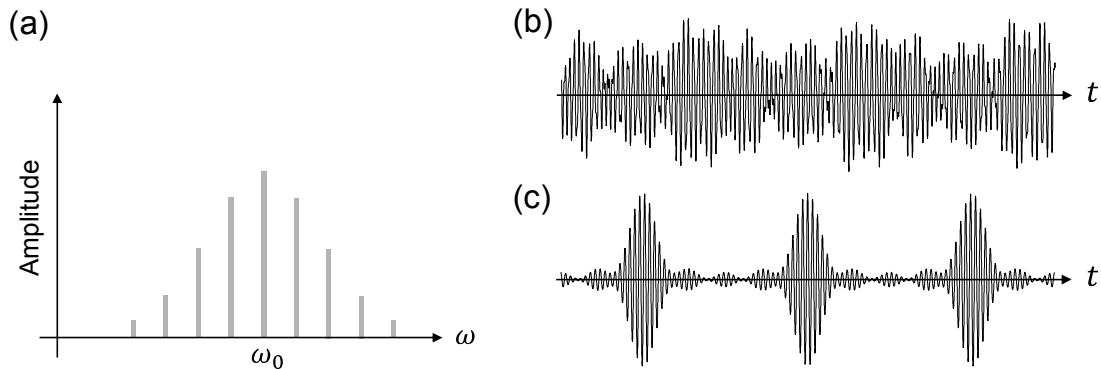

Fig. 2.2. Interference between multicolor light waves. When multicolor light waves, whose spectra are shown in (a), are superposed with random phases, the resultant electric field resembles Gaussian noise (b). When the initial phases are zero, superposition results in an optical pulse train (c).

2.1.3. Effect of pulse propagation in dispersive medium

When an optical pulse propagates in a dispersive medium (e.g., air, glass, and optical fiber), the pulse experiences material dispersion, which causes pulse broadening. This leads to a decrease in instantaneous optical power, causing deterioration of nonlinear signal generation, including not only SRS but also high harmonic generation for wavelength conversion. To address this issue, the influence of the dispersion effect on light waves is explained, and then dispersion compensation techniques are briefly introduced here.

When a monochromatic light wave propagates in dispersive material with a propagation constant β, the light field experiences phase delay by as much as βz, as described in Eq. (2-1) and shown in Fig. 2.3(a). If the refractive index (n) of the material has dependence of ω, we then expand β in terms of an optical frequency of ω around a frequency of ω_0 [3]:

$$\beta(\omega) = n(\omega)\frac{\omega}{c} = \beta_0 + \beta_1(\omega - \omega_0) + \frac{\beta_2}{2!}(\omega - \omega_0)^2 + \cdots, \qquad (2\text{-}10)$$

where

$$\beta_m = \frac{d^m\beta}{d\omega^m}\bigg|_{\omega=\omega_0} \quad (m = 0,1,2\ldots). \qquad (2\text{-}11)$$

The parameters β_0 and β_1 are related to the phase velocity (v_p) and the group velocity (v_g) as follows:

$$\frac{\beta_0}{\omega_0} = \frac{1}{v_p}, \qquad (2\text{-}12)$$

$$\beta_1 = \frac{d\beta}{d\omega}\bigg|_{\omega=\omega_0} = \frac{1}{v_g}. \qquad (2\text{-}13)$$

β_1 is also referred as the group delay, τ_g. The second derivative of the propagation constant (β_2) is the dependence of the group delay with respect to ω, and is related to the group delay dispersion (GDD). The second- or higher-order dispersion (β_n (n > 2)) is especially important when the pulse duration is much narrower than ~100 fs.

The second-order dispersion β_2 is related to the dispersion parameter, D, which shows the wavelength dependence of GDD:

$$D(\lambda) = \frac{d\tau_g}{d\lambda} = \frac{d\beta_1}{d\omega}\frac{d\omega}{d\lambda} = -\frac{2\pi c\beta_2}{\lambda^2}, \qquad (2\text{-}14)$$

where λ is the center wavelength, respectively. D is specified in units of ps/km/nm, and

pulse broadening is measured in picoseconds. The length of the medium is in kilometers, and the source spectral width is in nanometers.

To understand the dispersion effect intuitively, we consider that the two-color monochromatic plane waves E_1 and E_2, whose frequencies are ω_0 and $\omega_0 + \delta\omega$ ($\delta\omega \ll \omega_0$), respectively, collinearly propagate in dispersive medium with a length of L. The waves after propagation are represented by Eq. (2-1):

$$E_1 = \cos(\omega_0 t - \beta_0 L), \tag{2-15}$$

$$E_2 = \cos[(\omega_0 + \delta\omega)t - (\beta_0 + \delta\omega\beta_1)L]. \tag{2-16}$$

The total electric field is given by

$$E = 2\cos\left[\frac{\delta\omega}{2}t - \frac{\beta_1\delta\omega}{2}L\right]\cos\left[\frac{(2\omega + \delta\omega)}{2}t - \frac{(2\beta_0 + \delta\omega\beta_1)}{2}L\right]. \tag{2-17}$$

The first term of Eq. (2-17) corresponds to the envelope, and is time-delayed by as much as $\beta_1 L$, as shown in Fig. 2.3(b). In other words, β_1 is related to the time delay of the envelope by the propagation in the dispersive medium. This is why β_1 is called the group delay, τ_g.
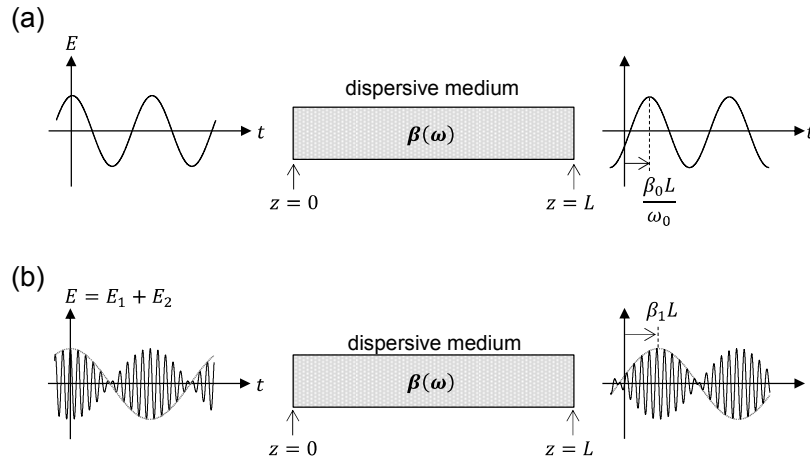
Fig. 2.3. Effect of light propagation in dispersive medium. (a) When a monochromatic light wave propagates in a dispersive material with propagation constant and distance of β and L, respectively, the output electric field is time-delayed by as much as $\beta_0 L/\omega_0$. (b) When an optical beat generated by two-color light waves, E_1 and E_2, propagates through the material, its envelope is time-delayed by as much as $\beta_1 L$. Hence, β_1 is referred to as group delay.

It is better to consider the propagation of optical pulse for β_2. Since the optical pulse is formed by many multicolor light waves, it can be treated as a group of small pulses with very narrow bandwidths, that is, wave packets. A wave packet propagates in the material at a propagation velocity of v_g. Because of the wavelength dependence of v_g, the group velocity dispersion, the wave packets are dispersed in time. This is an intuitive depiction of pulse broadening caused by material dispersion in which GDD is a measure of the separation. The direction of the separation is determined by the sign of GDD. When wave packets composed of shorter wavelengths precede those composed of longer wavelengths during propagation, the material has anomalous dispersion ($\beta_2 < 0$). Otherwise, the material has normal dispersion ($\beta_2 > 0$). Figure 2.4 shows schematic illustrations of the effect of GDD.
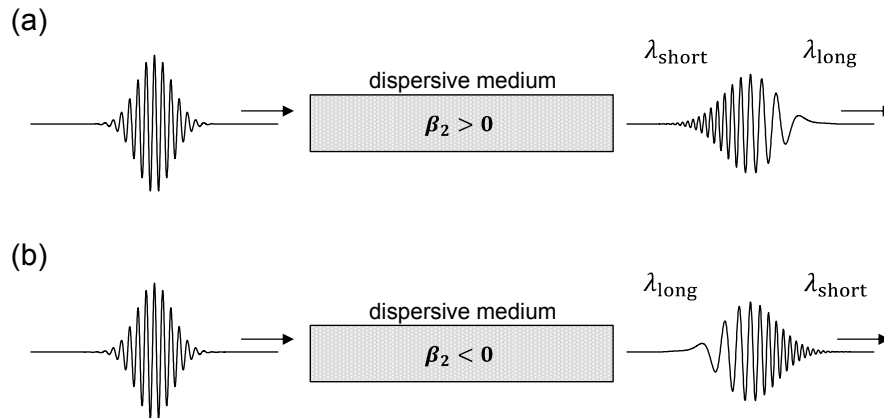
Fig. 2.4. The effect of GDD. When an optical pulse propagates in a dispersive material, its pulse duration lengthens in accordance with the GDD of the material. (a) When the material has normal dispersion, the red components precede the blue components in the pulse. (b) When the material has anomalous dispersion, the blue components precede the red components.

Compensation for GDD is possible through passage through optical devices that have the opposite dispersion with respect to the dispersed pulse (Fig. 2.5). The pulse at the telecommunication band (~1.5 μm) experiences anomalous dispersion ($\beta_2 < 0$) propagating in glass. In this band, GDD is compensated by dispersion-compensating fiber [4], which is designed to have normal dispersion. In the near-infrared region, a pulse experiences normal dispersion ($\beta_2 > 0$) in glass. In this region, a grating pair and a prism pair are used to introduce negative dispersion [5–9].
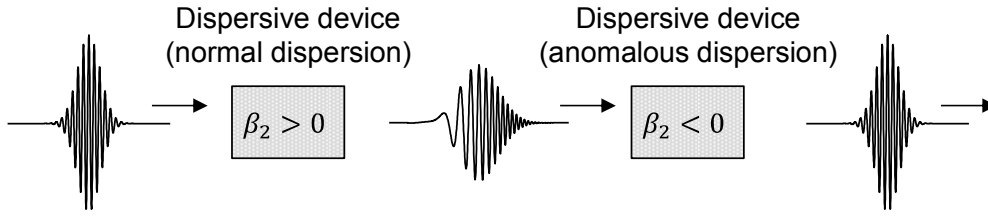
Fig. 2.5. Schematic of GDD compensation.

2.1.4. Optical interference in the Fourier domain

Interference between white light with different delays generates an interference fringe in its spectrum. This is known as spectral interference [10]. We denote a complex electric field of white light as $E(t)$. It is split into two parts, one of which is delayed by time τ. The total field of the two superposed white lights is given by

$$E'(t) = \frac{1}{2}[E(t) + E(t - \tau)]. \tag{2-18}$$

The spectrum of the superposition field is given by the Fourier transform of Eq. (2-18):

$$E'(\omega) = \frac{E(\omega)}{2}\left(1 + e^{i\omega\tau}\right), \tag{2-19}$$

where $E'(\omega)$ and $E(\omega)$ are Fourier transforms of $E'(t)$ and $E(t)$, respectively. Its power spectrum is given by

$$S(\omega) = \left|E'(\omega)\right|^2 = |E(\omega)|^2[1 + \cos(\omega\tau)]. \tag{2-20}$$

This means that the optical spectrum is modulated by a sinusoidal function with a period of $2\pi/\tau$. Figure 2.6, for example, shows the spectral interference under the assumption that the spectral shape is Gaussian.
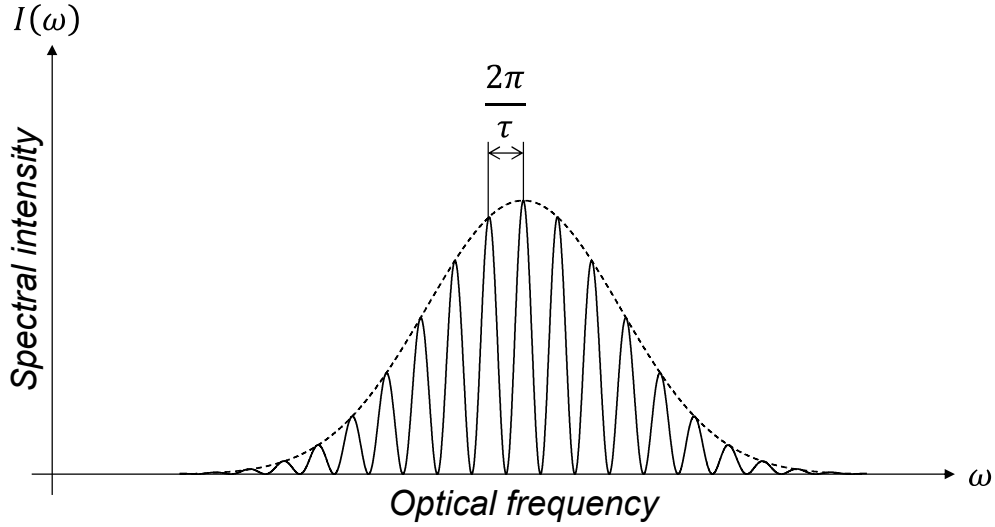
Fig. 2.6. Spectral interference. Delayed interference between white lights with spectra resembling Gaussian shapes, for example, modulates its optical spectrum at a modulation period of $2\pi/\tau$.

2.2. Raman effect

2.2.1. Spontaneous Raman scattering

This section describes the principle of Raman effect [11]. When a dielectric material is irradiated by a light wave, part of the light is scattered by small particles inside the material, such as atoms or molecules. Interestingly, the scattered light includes not only the component of same frequency as that of the incident light but also components of different frequencies. The same-frequency component, known as Rayleigh scattering, is the result of elastic scattering. Components of different frequencies originate from inelastic scattering due to energy transfer between the incident light wave and a molecule. Specifically, inelastic scattering caused by molecular vibrations is called Raman scattering. Since the amount of the frequency shift reflects the intrinsic molecular vibrational frequency, the spectrum of Raman scattering provides information on the molecules in the material. To provide an intuitive picture of Raman scattering, we develop the classical model of the interaction between electric fields and molecular vibrations [12].

When an external electric field $\tilde{E}(t)$ is applied to a dielectric material, molecules inside the material are polarized. The tilde hereafter shows that the function has a real value and oscillates rapidly in time. Microscopic polarization is denoted as follows:

$$\tilde{p}(t) = \epsilon_0 \alpha \tilde{E}(t), \qquad (2\text{-}21)$$

where α is the polarizability, a measure of the polarization of a molecule. We assume that the molecule is Raman active. In other words, the polarizability is a function of the internuclear distance (q) of the molecular bonding. We denote the displacement of q from its equilibrium distance as Δq. By assuming that Δq is so small that the relationship between Δq and α is linear, we can expand the polarizability as follows:

$$\alpha = \alpha_0 + \frac{\mathrm{d}\alpha}{\mathrm{d}q} \Delta q. \qquad (2\text{-}22)$$

The first term denotes the polarizability for $\Delta q = 0$, i.e., the equilibrium intermolecular distance. The second term denotes the first derivative of the polarizability with respect to Δq.

To consider the effect of the polarization with respect to $\mathrm{d}\alpha/\mathrm{d}q$, we denote the electric field of the incident light wave with an amplitude of E_0 as follows:

$$\tilde{E}(t) = E_0 \cos \omega_0 t. \qquad (2\text{-}23)$$

By assuming that a molecular vibrational mode is a sinusoidal oscillation at a frequency of ω_v with an amplitude of Δq, the polarization is given by substituting Eqs. (2-22) and (2-23) into Eq. (2-21) and is represented by

$$
\begin{aligned}
\tilde{p}(t) &= \epsilon_0 \left[\alpha_0 + \frac{\mathrm{d}\alpha}{\mathrm{d}q} \Delta q \cos \omega_v t \right] E_0 \cos \omega_0 t \\
&= \epsilon_0 E_0 \left\{ \alpha_0 \cos \omega_0 t + \frac{\mathrm{d}\alpha}{\mathrm{d}q} \Delta q [\cos(\omega_0 - \omega_v)t + \cos(\omega_0 + \omega_v)t] \right\}.
\end{aligned} \qquad (2\text{-}24)
$$

The first term has the same frequency as that of incident light. Radiation represented by this term contributes to Rayleigh scattering. The second and third terms represent the origins of Stokes Raman scattering and anti-Stokes Raman scattering, respectively (see also Fig. 1.1).

The Raman spectrum has several characteristic bands. As an example, the Raman spectrum of a biological sample is shown in Fig. 2.7 [13]. We can see that there are many fine peaks in the wavenumber range of 500 to 1800 cm^{-1}. Since this region contains rich spectroscopic information of biomolecules, it is known as the fingerprint region. The wavenumber range of 2800 to 3100 cm^{-1} reflects CH stretching vibration. In particular, we can obtain strong peaks reflecting lipid and protein in the CH stretching region. The wavenumber range of 3000 to 3400 cm^{-1} reflects OH stretching vibration. In

this region, the peak reflects water in solvents and cells. On the contrary, the wavenumber range of 1800 to 2800 cm^{-1} is flat. Hence, this region is called the cellular silent region.

It should be noted that the signal of spontaneous Raman scattering is weak. This is because the Raman scattering cross section, which is the proportional coefficient of the scattering, is very small. This leads to long acquisition time (typically on the order of ~1 s) needed to achieve high signal-to-noise ratio (SNR).
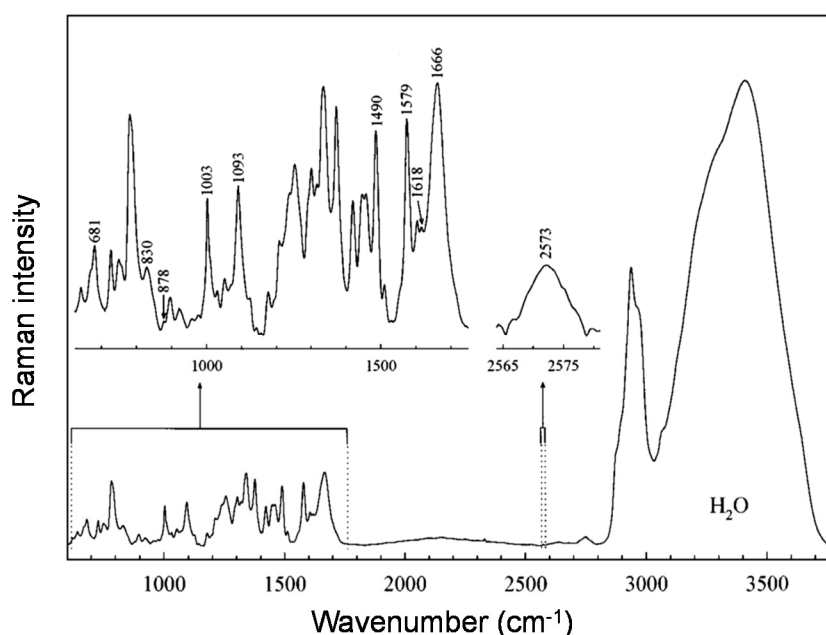
Fig. 2.7. Raman spectrum of P22 virus in H_2O buffer [13].

2.2.2. Nonlinear Raman scattering

One of the technologies for improving the sensitivity of Raman scattering is nonlinear Raman scattering [14, 15]. In contrast to spontaneous Raman scattering, it uses two-color light waves to enhance the signal intensity. Such incident waves form a beat, which oscillates at their difference frequency, as described in Section 2.1. When the frequency of the beat matches the molecular vibrational frequency, resonant molecular oscillation occurs in response to the vibrational force of the beat. This drastically enhances the amount of scattering. Since the molecular vibration is coherently driven, this effect is also known as coherent Raman scattering (CRS). To understand the mechanism of CRS, the classical model of the interaction between the molecular vibration and two-color electric fields is developed as follows.

24

We consider how two-color incident light waves can drive molecular vibration. When a blue beam and a red beam, the pump and Stokes, respectively, are incident on a material, polarization is established. The containing energy of the microscopic polarization is described as follows:

$$\widetilde{w} = \frac{1}{2}[\widetilde{p} \cdot \widetilde{E}] = \frac{\epsilon_0 \alpha}{2}\widetilde{E}^2, \qquad (2\text{-}25)$$

where $\widetilde{E}$ is the electric field of the superposition of pump and Stokes waves. Since the intensity of the superposition field oscillates at the beat frequency, E^2 is time-varying. When the material is Raman active, the polarizability is a function of the internuclear distance (q), as described in Section 2.2.1. When α increases, w also increases by reducing the light energy. This generates force on the molecular bond, increasing q and w. Since the energy is the product of the force and displacement, the force on the molecular bond can be obtained by differentiating the energy of polarization with respect to the intermolecular displacement:

$$\widetilde{F} = \frac{\mathrm{d}\widetilde{w}}{\mathrm{d}q} = \frac{\epsilon_0}{2}\frac{\mathrm{d}\alpha}{\mathrm{d}q}\widetilde{E}^2. \qquad (2\text{-}26)$$

Because of this force, the molecules coherently oscillate at the beat frequency.

We assume that the molecular oscillation can be described as a simple harmonic oscillator. We assume that the molecules are forced to oscillate by the optical beat. The theory of resonance of damped oscillators stipulates that when F is a sinusoidal function in time and when its frequency matches ω_v, q is also sinusoidal, and its phase lags by $\pi/2$. Because of the molecular vibration, the polarizability also varies in time. Since two-color waves at ω_p and ω_S irradiate the molecules, the time-dependent polarizability generates sidebands during polarization at $\omega_\mathrm{p} \pm (\omega_\mathrm{p} - \omega_\mathrm{S})$ and $\omega_\mathrm{S} \pm (\omega_\mathrm{p} - \omega_\mathrm{S})$. Because the vibration lags with respect to the beat, the phase of the upper sideband lags by $\pi/2$, while that of the lower sideband advances by $\pi/2$. Since radiation from the polarization lags by $\pi/2$ [1], radiation from the upper sideband is phase-shifted by π, while that from the lower sideband is in-phase. As a result, radiation from the upper sideband of the Stokes polarization attenuates the pump field, and that from the lower sideband of the pump polarization amplifies the Stokes field (see also Fig. 1.3). These are called stimulated Raman loss and stimulated Raman gain, respectively; together, both phenomena are called SRS. SRS can be seen as the energy transfer between the pump and

Stokes fields through the molecular vibration. On the other hand, the upper sideband of pump polarization and the lower sideband of Stokes polarization generate radiation with new frequency components. These are the origins of anti-Stokes Raman scattering and coherent Stokes Raman scattering, respectively.

2.3. Stimulated Raman scattering microscopy

2.3.1. Principle

SRS microscopy is one of the coherent Raman microscopy techniques. As described in Section 2.2, SRS can be considered as the energy transfer from a pump light to a Stokes light. Such energy transfer changes the intensities of these lights, and the resultant change is detected as a signal in SRS microscopy. Usually, pulsed lasers are employed as light sources to utilize their high instantaneous power to efficiently induce the SRS effect. Nevertheless, the amount of energy change in SRS microscopy is typically as small as 10^{-3}–10^{-5} times the energies of the incident pulses [16, 17]. To precisely measure such small signals, the lock-in detection technique is employed. The principle of SRS microscopy is already briefly introduced in Fig. 1.5 in Section 1.3, but it is explained here in detail.

For the lock-in detection, one of the pulse trains is amplitude-modulated before being introduced into the microscope. We assume that the Stokes pulse train is modulated in accordance with Fig. 1.5. After the two-color pulses are overlapped in time and in space, these pulse trains are tightly focused on the sample through a microscope objective. When the difference frequency between pump and Stokes matches the vibrational resonance frequency of molecules, energy transfer due to SRS at the focus occurs. Consequently, the amplitude modulation is transferred to the pump pulse train. The transmitted light is collected by another microscope objective. After the Stokes pulse train is blocked, the pump pulse train is measured by a photodetector. To obtain the SRS signal, modulation transfer in the photocurrent is measured by a lock-in amplifier, in which the known carrier wave is extracted by signal demodulation by mixing a reference wave. (Hence, this technique is sometimes referred to as homodyne detection.) Images are taken by scanning the laser beam with a beam scanner. This is the principle of SRS microscopy.

One of the important parameters that affect the SNR of SRS microscopy is the modulation frequency. It has to be set to at least several megahertz. Otherwise, the SNR of SRS signals decrease markedly, because optical pulses generated by typical lasers have relatively high intensity noise at low frequency due to $1/f$ noise [16, 17]. Furthermore, we can obtain the 3 dB merit in the SNR when the modulation function is rectangular or when the modulation frequency is maximal, i.e., half of the repetition rate [17]. Referring Fig. 2.8, we can intuitively explain this point as follows: When the pulse train is modulated by a sine wave, some pulses are not completely switched off. On the other hand, when the modulation function is rectangular or sinusoidal at the subharmonic frequency, all the pulses are completely switched on or off.
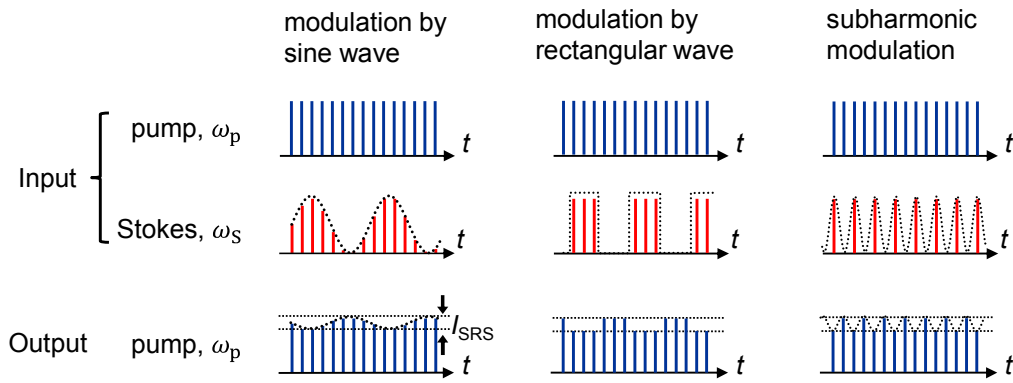
Fig. 2.8. Schematic illustration of pulse modulations with various modulation functions in SRS microscopy.

2.3.2. Photodetection noise and sensitivity

In photodetection, the shot noise and thermal noise are important noise sources that determine the sensitivity of SRS microscopy. Thermal noise originates from thermal agitation of charge carriers in electrical conductors [18]. The current of thermal noise is given by

$$i_{\text{th}} = \sqrt{\frac{4k_B T B}{R}},$$
(2-27)

where k_B is the Boltzmann's constant, T is the absolute temperature of the resistor in kelvins, B is the bandwidth of the measuring instrument, and R is the resistor value.

Thus, the thermal noise is independent of the optical intensity but depends on the temperature and measuring instruments. Its power spectral density is flat. The shot noise originates from the fluctuation of the photocurrent in photodetection. The shot noise current is defined as follows [19]:

$$\langle i_{\text{shot}} \rangle = \sqrt{2eiB}, \tag{2-28}$$

where i is the average photocurrent, and e is the elementary charge. On the other hand, the photocurrent or signal is given by

$$i(t) = \frac{\eta e}{\hbar \omega} \langle I(t) \rangle, \tag{2-29}$$

where η is the quantum efficiency, $\hbar \omega$ is the photon energy, and $I(t)$ is the instantaneous power. The bracket signifies the time average in the response time of the photodetector. The photocurrent increases proportionally to the optical intensity. Thus, the shot noise is proportional to the square root of the optical intensity.

As described above, the shot noise is inherent to optical signals. Hence, it is important to realize that the SNR is limited by the shot noise. In other words, other noises should be much smaller than the shot noise. Eq. (2-27) suggests that increasing the resistor value can suppress the thermal noise, which, in turn, decreases the bandwidth of the photodetector due to the CR time constant. Thus, the optical power at the photodetector has to be sufficiently high such that the shot noise becomes dominant compared with the thermal noise. For example, when $i_{\text{th}} = i_{\text{shot}}$ and $R = 50 \, \Omega$, $i \sim 1$ mA, corresponding to an optical power of ~2 mW under the assumption that for the conversion efficiency of a photodetector, $\eta e / \hbar \omega \sim 0.5$ [A/W].

2.3.3. Excess intensity noise

As described in the previous section, the optical power at the photodetector has to be sufficiently high such that thermal noise is negligible. When optical amplification is used to boost low-power laser pulses in SRS microscopy, however, attention must be paid to another noise source: the excess intensity noise. In this section, we consider how optical amplification affects the SNR of SRS microscopy.

An optical amplifier not only amplifies optical pulses but also leads to spontaneous emission, which originates from vacuum fluctuation. Because of the randomness of spontaneous emission, the emission becomes noise. As a result, the output

of optical amplifiers involves not only the signal but also involves amplified spontaneous emission (ASE), as shown in Fig. 2.9. Since the spectrum of vacuum fluctuation is almost flat, the spectrum of ASE reflects the gain spectrum in which the bandwidth is typically on the order of THz.

Even when the optical power of ASE noise is much smaller than that of optical pulses by orders of magnitude, we should consider the beat noise in the photocurrent. The amplified electric field is described as follows:

$$E'(t) = E'_{\text{pulse}} + E'_{\text{ASE}} + E_{\text{vacuum}}, \qquad (2\text{-}30)$$

where E'_{pulse}, E'_{ASE}, and E_{vacuum} are the amplified electric fields of the pulse, ASE, and vacuum field, respectively. Since the photocurrent is proportional to the optical intensity, the photocurrent includes terms representing optical beats between signal and ASE, ASE and ASE, signal and vacuum field, as well as ASE and vacuum field. As a result, ASE in the optical frequency is converted to broad electric noise in electric frequency. Since the SRS signal is typically detected at a frequency of tens of MHz, the SNR may be reduced due to the beat noise. Notably, the beat related to the vacuum field is the origin of shot noise [20]. Since the ASE is typically much larger than the vacuum field, the signal–ASE beat is much larger than the shot noise. Therefore, the excess intensity noise caused by the signal–ASE beat is an important issue that limits the SNR during use of practical laser sources such as laser diodes and fiber lasers in SRS microscopy.
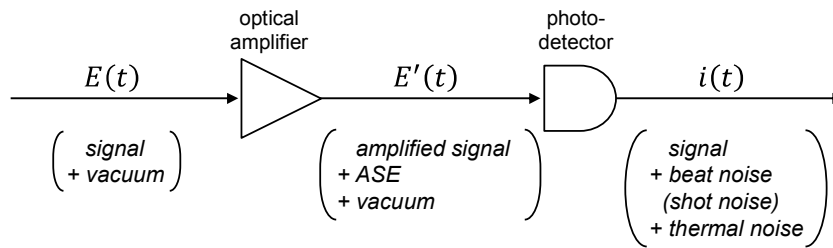

Fig. 2.9. Photodetection of optically amplified signals.

References

[1] E. Hecht and A. Zajac, "*Optics*," 4th ed., Addison-Wesley (2001).

[2] 小林孝嘉 訳, J. Herrman and B. Wilhelmi 著, "超短光パルスレーザー," 共立出版株式会社 (1991). (in Japanese)

[3] G. P. Agrawal, "*Nonlinear Fiber Optics*," 5th ed.*,* Academic Press, (2012).

[4] K. Goda, K. K. Tsia, and B. Jalali, *Nature* **458***,* 1145 (2009).

[5] E. B. Treacy, *IEEE J. Quant. Electron* **5**, 454 (1969).

[6] R. L. Fork, O. E. Martinez, and J. P. Gordon, *Opt. Lett.* **9**, 150 (1984).

[7] J. R. Buckley, F. W. Wise, F. Ö. Ilday, and T. Sosnowski, *Opt. Lett.* **30**, 1888 (2005).

[8] X. Zhou, D. Yoshitomi, Y. Kobayashi, and K. Torizuka, *Opt. Express* **16**, 7055 (2008).

[9] K. Nakagawa, A. Iwasaki, Y. Oishi, R. Horisaki, A. Tsukamoto, A. Nakamura, K. Hirosawa, H. Liao, T. Ushida, K. Goda, F. Kannari, and I. Sakuma, *Nat. Photonics* **8**, 695 (2014).

[10] M. Born and E. Wolf, "*Principles of Optics*," 7th ed., Cambridge Univ. Press, Cambridge (1999).

[11] C. V. Raman and K. S. Krishnan, *Nature* **121**, 501 (1928).

[12] 浜口宏夫, 平川暁子 編, "*ラマン分光法*," (学会出版センター, 1988). (in Japanese)

[13] G. J. Thomas, Jr., *Ann. Rev. Biophys. Biomol. Struct.* **28**, 1 (1999).

[14] R. W. Boyd, "*Nonlinear Optics*," Academic Press (2008).

[15] 黒田和夫, "*非線形光学*," コロナ社, (2008). (in Japanese)

[16] C. W. Freudiger, W. Min, B. G. Saar, S. Lu, G. R. Holtom, C. He, J. C. Tsai, J. X. Kang, and X. S. Xie, *Science* **322**, 1857 (2008).

[17] Y. Ozeki, Y. Kitagawa, K. Sumimura, N. Nishizawa, W. Umemura, S. Kajiyama, K. Fukui, and K. Itoh, *Opt. Express* **18**, 13708 (2010).

[18] A. Yariv, P. Yeh, "*Photonics: Optical Electronics in Modern Communication*," 6th ed., Oxford Univ. Press (2006).

[19] Y. Ozeki, F. Dake, S. Kajiyama, K. Fukui, and K. Itoh, *Opt. Express* **17**, 3651 (2009).

[20] 菊池和朗, "*光ファイバ通信の基礎*," 昭晃堂 (1997). (in Japanese)

Chapter 3

Collinear balanced detection (CBD): a new type of balanced detection based on photonic RF spectral modulation

As described in Chapter 2, stimulated Raman scattering (SRS) microscopy requires ultraquiet laser sources. Although fiber lasers (FLs) enhance the practicality of SRS microscopy, employing such lasers leads to deterioration of the signal-to-noise ratio (SNR) because of its excess intensity noise. Thus, I propose CBD, as a new balanced detection technique. It overcomes the issue with ordinary balanced detection by suppressing the effect of intensity noise at a specific frequency by collinear photodetection. In CBD, a photocurrent spectrum is modulated by introducing a delay in the optical domain. Hence, this procedure is referred to as *"photonic RF spectral modulation."* The concept of photonic RF spectral modulation is quite general. It can be applied not only to optical pulses, but also to nonpolarized optical noise. In Section 3.1, the principle of CBD is introduced, and its proof-of-principle experiment is described. In Section 3.2, fiber-based CBD, a version of CBD with improved practicality, is developed. In Section 3.3, application of photonic RF spectral modulation to nonpolarized optical noise is described. Finally, achievements in this chapter are summarized in Section 3.4.

3.1. Proposal of CBD

3.1.1. Principle

Figure 3.1 schematically illustrates the principle of CBD [1]. An optical pulse train is introduced into a delay line, termed *"delay-and-add line* (DAL)," which consists of two delay arms of different lengths. The optical pulse train is divided into two pulse trains that separately pass through the two delay arms, resulting in a delay difference. They are then recombined collinearly and photodetected. Here, the pulse trains obtained from the short

and long delay arms are called "*signal*" and "*reference*" pulse trains, respectively, named after their counterparts in ordinary balanced detection. Here, the photocurrents created by the signal and the reference are denoted as $i_{\text{sig}}(t)$ and $i_{\text{ref}}(t)$, respectively. We assume that the signal and reference pulse trains are incoherently added. This assumption is valid when the pulse trains are combined in polarization states orthogonal with each other, and/or when the pulses are not overlapped in time. Because of the incoherent addition, the intensity of the combined pulse train is simply the sum of those of the signal and the reference. Therefore, the total photocurrent is also the sum of both photocurrents generated by the signal and the reference. Since the reference is a delayed replica of the signal,

$$i_{\text{ref}}(t) = i_{\text{sig}}(t - \tau), \qquad (3\text{-}1)$$

where τ is the delay difference, the total photocurrent is given by

$$i(t) = i_{\text{sig}}(t) + i_{\text{ref}}(t) = i_{\text{sig}}(t) + i_{\text{sig}}(t - \tau). \qquad (3\text{-}2)$$

In the Fourier domain,

$$i(\omega) = i_{\text{sig}}(\omega)[1 + \exp(i\omega\tau)], \qquad (3\text{-}3)$$

where $i(\omega)$ and $i_{\text{sig}}(\omega)$ are the Fourier transforms of $i(t)$ and $i_{\text{sig}}(t)$, respectively. Equation (3-3) indicates that photocurrents of the signal and the reference are added destructively at a frequency ω_{CBD} ($\omega_{\text{CBD}} = (2n + 1)\pi/\tau$ ($n = 0, 1, 2, \ldots$)) because a delay of τ in the time domain corresponds to the linear spectral phase of $\omega\tau$. The RF spectral density is given by

$$|i(\omega)|^2 = 2|i_{\text{sig}}(\omega)|^2[1 + \cos(\omega\tau)]. \qquad (3\text{-}4)$$

In this way, the effect of the intensity noise can be suppressed at ω_{CBD}. This is the principle of CBD.
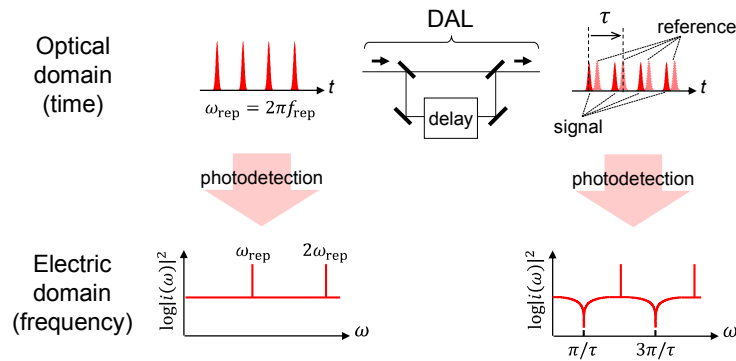

Fig. 3.1. Principle of CBD.

One important feature of CBD is that introducing a time delay in the optical domain modulates the photocurrent spectrum. Such a modulation originates from interference between photocurrents instead of interference between light waves. Therefore, this technique is referred to as "*photonic RF spectral modulation.*" This technique is different from a well-known technique, spectral interference, which involves spectral modulation in the optical frequency [2].

3.1.2. Proof-of-principle experiment

Figure 3.2 shows a schematic of the experimental setup for the proof-of-principle experiment on CBD. A figure-eight, dispersion managed, all polarization maintaining (PM) Er-doped fiber laser (Er-FL) fabricated in-house [3] was used as a pulse source. Mode-locking operation was achieved by applying an external electric signal to an intracavity electro-optic modulator (Photline Technologies, MPX-LN-0.1). Once the laser was mode-locked, the pulsing was maintained without any modulation. The Er-FL produced 180 fs pulses at a repetition rate (f_{rep}) of 35.2 MHz. The center wavelength and the bandwidth were 1560 and 14 nm, respectively. The pulses were amplified by a PM-Er-doped fiber amplifier (PM-EDFA). The amplified pulses were focused on a 20 mm long periodically poled LiNbO$_3$ (PPLN) crystal (Covesion Ltd., MSHG1550-0.5-20) [4] to generate narrowband (~0.3 nm) second harmonic (SH) pulses, which are suitable for SRS microscopy. The PPLN was equipped with multiple poled periods to obtain wavelength tunability from 760 to 810 nm. The average power of SH pulses was dependent on the wavelength and reached a maximum of 12 mW.

To perform CBD, SH pulses were introduced into a DAL consisting of a polarization beam splitter (PBS), a lens pair, several mirrors, and a right-angle prism. The PBS was used to split the pulse trains in orthogonal polarizations. The lens pair was included in the long delay arm to compensate for beam diffraction. Intensity balance between the signal and reference was adjusted by rotating a half-wave plate (HWP) in front of the PBS.
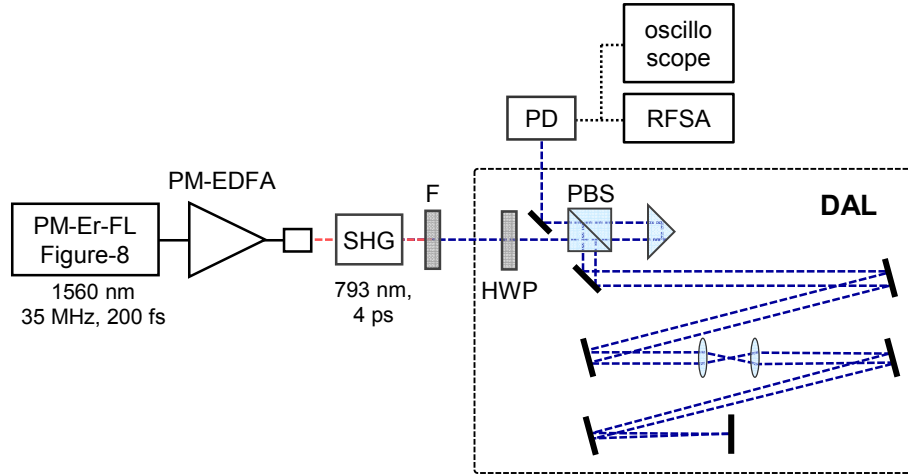
Fig. 3.2. Experimental setup for photocurrent noise suppression by CBD. F: optical filter.

The recombined SH pulse train was detected by a photodetector (PD) fabricated in-house. The PD included a Si photodiode (Hamamatsu, S3399), band-pass filters (BPFs) at a frequency of $f_{\mathrm{rep}}/2$, band elimination filters (BEFs) at a frequencies of f_{rep} and $2f_{\mathrm{rep}}$, electric amplifiers, and its load resistance was 51 Ω. These electric filters were inserted for avoiding the saturation of the electric amplifiers. The total gain of the electric amplifiers was 360. The spectrum of the photocurrent was measured by a RF spectrum analyzer (RFSA, Agilent Technologies, E4411B).

The effectiveness of CBD in the suppression of photocurrent noise has been investigated. To reduce the noise at a frequency of 17.6 MHz (almost the same as $f_{\mathrm{rep}}/2$), the light path lengths of the long and short delay lines at the DAL were set to 8.6 and 0.4 m, respectively. That is, the time delay was ~28 ns, which approximately corresponds to the period of the SH pulse train. The average power of the SH pulse train at the PD was 3.9 mW.

Figure 3.3 shows the obtained RF spectra. The noise spectrum had a broad peak reflecting the characteristics of BPFs (gray). The asymmetric spectral response is presumably due to interference between the BEF and BPF, which is removed by further optimization of filter design. When CBD was active, the photocurrent noise decreased by 13 dB at $f_{\mathrm{rep}}/2$ and was higher than the shot noise limit by only ~1.4 dB, as estimated from a DC photocurrent of 2.5 mA. In this way, the effectiveness of CBD was confirmed.

It should be noted that the intensity noise of the SH pulse train is very susceptible to pump levels of both the Er-FL and EDFA and that there is a tradeoff between achievable

optical power and intensity noise. The noise level without CBD presented in Fig. 3.3 was achieved through careful optimization of pump levels, and noise suppression of >20 dB was readily attained when the pump levels were not fully optimized.
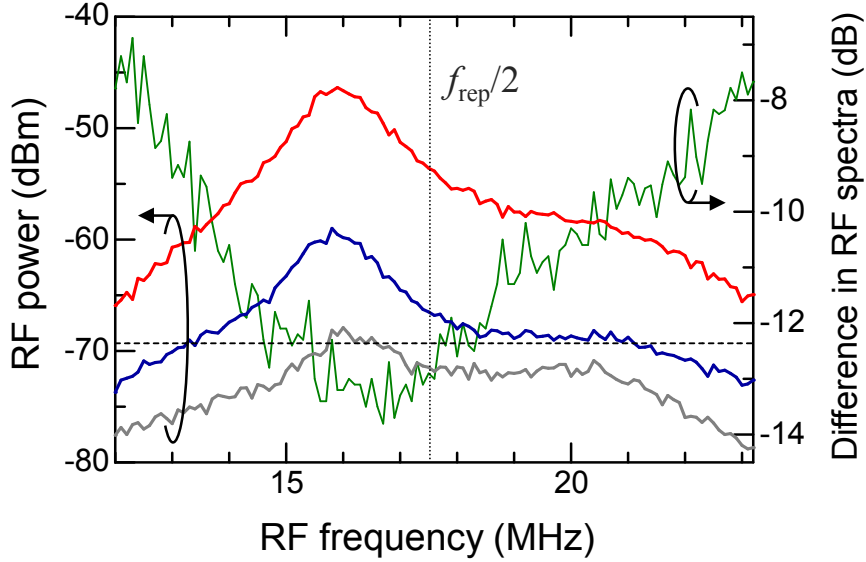

Fig. 3.3. Obtained RF spectra. When CBD is inactive (red), the noise level is much higher than the shot-noise limit (dashed). On the contrary, when CBD is active (blue), the noise is close to the shot-noise limit. The asymmetry peaks may be caused by frequency responses of the electric filters. Circuit noise is indicated by the gray line. For clarity of the noise suppression, the difference in RF spectra is indicated by the green line. Average power: 3.9 mW, resolution bandwidth: 100 kHz.

3.1.3. Comparison with ordinary balanced detection

Balanced detection has been widely used for noise suppression in optical measurements. Its principle is as follows: The signal and reference pulse trains are separately photodetected. The common photocurrent, i.e., noise, is then removed by subtraction of the photocurrents generated from the two photodiodes, and only the target signal is extracted. On the other hand, CBD cancels the photocurrent noise at a specific frequency by interference of the photocurrents as described above. The most important advantage of CBD is collinear photodetection. Although FLs would be attractive for improving practicality of SRS microscopy, their intensity noise is too high compared with shot-noise limit. The intensity noise can be canceled by employing balanced detection [5–7]. However, its performance is limited because the optical transmittance of the signal arm

can vary while the focus scans the sample. In other words, variation of the optical transmission causes intensity imbalance between the signal and reference. In contrast, the intensity balance in CBD is automatically maintained because optical transmissions of the signal and reference are the same. Hence, CBD sufficiently suppresses the effect of intensity noise even when transmission of the microscope varies.

Compared with SNR when a quiet laser source is used without any balanced detection, CBD has a 6 dB drawback in shot-noise-limited SNR. The pulse train is divided into signal and reference pulse trains, and only the signal pulse train contributes to the SRS signal. As a result, the amplitude of the SRS signal in the photocurrent is halved. In contrast, the noise level is maintained because both photocurrents originating from the signal and reference contribute to the shot noise.

Compared with ordinary balanced detection, the SNR drawback of CBD is 3 dB. This is because shot noise is contributed by both the signal and reference while the SRS signal level is maintained. In principle, the SNR drawback in ordinary balanced detection can be reduced by increasing the intensity of the reference. This is because the shot noise contributed by the reference is negligible when its photocurrent is attenuated to balance photocurrents of the signal and reference.

Nevertheless, CBD is effective in SRS microscopy because of its collinear arrangement during use of noisy laser sources. Application of CBD to FL-based SRS microscopy is presented in Chapter 4.

3.2. Development of practical CBD using fiber delay lines

3.2.1. Proposal of fiber-based CBD

Although CBD has been demonstrated to be effective in suppressing the effect of intensity noise, its practicality remains problematic, i.e., it requires a long delay line. This increases the size of light sources for SRS microscopy. Furthermore, this requires stringent optical alignment; two divided beams with the same beam diameters, the same direction, and the same divergences have to be combined collinearly. To address these issues, I propose fiber-based CBD [8], in which a DAL consists of fiber components. This is effective for downsizing of the DAL. In their application to SRS microscopy, PM fiber components are employed to maintain polarization states of incident pulses so that unwanted optical interference between the signal and reference does not occur.

Figure 3.4 illustrates fiber-based CBD. A pulse train is coupled to a PM fiber through a fiber collimator and split into the signal and reference by a PM-fiber-pigtailed PBS. The divided pulse trains propagate along the slow and fast axes of the PM fiber. After a time delay difference of τ is given to the pulse trains by fiber-delay arms, pulse trains are recombined by a PM-fiber-pigtailed polarization beam combiner (PBC) and detected by a PD. Optical powers of the two pulse trains are adjusted with a HWP so that a photocurrent noise is maximally suppressed. Fiber-based DAL is much smaller than free-space DAL. Furthermore, precise alignment is not necessary for the overlap of signal and reference in space.
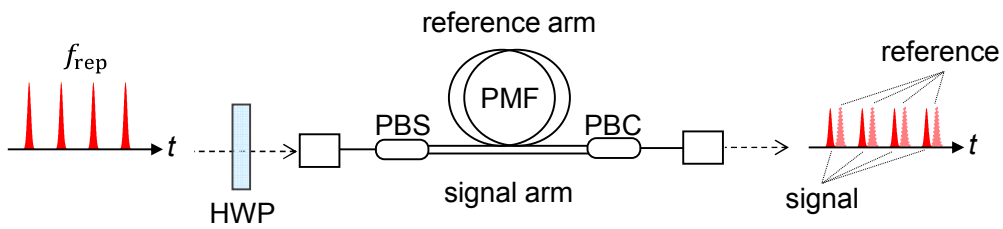

Fig. 3.4. Schematic of the fiber-based DAL.

3.2.2. Experimental setup

The experimental setup for the proof-of-principle demonstration of fiber-based CBD is shown in Fig. 3.5. A PM-Er-FL (IMRA, Femtolite Ultra CS-20) was used as an oscillator. The pulse width, center wavelength, repetition rate, and optical power were ~200 fs, 1560 nm, 51.1 MHz (f_{rep}), and ~20 mW, respectively. The pulses were then amplified to ~350 mW by another PM-EDFA, which was newly developed to obtain much stronger optical pulses. After dispersion compensation using a Si prism pair, the amplified pulses were frequency-doubled in a 25 mm long, MgO-doped PPLN (MgO:PPLN, HC photonics) crystal, for application to SRS microscopy. The center wavelength and optical power were 788.2 nm and ~40 mW, respectively. After fundamental pulses were removed by a color glass filter (SCHOTT, RG9), SH pulses were introduced to the fiber-based DAL, as shown in Fig. 3.6. The delay difference was set to 19.5 ns so that the photocurrent noise near $f_{rep}/2$ was suppressed. Loss of the fiber-based DAL was found to be 6 dB. Such loss is expected to be reduced down to ~3 dB by optimization of the DAL setup.

The photocurrent of SH pulses was obtained by using another homemade Si PD, which was optimized to obtain the photocurrent in the vicinity of $f_{rep}/2$. The load resistor was 51 Ω and the total gain of the electric amplifiers was 160. The photocurrent spectrum was measured by a RFSA with a resolution bandwidth of 100 kHz.
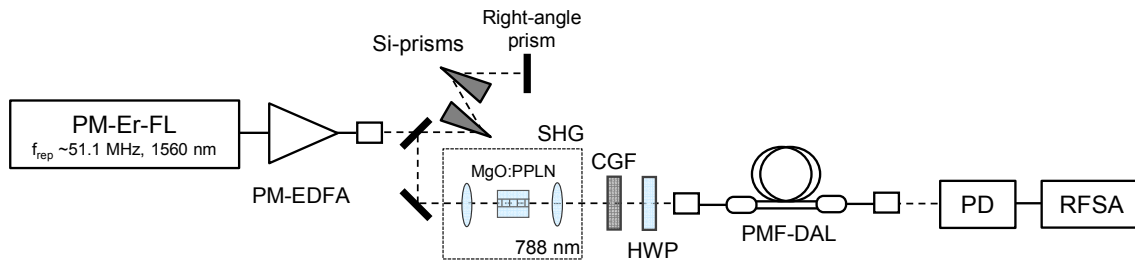

Fig. 3.5. Experimental setup for the proof-of-principle demonstration for fiber-based CBD.
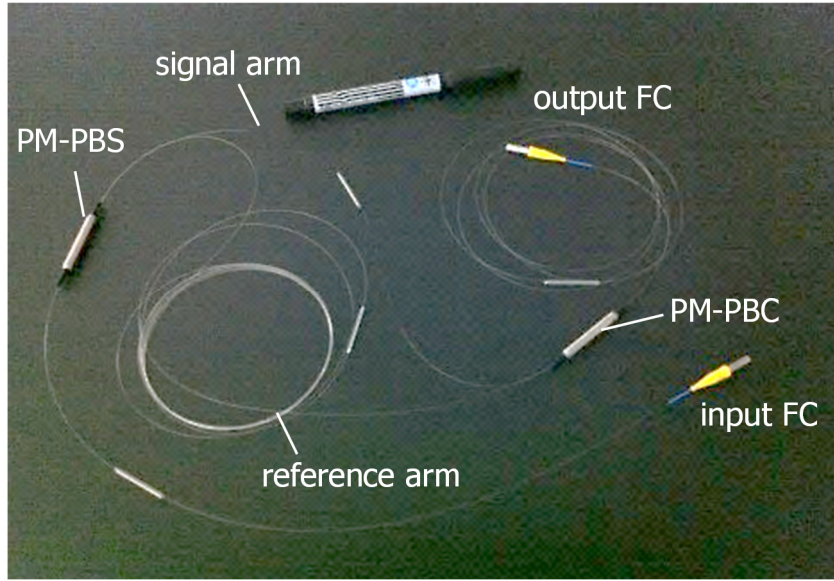
Fig. 3.6. The fiber-based DAL, all components of which maintain polarization.

3.2.3. Experiment on high-frequency noise suppression

Photocurrent noise suppression by fiber-based CBD is investigated. Figure 3.7 shows the measured intensity noise at a frequency of $f_{\mathrm{rep}}/2$ as a function of the input optical power. Intensity noise levels at $f_{\mathrm{rep}}/2$ with or without CBD are plotted as triangles and circles, respectively. The circuit noise and shot noise of our PD are indicated by broken and solid lines, respectively. The shot noise was calculated from a DC photocurrent of 14.5 mA. When CBD was inactive, the intensity noise was much larger than the shot-noise limit. In contrast, when CBD was active, the intensity noise showed good agreement with the shot-noise limit. The slopes, which depict the dependence of the noise level on the optical power, were 1.8 and 0.97, when CBD was inactive and active, respectively. These values prove that fiber-based CBD suppressed the effect of the intensity noise to the shot-noise limit.
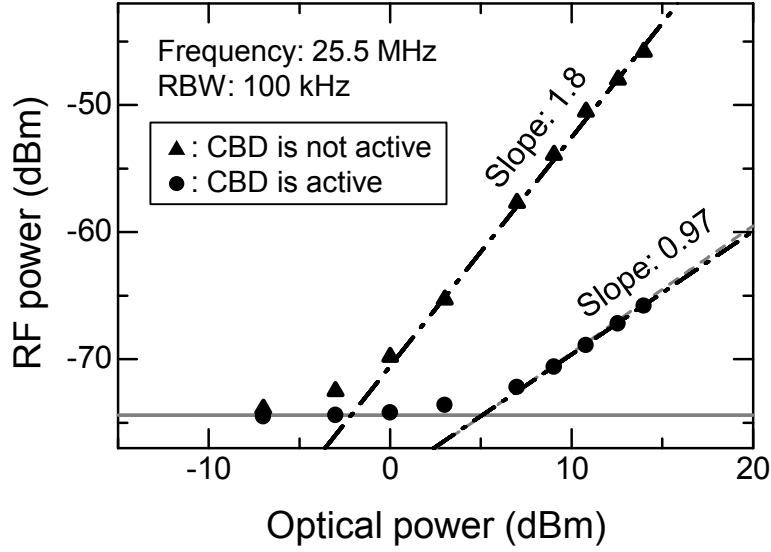
Fig. 3.7. RF power of the photocurrent noise at a frequency of 25.5 MHz ($f_{\mathrm{rep}}/2$). Intensity noises were measured as a function of an input power when CBD was inactive (triangle) or active (circle). The gray solid line and dashed line show theoretical circuit noise of our PD and the shot-noise level calculated from the DC photocurrent, respectively. Fitted lines (black, dashed, and dotted) show that excess noise was dominant when CBD was inactive whereas the noise level was shot-noise limited when CBD was active.

3.2.4. The effect of nonlinear spectral broadening in fiber delay lines

When optical pulses propagate along optical fibers, the pulses may suffer from self-phase modulation (SPM)-induced spectral broadening, which is one of the nonlinear optical effects in the fiber. This leads to degradation of spectral resolution in SRS microscopy. Hence, the influence of SPM in the fiber-based DAL was investigated by obtaining its output spectrum. Although the fiber-based DAL has a fiber-delay arm as long as several meters, we only have to pay attention to the effect in the short fiber-delay arm because only pulses from the short arm contribute to the SRS signal. Thus, the output spectrum from the short arm was obtained, while the long arm was disconnected to remove the pulses from the long arm. Figure 3.8 shows measured spectra with various input powers. From this result, it is confirmed that spectral change in the fiber-based DAL was negligible even when the input power was maximum of the developed source.
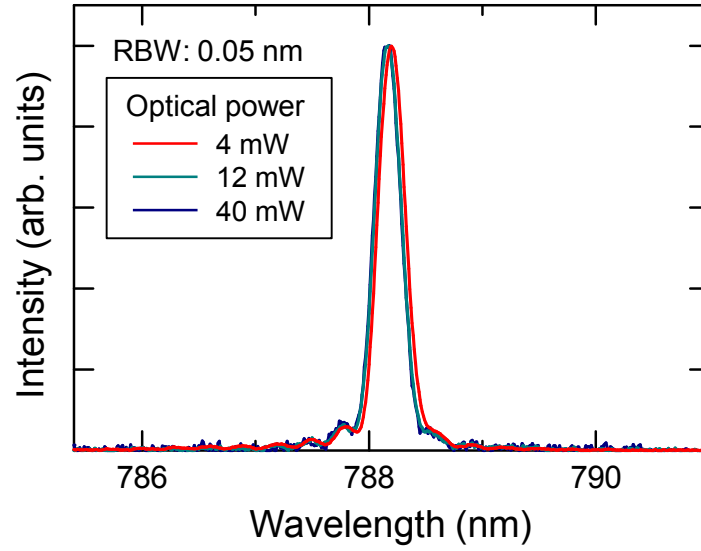
Fig. 3.8. Output spectra of the short fiber delay arm of the fiber-based DAL. Spectra with optical powers of 12 and 40 mW overlap.

3.3. Expansion of the concept of CBD

3.3.1. Photonic RF spectral modulation by optical noise

In the preceding sections, the principle of CBD was experimentally confirmed. As mentioned in Chapter 3.1.1, CBD is regarded as photonic RF spectral modulation. Incidentally, photonic RF spectral modulation can be conducted not only with optical pulses as in the case of CBD, but also with optical noise. This new phenomenon indicates that photonic RF spectral modulation is a general concept [9].

Figure 3.9 shows the apparatus. An Er-doped fiber pumped by a 980 nm laser diode generated an amplified spontaneous emission (ASE) with an average power of 3 mW. The ASE was then spectrally passed through a tunable optical band-pass filter (TBPF, Koshin Kogaku Co., Ltd, FC-1560B-3-16) with a bandwidth of 16 nm. The center wavelength of the ASE was set by the TBPF to 1551 nm. The ASE was divided into two parts by a 3 dB fiber coupler. One part was introduced into a standard single-mode fiber (SMF) with a length of 872 m and recombined with the other part in another 3 dB fiber coupler. The combined ASE was directed to a PD, and its photocurrent was measured by a RFSA. Note that the ASE was nonpolarized light, and we did not incorporate a polarization controller.

Figure 3.10 shows the obtained RF spectrum, which is the average of 30 measurements. The RF spectrum was modulated periodically (black). Such modulation cannot be seen in the case of ordinary ASE–ASE beat noise, which has a flat spectrum at a frequency much lower than the spectral width of ASE. To obtain the modulation period (Δv), the spectrum was fitted with a curve (gray, dotted) with the equation of the power spectrum given by

$$I(\Delta f) = I_0 + I_1 \cos[2\pi\Delta f / \Delta v - \phi], \tag{3-5}$$

where I_0 and I_1 are the RF power offset and the fringe amplitude, respectively. Δf is the frequency deviation from 600.5 MHz (f_0), and ϕ is the modulation phase. The period of RF modulation was found to be ~236 kHz. Note that the fringe did not change when we moved the fiber to vary the state of polarization of the transmitted light during the experiment. Assuming that the relation between the delay difference τ and the modulation period Δv is the same as that observed by conventional spectral interferometry (i.e., $\Delta v = 1/\tau$) [2], we found that the calculated value of τ was 4.23 μs. By assuming a refractive index of 1.47, we found this delay to correspond to a fiber length of 863 m, which agrees well with the actual fiber length. We define the visibility of the fringe (V) as

$$V = \frac{I_{\max} - I_{\min}}{I_{\max} + I_{\min} - 2I_{\mathrm{th}}} = \frac{I_1}{I_0 - I_{\mathrm{th}}}, \tag{3-6}$$

where $I_{\max}$ and $I_{\min}$ are the maximum and minimum values of the fitted RF spectrum, respectively, and I_{th} is the thermal noise of the measuring instruments. V was found to be 0.48.
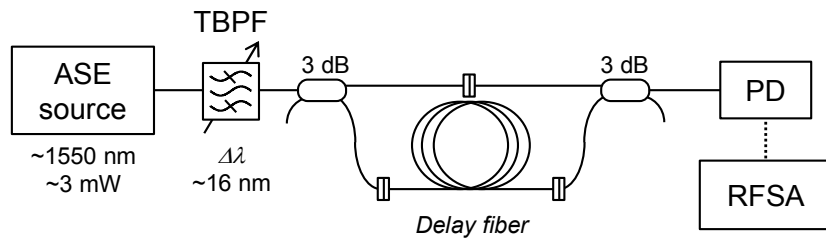

Fig. 3.9. Apparatus used for the RF spectral modulation of optical noise.
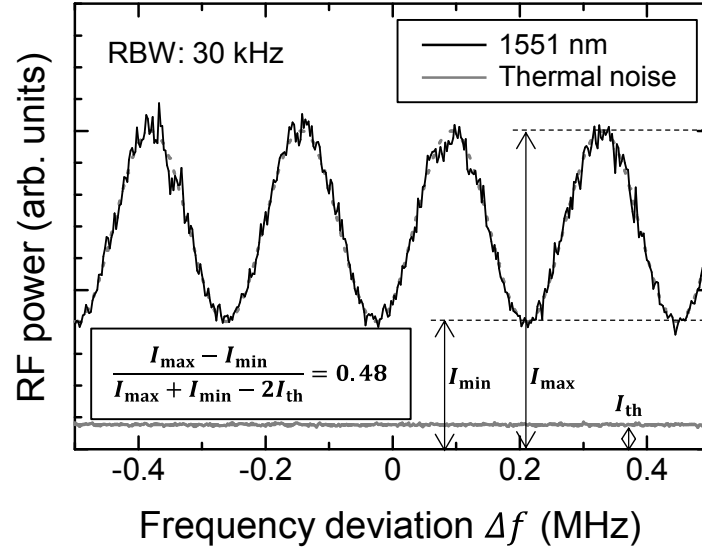
Fig. 3.10. RF spectrum obtained from the average of 30 measurements. Spectra were obtained in near the center frequency of 600.5 MHz.

3.3.2. Validation of the delay dependence of the RF fringe

To confirm whether the period of the RF fringe reflects the delay time, we investigated whether a slight difference in group delay due to group delay dispersion (GDD) of fibers affects the RF modulation. To do so, RF spectra were obtained at various ASE wavelengths, which were tuned by the TBPF. Since the change in Δv is much smaller than the original value (Δv), the modulation phase difference ($\Delta \phi$) was observed by using one of the measured phases as a phase reference, ϕ_0. Experimental results are shown in Fig. 3.11(a). The RF spectra were normalized and offset for clarity. Table 3.1 shows the measured ϕ and $\Delta \phi$. The phase measured at a wavelength of 1546.9 nm was used as ϕ_0. Measured phase differences were converted to the group delay difference per kilometer ($\Delta \tau$) through the following relation:

$$\Delta \tau = \frac{\Delta \phi}{2\pi f_0 L}, \tag{3-7}$$

where L is the length of the delay fiber. Figure 3.12 shows the obtained $\Delta \tau$ plotted as circles. The slope of the linear fitting of $\Delta \tau$ shows that the measured GDD is 17.1 ps/nm/km. This result is in good agreement with that of the standard SMF. Next, we replaced the SMF by a dispersion-shifted fiber (DSF), which is designed such that the

43

zero-dispersion wavelength is approximately 1.55 μm at unknown fiber length. Its GDD was also subsequently measured. The obtained RF spectra are shown in Fig. 3.11(b). The period of RF spectral modulation was ~153 kHz. The fiber length that was obtained from this value was ~1334 m. Table 3.2 shows the measured values of ϕ and $\Delta\phi$. The phase measured at a wavelength of 1547.4 nm was used as ϕ_0. $\Delta\tau$ is calculated from $\Delta\phi$ through Eq. (3-7), and the calculated values are plotted as triangles in Fig. 3.12. The GDD of the DSF was determined to be –0.4 ps/nm/km, which is much smaller than that of the SMF. Thus, we confirmed that RF spectral modulation reflects the optical delay. Furthermore, theoretical analysis supports this phenomenon (see Appendix A), showing that the visibility is 0.5 regardless of the polarization state of the transmitted light. Compared with other techniques for measuring the group delay of long optical fibers, the present technique is a simpler way for group delay monitoring because it does not involve any optical modulation [10, 11].

3.3.3. Comparison with CBD

Although the concept of photonic RF spectral modulation is applicable not only to optical pulses but also to nonpolarized optical noise, there are intrinsic differences between them. In CBD, linearly polarized optical pulses are used as the reference and signal, and they are combined with orthogonal polarizations. This leads to a visibility of 1 because optical interference between pulses does not occur and only interference between photocurrents is involved. On the other hand, when optical noise is used, optical interference occurs partially and the visibility in the photocurrent is 0.5. Nevertheless, the concept of photonic RF spectral modulation is general: the delay difference in optical domain leads to spectral modulation in the RF domain.
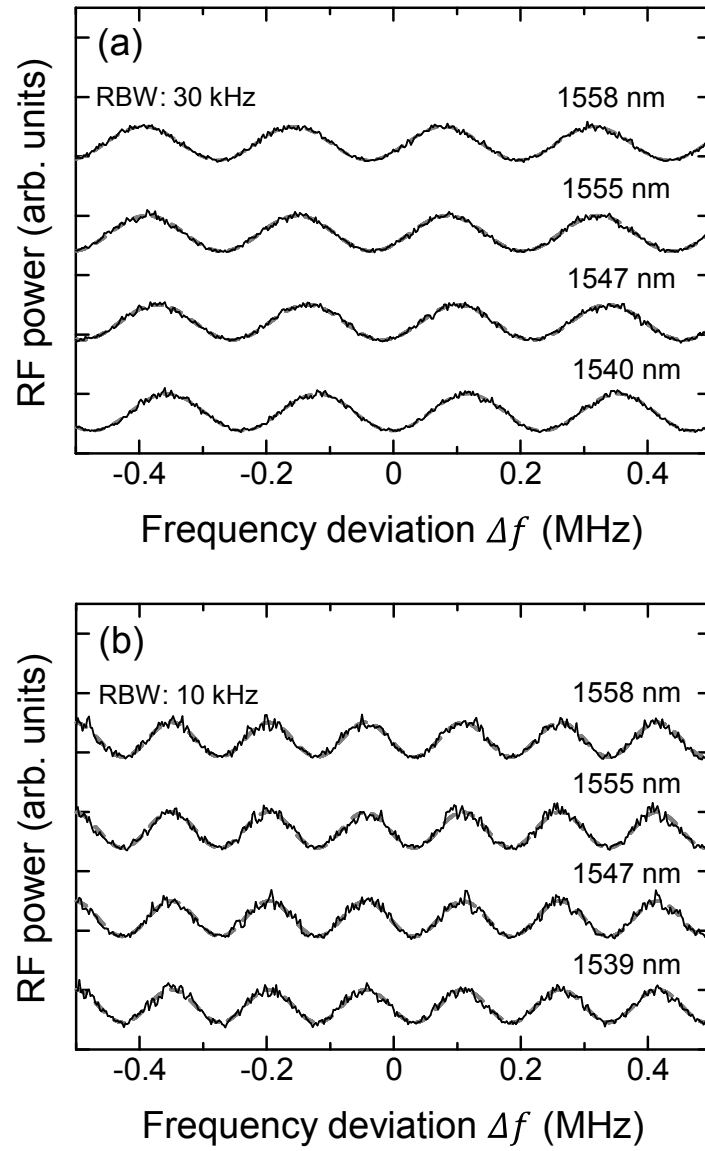
Fig. 3.11. RF spectra for (a) the SMF and (b) the DSF obtained at various wavelengths of ASE. These spectra are obtained near the center frequency of 600.5 MHz. Vertical axes are normalized and offset for clarity. Average number of signals: (a) 30 and (b) 1.

Table 3.1. Measured RF modulation phases and phase differences for the SMF.

	Wavelength (nm)			
	1540	1546.9	1554.9	1557.9
Phase ϕ (rad)	0.0452	0.481 (ϕ_0)	0.901	1.05
Phase difference $\Delta\phi = \phi - \phi_0$ (rad)	$-$ 0.435	0	0.42	0.564

Table 3.2. Measured RF modulation phases and phase differences for the DSF.

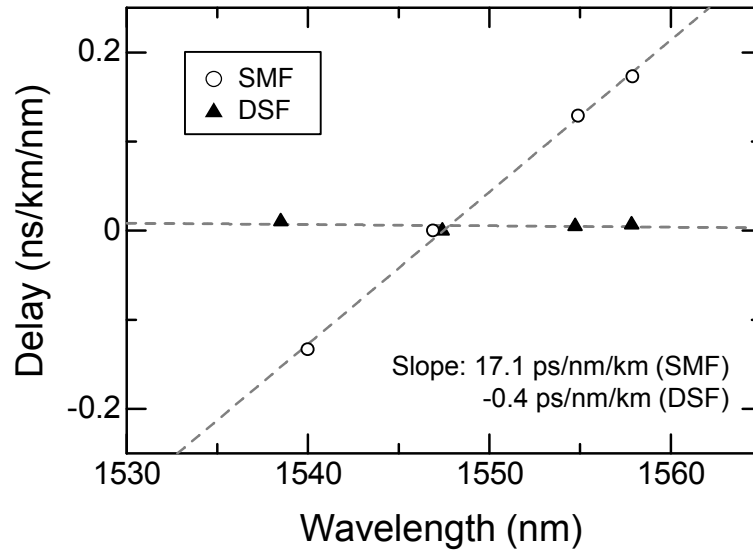|	Wavelength (nm)			
	1538.5	1547.4	1554.7	1557.8
Phase ϕ (rad)	4.997	4.945 (ϕ_0)	4.971	4.979
Phase difference $\Delta\phi = \phi - \phi_0$ (rad)	0.0516	0	0.0256	0.0341

Fig. 3.12. Measured group delay differences of the SMF (circle) and DSF (triangle).

3.4. Conclusion

The technique for high-frequency noise suppression, CBD, is proposed and explained in this chapter. CBD was applied to the SH of the amplified Er-FL pulses for the proof-of-principle experiment. We then confirmed that the high-frequency noise was suppressed. The measured noise level was higher than the shot noise by only 1.4 dB. The DAL was then replaced by optical fibers. We confirmed that the intensity noise was suppressed to the shot-noise limit and that nonlinear spectral broadening, which is an important issue with fiber-based CBD, was negligible when the optical power was as much as 40 mW. In this way, the effectiveness of CBD was demonstrated.

Photonic RF spectral modulation, a concept identical to CBD, was applied to nonpolarized optical noise. We experimentally confirmed that an RF spectral fringe with a visibility of 0.5 appeared. The relation between the RF fringe and delay difference was also confirmed through GDD measurements of the optical fibers.

The results show that the concept of photonic RF spectral modulation is applicable to various forms of light ranging from optical pulses to optical noises and that it may find various applications. In fact, CBD has been recently reported to be effective in squeezed photon-number generation; it has been employed to reduce the effect of intensity noise originating from a noisy laser source [12].

References

[1]   K. Nose, Y. Ozeki, T. Kishi, K. Sumimura, N. Nishizawa, K. Fukui, Y. Kanematsu, and K. Itoh, *Opt. Express* **20**, 13958 (2012).

[2]   M. Born and E. Wolf, "*Principles of Optics,*" 7th ed., Cambridge Univ. Press, (1999).

[3]   J. W. Nicholson, and M. Andrejco, *Opt. Express* **14**, 8160 (2006).

[4]   G. Krauss, T. Hanke, A. Sell, D. Träutlein, A. Leitenstorfer, R. Selm, M. Winterhalder, and A. Zumbusch, *Opt. Lett*. **34**, 2847 (2009).

[5]   A. Gambetta, V. Kumar, G. Grancini, D. Polli, R. Ramponi, G. Cerullo, and M. Marangoni, *Opt. Lett.* **35**, 226 (2010).

[6]   E. Molotokaite, V. Kumar, C. Manzoni, D. Polli, G. Cerullo, and M. Marangoni, *J. Raman Spectrosc* **44**, 1385 (2013).

[7]   C. W. Freudiger, W. Yang, G. R. Holtom, N. Peyghambarian, X. S. Xie, and K. Q. Kie, *Nat. Photonics* **8**, 153 (2014).

[8]   K. Nose, T. Kishi, Y. Ozeki, Y. Kanematsu, H. Takata, K. Fukui, Y. Takai, and K. Itoh, *Jpn. J. Appl. Phys.* **53**, 052401 (2014).

[9]   K. Nose, Y. Ozeki, Y. Kanematsu, Y. Takai, and K. Itoh, *Opt. Rev.* **21** 425 (2014).

[10]   L. G. Cohen and C. Lin, *Appl. Opt.* **16,** 3136 (1977).

[11]   B. Costa, M. Puleo, and E. Vezzoni, *Electron. Lett.* **19,** 1074 (1983).

[12]   S. Sawai, H. Kawauchi, K. Hirosawa, and F. Kannari, *Opt. Express* **21**, 25099 (2013).

Chapter 4

Fiber-laser-based stimulated Raman scattering (FL-SRS) microscopy with shot-noise limited sensitivity

In this chapter, the application of collinear balanced detection (CBD) to a FL-SRS microscope is explained. To generate subharmonically synchronized pump and Stokes pulses, an Er-doped FL (Er-FL) at a repetition rate of 35.2 MHz and an Yb-FL at a repetition rate of 17.6 MHz are synchronized by a phase-locked loop with a two-photon absorption (TPA) detection scheme. The photocurrent noise at a lock-in frequency is removed by CBD. Investigation of the imaging of living cells showed that CBD is effective for sensitivity enhancement of FL-SRS microscopy. In Section 4.1, the principle of the sensitivity enhancement is explained. In Section 4.2, development of the FL-SRS microscope is described in detail. The experiment on subharmonic synchronization is described in Section 4.3. SRS imaging of HeLa cells is then described in Section 4.4. Achievements in this chapter are summarized in Section 4.5.

4.1. Application of CBD to FL-SRS microscopy

SRS microscopy is regarded as a powerful tool for label-free biological imaging [1–7]. However, its use is limited in the laboratory level because of its cost and the low utility of its laser sources. FLs are practical for SRS microscopy [7–9], but these lasers suffer from excess intensity noise, which the ordinary balanced detection cannot sufficiently suppress because of variation of optical transmission of samples, as mentioned in Section 3.1.3. To address this, I employed CBD, taking advantage of its insusceptibility to optical loss in microscopy [10].

Figure 4.1(a) is a schematic of the proposed FL-SRS microscope. A delay-and-add line (DAL), which is a key component of CBD, is included in the pump pulse source

to generate signal and reference pulse trains with orthogonal polarization states. Figure 4.1(b) illustrates the arrangement of pump and Stokes pulse trains. Although in principle, CBD is applicable to SRS microscopy with any lock-in frequency, here we assume that the lock-in frequency is the maximum for obtaining the sensitivity merit of 3 dB, as described in detail in Section 2.3.1. It is important that Stokes pulses be polarized in parallel to pump pulses so that we detect ordinary Raman signals instead of Raman depolarization components.

Equation (3-3) suggests that optimum delay for suppressing noise at a lock-in frequency, i.e., half of the repetition rate of the pump ($f_{\mathrm{rep}}/2$), is $1/f_{\mathrm{rep}}$, which is equal to the pulse period. However, when the delay is precisely matched to the pulse period, both signal pulses and reference pulses interact with Stokes pulses. In order to avoid such unwanted interaction, introducing an additional small delay ($\Delta\tau$) is desirable.

Through the stimulated Raman loss, intensity modulation of the Stokes pulses at $f_{\mathrm{rep}}/2$ is transferred to the signal pulses. After the Stokes pulses are blocked, the signal and reference pulses are detected by a photodetector. The effect of the intensity noise of pump pulses is cancelled by CBD at a lock-in frequency, whereas the transferred modulation can be detected by lock-in technique to obtain the SRS signal.
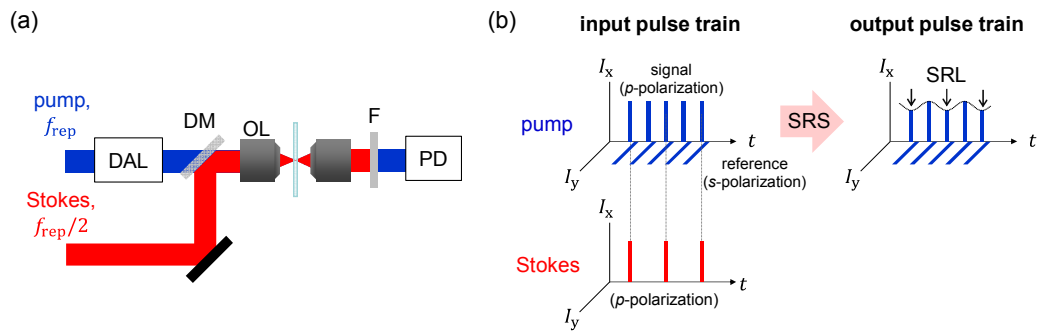

Fig. 4.1. (a) Schematic of SRS microscopy combined with CBD. DM: dichroic mirror, F: Stokes cut filter, PD: photodetector. (b) Possible arrangement of pump and Stokes pulses, which are assumed to be subharmonically synchronized.

4.2. Construction of the microscope system

To demonstrate sensitivity enhancement by CBD, an SRS microscope based on FLs is developed (schematic is shown in Fig. 4.2). The pump pulse source, an Er-FL based pulse source (Section 3.1) with a f_{rep} value of 35.2 MHz, was employed. The delay difference of the DAL was set to ~28 ns to reduce the photocurrent noise at the lock-in frequency ($f_{rep}/2$). A picosecond Yb-doped FL (Yb-FL) was developed for the Stokes pulse source. The Yb-FL was mode-locked by the nonlinear polarization rotation scheme [11]. The f_{rep} value, center wavelength, and bandwidth of the Yb-FL were 17.6 MHz, 1026.7 nm, and 1.54 nm, respectively. A piezoelectric transducer (PZT, MESS-TEK Co., Ltd, MA-140XL) was inserted in the Yb-FL cavity to control the f_{rep} value of the Yb-FL to synchronize to the pump pulse source. Details of the synchronization are described in next section. To equalize the pulse duration and pump pulse, the Yb-FL pulses were introduced into an optical band-pass filter in which the pulse was diffracted by a reflection grating (1200 mm^{-1}) and was filtered by being coupled to a fiber collimator. The filtered pulses were amplified by an Yb-doped fiber amplifier. Consequently, the pulse duration and average power of Stokes pulse were 3 ps and 15 mW, respectively. Figure 4.3 shows the spectra of the Yb-FL pulse and the filtered pulse.

The pump and Stokes pulses were collinearly combined on a dichroic mirror (DM) and focused on a sample by an objective lens (Olympus, ×100, NA 1.4, oil). The transmitted light was collected by another lens (Olympus, ×100, NA 1.4, oil). The sample position was scanned by a three-axis PZT stage. After removal of the Stokes pulses with an optical filter, pump pulses were detected by a Si photodetector (PD; described in Section 3.1) to obtain a photocurrent spectrum near $f_{rep}/2$. The photocurrent was directed to a lock-in amplifier (SR844, Stanford Research Systems) to obtain the SRS signal. The reference signal for lock-in detection was obtained through photodetection of the zeroth diffraction from the grating compressor in the Yb-FL cavity.
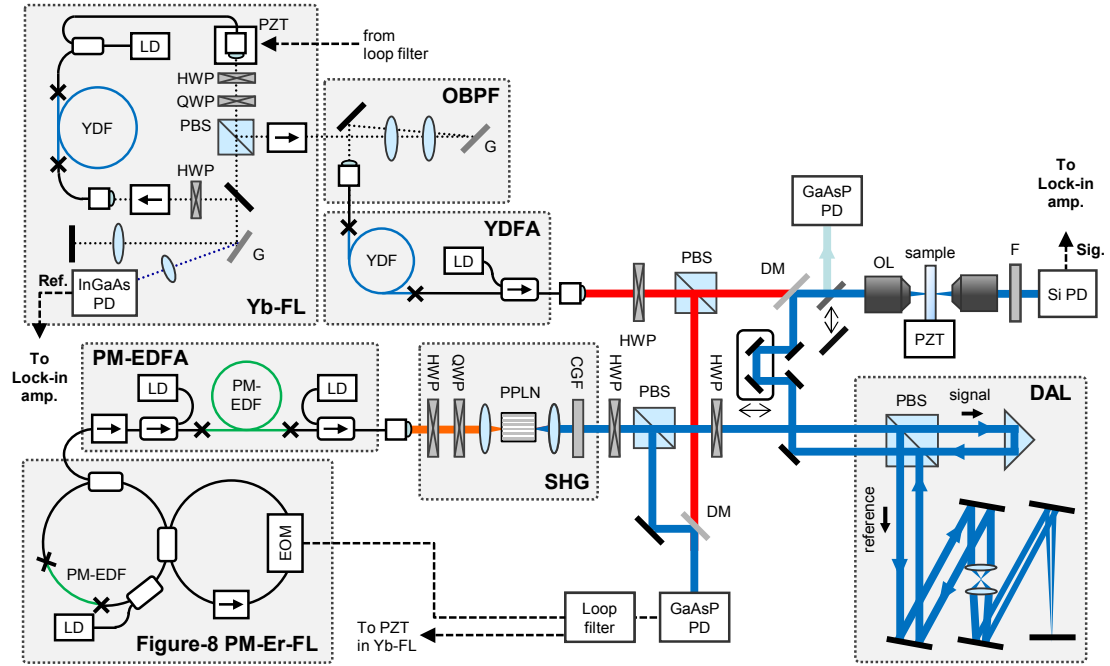
Fig. 4.2. Schematic of the FL-SRS microscope. LD: laser diode, HWP: half wave plate, QWP: quarter-wave plate, PBS: polarization beam splitter, G: reflection grating, DM: dichroic mirror, OL: objective lens, F: Stokes cut filter, PM-EDFA: polarization-maintaining Er-doped fiber amplifier, PPLN: periodically poled LiNbO$_3$, CGF: color glass filter, EOM: electro-optical modulator.
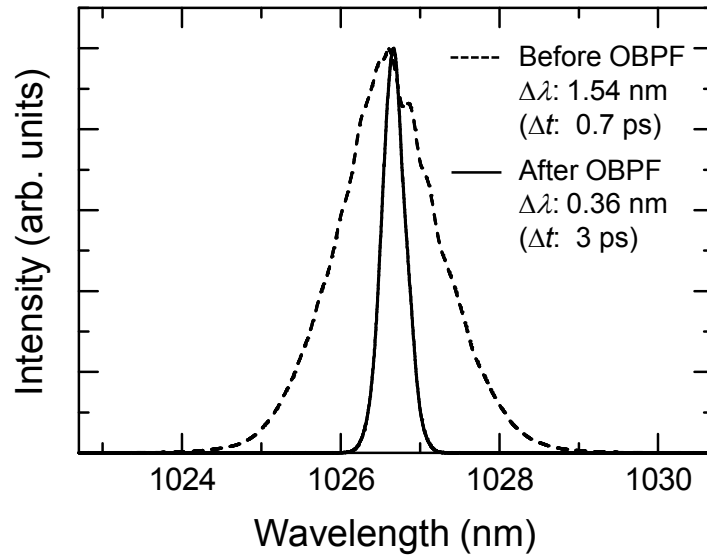

Fig. 4.3. Yb-FL pulse spectra. The dashed line shows the spectrum of the Yb-FL output. The Yb-FL pulse introduced to the OBPF to narrow its bandwidth to equalize the pulse width to that of the pump pulse. The pulse widths are estimated values, which are calculated using time-bandwidth product.

4.3. Subharmonic synchronization between FLs

In SRS microscopy, pump and Stokes pulses have to coincide in time. Therefore, the Er-FL and the Yb-FL should be synchronized. Since the f_{rep} value of the Yb-FL was half that of the Er-FL as shown in Fig. 4.4 (a), we refer to the synchronization of these lasers as subharmonic synchronization. For this synchronization, a phase-locked loop (PLL) with a TPA detection scheme [12, 13] was employed. In this scheme, the TPA photocurrent generated by both the pump and Stokes pulses functions as synchronization error signal, as the TPA reflect the cross correlation between the pump and Stokes pulses. To generate TPA photocurrent, parts of the pump and Stokes pulses were tapped by polarization beam splitters, and then they collinearly impinged on a GaAsP PD (Hamamatsu, G1115). The error signal was fed back to an electro-optic modulator in the Er-FL and to the PZT in the Yb-FL through a loop filter to control their f_{rep} values. Consequently, the GaAsP PD and two FLs function as a phase comparator and voltage-controlled oscillators in PLL circuit, respectively. The error signal was proportionally fed back until the FLs were synchronized. Once synchronization was achieved, an integral control was switched on to achieve tight synchronization [13].

Figure 4.4 (b) shows the TPA signals measured when the PLL was active (red) and was not active (gray). To obtain the synchronization error signal, the TPA signal was biased and the lock point was set at 0 V. Since the TPA signal was approximately 0 V when the PLL was active, it was confirmed that the synchronization was achieved.
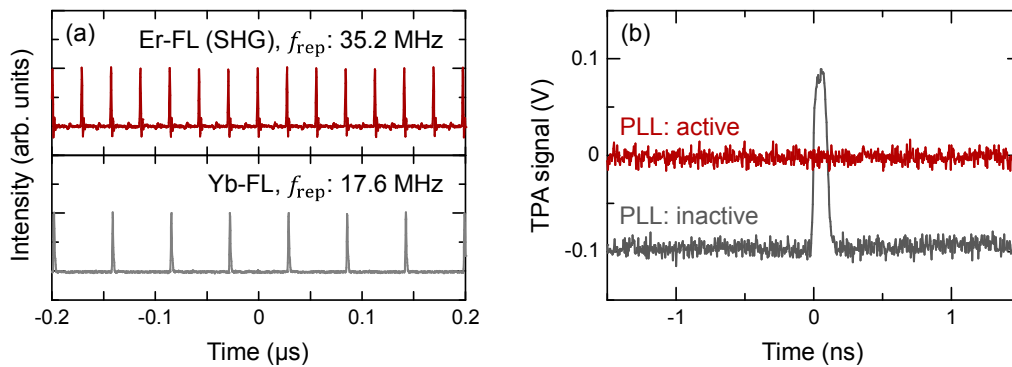
Fig. 4.4. Synchronization experiment. (a) Upper and lower rows show oscilloscope traces of the SHG and Yb-FL pulse trains, respectively. The repetition rate of the Yb-FL is just half that of the Er-FL. (b) TPA signals measured before and after synchronization. The TPA signal was biased with 0.1 V and 0 V was set as a lock point. The center peak of the TPA signal measured before synchronization reflects the cross correlation between the pump and Stokes pulses.

The performance of the synchronization was characterized by measuring in-loop and out-of-loop jitters. The in-loop jitter was measured by the GaAsP PD. The out-of-loop jitter was measured separately by using another GaAsP PD at the input of the microscope. Figures 4.5(a) and 4.5(b) show the error signals and their spectral densities, respectively. The in-loop and out-of-loop jitters were found to be 211 and 227 fs, respectively. The difference between values of these jitters may be caused by intensity fluctuation of the lasers. This is because intensity fluctuation changes the DC bias of the TPA photocurrent, which is converted to timing shift by the PLL. Such a timing shift can only be monitored by out-of-loop jitter measurement. Nevertheless, these jitter values were much smaller than the pulse durations, indicating that precise synchronization was achieved. The central peak in Fig. 4.5(b) indicates that PLL operated with a loop bandwidth of 1.6 kHz.
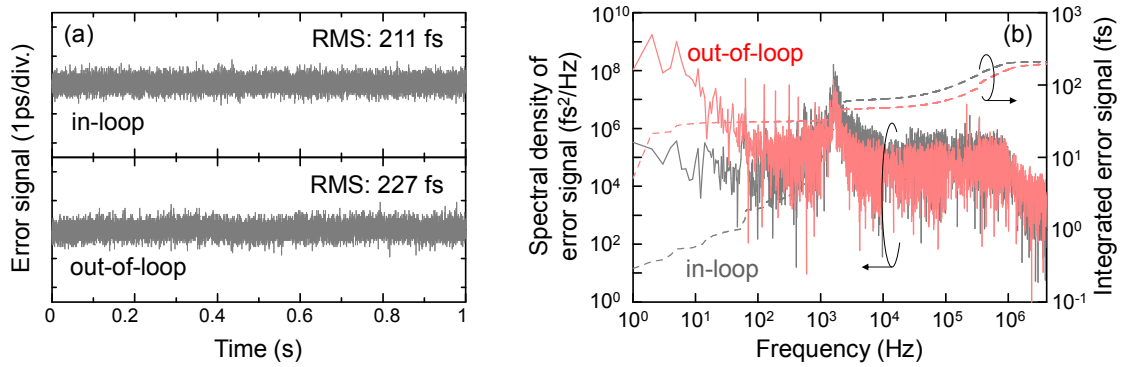

Fig. 4.5. Results of the synchronization experiment. (a) Upper and lower rows show in-loop and out-of-loop error signals in time domain, respectively. (b) Spectral densities of in-loop and out-of-loop error signals are shown by red and gray solid lines, respectively. Dashed lines show integrated error signals with the same colors.

4.4. SRS imaging of HeLa cells

Sensitivity enhancement of FL-SRS microscopy by CBD was investigated through SRS imaging of HeLa cells. The average power of the Stokes pulses at the focus was 4.5 mW. The average power of the pump pulses was dependent on the wavelength, and accordingly, on the Raman shift. Specifically, the average power was 5.4 mW when the Raman shift was 2850 cm^{-1}, which corresponds to CH_2 stretching vibration; and 8.7 mW when the Raman shift was 2950 cm^{-1}, which corresponds to CH_3 stretching vibration. The pixel dwell time was 3 ms.

54

Figure 4.6 shows the experimental results. When CBD is inactive, SRS images look noisy, as shown in Figs. 4.6(a) and 4.6(c). In contrast, when CBD is active, images look less noisy, as shown in Figs. 4.6(b) and 4.6(d). In order to evaluate the improvement in signal-to-noise ratio (SNR), pixel intensities are characterized in areas indicated by boxes in Figs. 4.6(a) and 4.6(c) and in the same area in Figs. 4.6(b) and 4.6(d). Histograms are shown in Figs. 4.6(e) and 4.6(f). Evidently, the distribution became sharper when CBD was used. Root-mean-square values of the background noise in Fig. 4.6(e) when CBD was inactive and active were found to be 19 and 9.8, respectively. Thus, the SNR improvement is ~6 dB, which is in reasonable agreement with the RF noise suppression of 13 dB and the 6 dB SNR drawback of CBD.
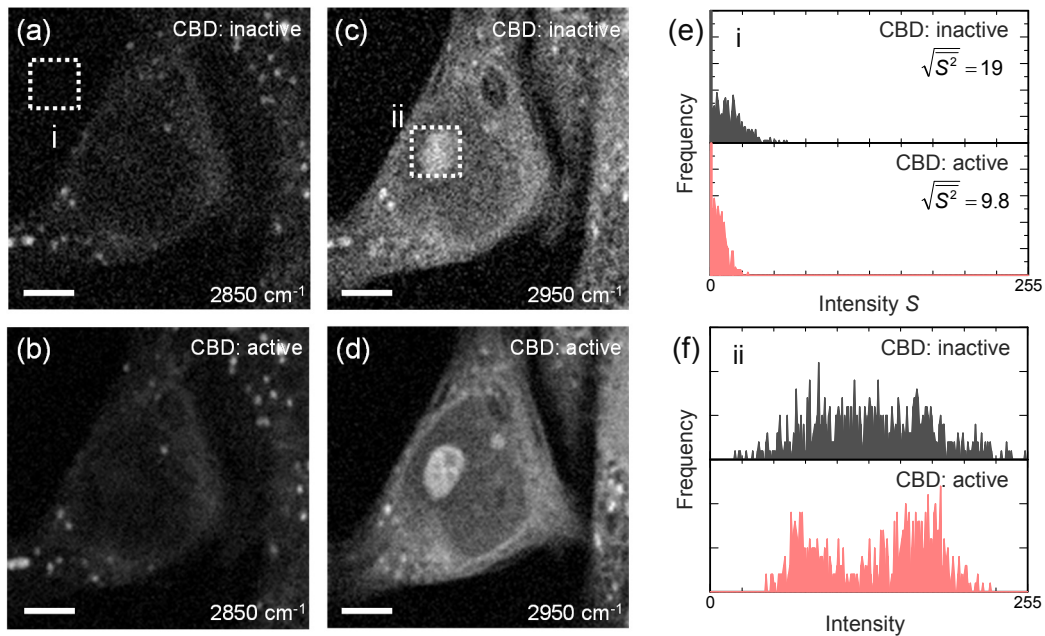
Fig. 4.6. SRS images of a cultured HeLa cell obtained at Raman shifts of 2850 cm^{-1} (a, b) and 2950 cm^{-1} (c, d). Upper and lower rows show the cases in which CBD was inactive and active, respectively. The pixel dwell time was 3 ms. The image size and its number of pixels are 30 μm × 30 μm and 151 × 151 μm^2, respectively. Scale bar is 5 μm. (e, f) Histograms of the pixel intensities of the square areas indicated in (a, c) and the same areas in (b, d). Compared with the case in which CBD is inactive (black), the histogram was markedly sharp when CBD was active (red).

4.5. Conclusion

Sensitivity enhancement of FL-SRS microscopy was demonstrated by using CBD. The Er-FL, which was developed in Section 3.1, was employed as pump pulse source. The picosecond-Yb-FL was developed and used as the Stokes pulse source. These FLs were subharmonically synchronized for SRS microscopy by PLL with a TPA detection scheme. We found the timing jitter to be 227 fs, which was much shorter than the pulse durations, indicating that precise synchronization was accomplished. We then confirmed through SRS imaging of HeLa cells that sensitivity enhancement was achievable through CBD. This demonstration shows the possibility for realizing practical SRS microscopy.

References

[1]   C. W. Freudiger, W. Min, B. G. Saar, S. Lu, G. R. Holtom, C. He, J. C. Tsai, J. X. Kang, and X. S. Xie, *Science* **322** 1857 (2008).

[2]   Y. Ozeki, F. Dake, S. Kajiyama, K. Fukui, and K. Itoh, *Opt. Express* **17**, 3651 (2009).

[3]   P. Nandakumar, A. Kovalev, and A. Volkumar, *New J. Phys.* **11**, 033026 (2009).

[4]   B. G. Saar, C. W. Freudiger, J. Reichman, C. M. Stanley, G. R. Holtom, and X. S. Xie, *Science* **330**, 1368 (2010).

[5]   W. Min, C. W. Freudiger, S. Lu, and X. S. Xie, *Annu. Rev. Phys. Chem.* **62**, 507 (2011).

[6]   Y. Ozeki, W. Umemura, Y. Otsuka, S. Satoh, H. Hashimoto, K. Sumimura, N. Nishizawa, K. Fukui, and K. Itoh, *Nat. Photonics* **6**, 845 (2012).

[7]   C. W. Freudiger, W. Yang, G. R. Holtom, N. Peyghambarian, X. S. Xie, and K. Q. Kie, *Nat. Photonics* **8**, 153 (2014).

[8]   A. Gambetta, V. Kumar, G. Grancini, D. Polli, R. Ramponi, G. Cerullo, and M. Marangoni, *Opt. Lett.* **35**, 226 (2010).

[9]   E. Molotokaite, V. Kumar, C. Manzoni, D. Polli, G. Cerullo, M. Marangoni, *J. Raman Spectrosc.* **44**, 1385 (2013).

[10]   K. Nose, Y. Ozeki, T. Kishi, K. Sumimura, N. Nishizawa, K. Fukui, Y. Kanematsu, and K. Itoh, *Opt. Express* **20**, 13958 (2012).

[11]   M. Hofer, M. E. Fermann, F. Haberl, M. H. Ober, and A. J. Schmidt, *Opt. Lett.* **16**, 502 (1991).

[12]   T. Minamikawa, N. Tanimoto, M. Hashimoto, T. Araki, M. Kobayashi, K. Fujita, and S. Kawata, *Appl. Phys. Lett.* **89**, 191101 (2006).

[13]   Y. Ozeki, Y. Kitagawa, K. Sumimura, N. Nishizawa, W. Umemura, S. Kajiyama, K. Fukui, and K. Itoh, *Opt. Express* **18**, 13708 (2010).

Chapter 5

Development of FL-SRS spectral microscopy

Here, fiber-laser-based stimulated Raman scattering (FL-SRS) spectral microscopy is developed by expanding the functionality of the FL-SRS microscope described in Chapter 4. SRS spectral microscopy has been demonstrated by using a solid-state laser and a wavelength-tunable FL, which were used as pump and Stokes pulse sources, respectively. Here, almost the same Stokes pulse source is employed, and modifications are made to extend the wavelength tunability and to compensate for group delay dispersion (GDD). Development of the modified Stokes pulse source is explained in Section 5.1. In Section 5.2, we constructed a laser scanning SRS spectral microscope by combining the Stokes pulse source with the FL-based pump pulse source, which incorporates fiber delay lines (DLs) for collinear balanced detection (CBD). In Section 5.3, we investigated and compensated for the GDD of the Stokes pulse. SRS spectral imaging and microspectroscopy of polymer beads and HeLa cells are demonstrated in Section 5.4. Achievements in this chapter are summarized in Section 5.5.

5.1. Development of a widely tunable Stokes pulse source

5.1.1. A tunable FL based on the spectral filtering technique

In SRS microscopy, discriminating among several constituents is not always possible because their spectral characteristics can overlap. To distinguish different molecules, SRS spectral images should be acquired by tuning the difference frequency between pump and Stokes pulses [1–7]. A wavelength tunable FL was demonstrated on the basis of the spectral filtering of broadband Yb-doped FL (Yb-FL) pulses [8]. This laser provided a wavelength tunability of ~300 cm^{-1} [2]. However, the Yb-FL was bulky as it included a free-space path as long as ~3.8 m to minimize the length of optical fibers. Hence, the bulky Yb-FL does not share the advantages of typical FLs such as compactness and long-term stability.

Instead of a bulky one, a compact Yb-FL was adapted here as a tunable FL

(schematic is shown in Fig. 5.1). The cavity of the compact Yb-FL was mainly composed of fibers that minimize the free-space path. Mode-locking operation was performed by sending an external signal, which was a sinusoidal function at the same frequency as the repetition rate, to an intracavity electric-optical modulator (EOM, Photline Technologies, NIR-MPX-LN-0.1). Once the laser was mode-locked, pulsing was maintained without any modulation. The EOM and an intracavity piezoelectric transducer (PZT, MESS-TEK Co., Ltd, MA-140XL) were then used to control its repetition rate to synchronize with the pump pulse source [9]. The repetition rate (f_{rep}) was designed to be 25.5 MHz ($f_{rep}/2$) to subharmonically synchronize with the Er-doped FL (Er-FL) (developed in Section 3.2) at a repetition rate of 51.1 MHz. The center wavelength, bandwidth, and output power of the Yb-FL were 1028 nm, 20 nm, and 12 mW, respectively. The Yb-FL pulses were introduced to a wavelength-tunable optical band-pass filter (OBPF) [8] consisting of a galvanometer scanner (GS), relay lenses, a reflection grating (G) with 1200 grooves/mm, and a fiber collimator (FC). In the OBPF, the pulses were diffracted by the grating, and then only a Littrow wavelength component was coupled to the FC. The passband could immediately be changed by changing the angle of the GS. The filtered pulses were introduced to concatenated polarization-maintaining Yb-doped fiber amplifiers (PM-YDFAs).
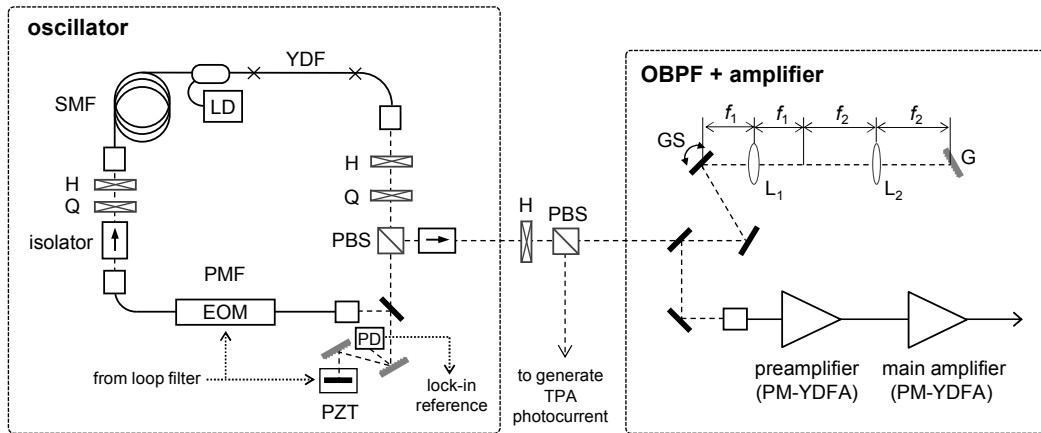

Fig. 5.1. Schematic of the tunable FL. SMF: single-mode fiber, YDF: Yb-doped fiber, PMF: polarization-maintaining fiber, H: half-wave plate, Q: quarter-wave plate. PD: photodetector, f_1 = 100 mm, f_2 = 150 mm.

Figure 5.2 shows output spectra from the developed tunable FL. The wavelength tunability was ~20 nm (~190 cm^{-1}) [10]. The optical power was ~100 mW at a wavelength of 1030 nm. The tunability was narrower than that in the previous one by a factor of ~1.6. Presumably, the difference in the pulse energy of the oscillator output mainly contributed to the difference in the tunability. Figure 5.3 shows the possible reason for the narrowing the wavelength tunable range. When the pulse energy is low and the passband is in the wing of the gain spectrum, a broadband amplified spontaneous emission (ASE) noise is imposed at the center of the gain spectrum in the preamplifier. If the optical power of the ASE is comparable to that of the filtered pulses, then the main amplifier may be saturated by the ASE before the filtered pulses are sufficiently amplified. This causes narrowing of the wavelength tunability.
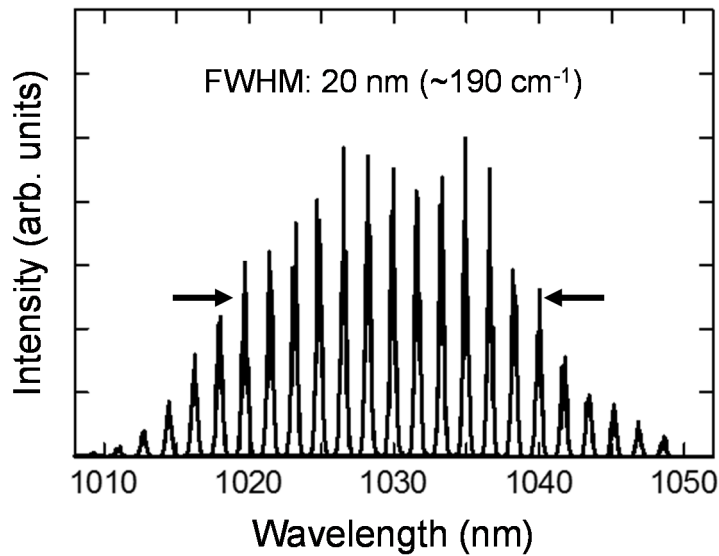

Fig. 5.2. Wavelength tunable range of the compact tunable FL. This spectrum is merged with various filtering spectra.
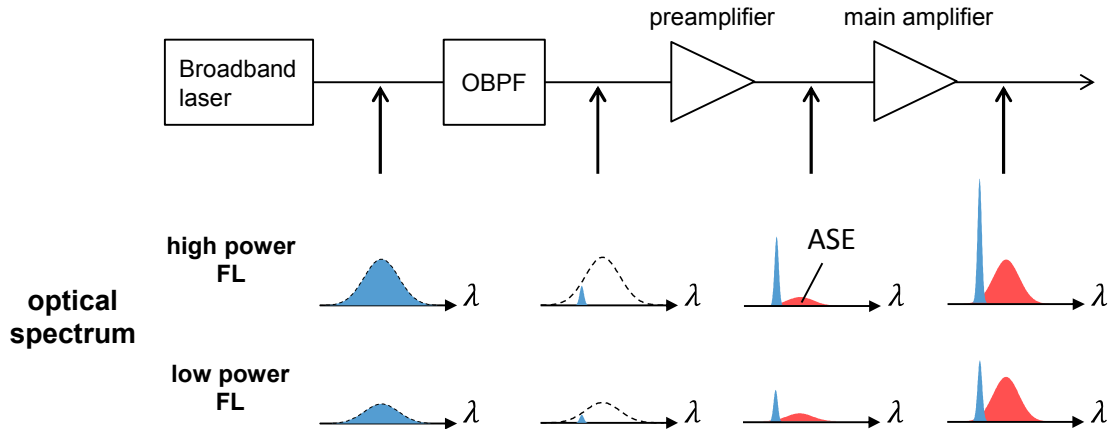
Fig. 5.3. The possible reason for the narrowing of the wavelength tunable range. The schematic shows the basic configuration of the wavelength tunable source and optical spectra at the position directed by allows when the filtered wavelength is in the wing of the FL spectrum. When the high-power FL is employed as the oscillator, the filtered pulse is sufficiently amplified. On the other hand, when the low-power FL is used, the main amplifier is saturated by ASE originated from the preamplifier before the filtered pulse is sufficiently amplified.

5.1.2. Proposal of a double-pass filtering scheme to extend the tunability

As described in the previous section, a wavelength-tunable pulse source using a low-power FL oscillator suffers from a narrow tuning range. If ASE that saturates subsequent amplifiers is removed, then the tunability may be extended. To this end, I propose a new scheme for the OBPF [11], in which preamplified pulses are introduced again into the OBPF to remove ASE. Figure 5.4 shows a schematic of the double-pass OBPF (DP-OBPF). Pulses from the Yb-FL are introduced into an OBPF through a polarization beam splitter (PBS). A Littrow wavelength component is then coupled to a preamplifier through another PBS. Preamplified pulses are then again coupled to the OBPF with orthogonal polarization state by the first PBS. The second path is almost the same as the first path, but it is slightly shifted vertically to avoid unwanted interference and lasing between PM-YDFAs. Second-pass pulses are then introduced into a main amplifier by the second PBS.

Figure 5.5 shows output spectra from the tunable FL combined with the DP-OBPF. The wavelength tunability was extended to ~30 nm (~280 cm^{-1}). The spectral widths were approximately ~0.4 nm (~4 cm^{-1}). The optical power was ~100 mW at a wavelength of 1030 nm. Notably, the wavelength tunability was broader than the bandwidth of the Yb-FL. This is because the gain saturation of the main amplifier maintained the output power at a nearly constant value over a broadband range. Thus, we confirmed that the DP-OBPF effective extends the wavelength tunability.
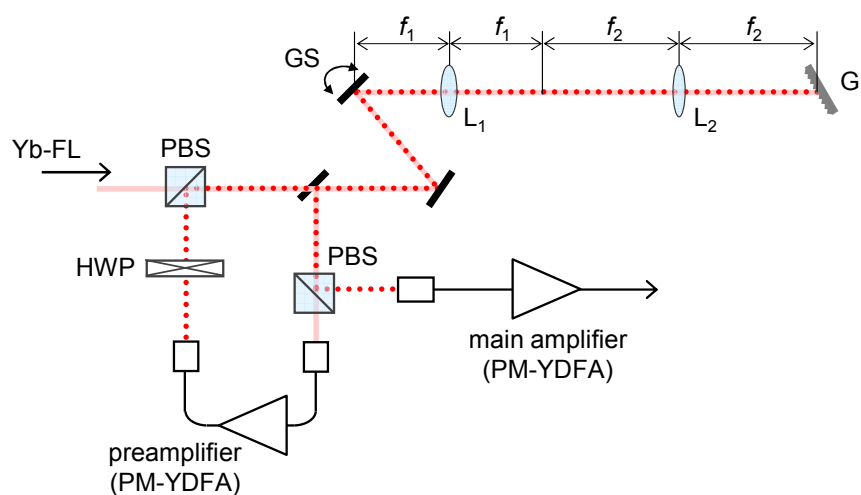
Fig. 5.4. Schematic of the DP-OBPF. Solid line: first path. Dotted line: second path.
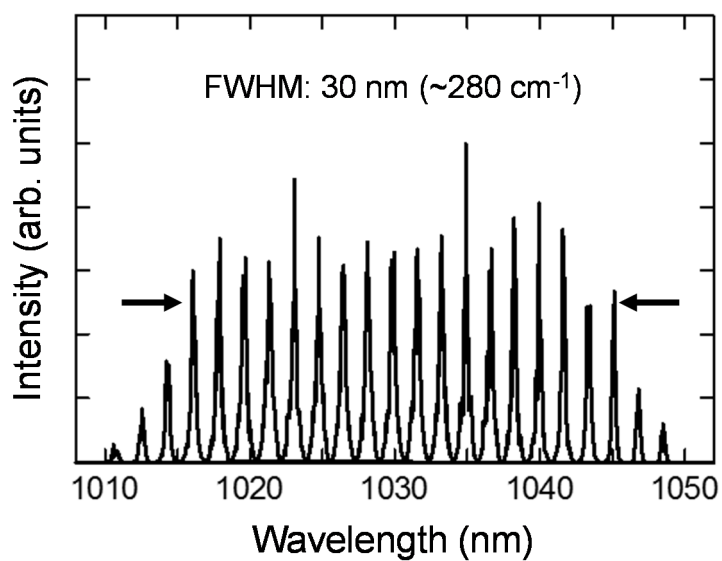

Fig. 5.5. Extended wavelength range of the tunable FL. This spectrum is merged with various filtering spectra.

5.2. Microscope setup

A FL-SRS spectral microscope is constructed by combining the tunable Stokes pulse source with the pump pulse source, which was developed based on an Er-FL (Section 3.2). A schematic of the microscope setup is shown in Fig. 5.6. A fiber-based CBD [11] was employed to enhance the sensitivity. The delay difference of the fiber-based delay-and-add line (DAL) was set to 19.5 ns so that the photocurrent noise at a lock-in frequency of $f_{rep}/2$ was suppressed.

The pump pulse source was subharmonically synchronized with the tunable Stokes pulse source by a phase-locked loop with intracavity modulators and a two-photon absorption detector [9, 11]. Parts of the pump and the Yb-FL output were tapped by PBSs. They were connected to a GaAsP-photodetector (PD) (Hamamatsu, G1115) to generate two-photon absorption (TPA) photocurrent, which functioned as an error signal. The TPA photocurrent was fed back to the EOM and the PZT in the Yb-FL through a loop filter to control its repetition rate. In this manner, the Er-FL and Yb-FL were subharmonically synchronized.

The pump and Stokes pulses were overlapped in time and space by an optical DL and a dichroic mirror (DM), respectively. These pulses were introduced into a laser scanning microscope. A microscope objective (Olympus, 60×, NA 1.2, water) was used to focus the pulses in the sample. The transmitted light was collected by another lens (Olympus, 60×, NA 1.2, water).

After Stokes pulses were removed by an optical short-pass filter, pump pulses were detected by the Si PD, which was used in Section 3.2. The SRS signal was then measured with a high-speed lock-in amplifier (LIA) fabricated in-house. The reference signal for lock-in detection was obtained with a photodetector in the Yb-FL.
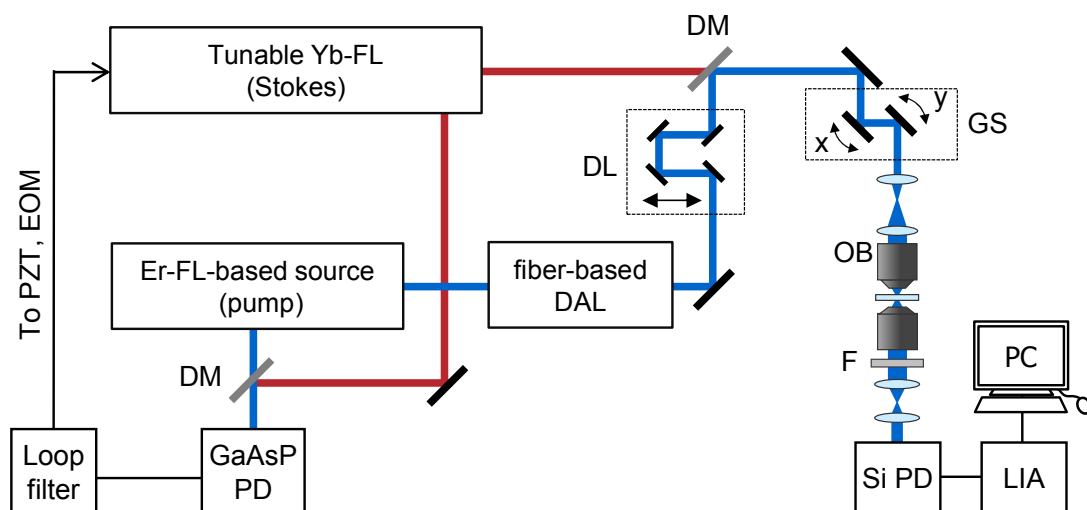
Fig. 5.6. Schematic of FL-SRS spectral microscopy. OB: objective lens, F: short-pass filter.

5.3. Compensation for group delay dispersion of the Stokes pulse

When we carried out SRS spectroscopy of polymer beads (poly (methyl methacrylate) (PMMA) and polystyrene (PS)) using the developed system, we noticed that the SRS signal weakened when the wavelength of the Stokes pulse was in the wing of the tunable range. Furthermore, the obtainable Raman spectral range was shifted when a time delay was given to the pump pulse. Figure 5.7 (a) and (b) show the measured SRS spectra, which were obtained by adjusting the time delay of the pump pulses so that SRS signals at wavenumbers of 2950 cm^{-1} and 3050 cm^{-1} become maximum, respectively. This narrowing may be caused by the wavelength-dependent delay difference of the Stokes pulse, i.e., GDD. As shown in Fig. 5.8, GDD causes a timing mismatch between pump and Stokes pulses, leading to narrowing of the effective tunable range. Thus, compensating for GDD is crucial to SRS spectral microscopy. Although the exact origin of GDD is still unclear, it might have originated from the Yb-FL pulse and from group-velocity dispersion of the fiber amplifiers.
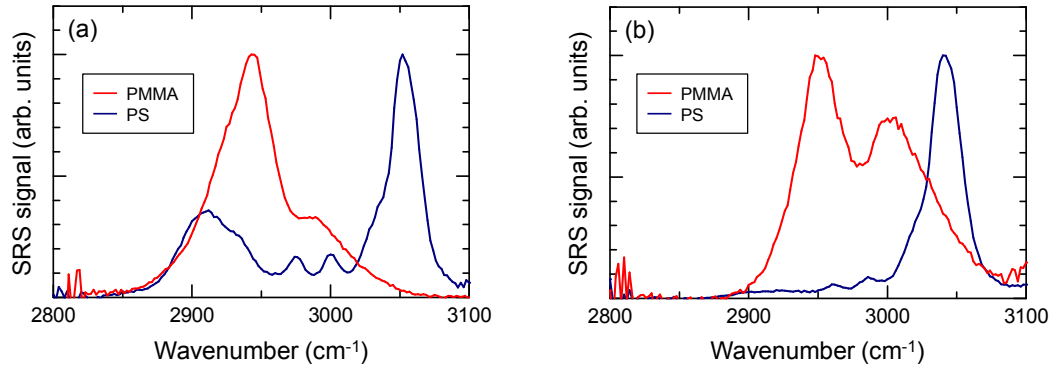
Fig. 5.7. The shift of the obtainable Raman spectral range due to a time delay of the pump pulses. Red and blue lines show SRS spectra of PMMA and PS beads. The time delay of pump pulses is adjusted so as to optimize the SRS signal at wavenumbers of (a) 2950 cm^{-1} and (b) 3050 cm^{-1}. The spectra are normalized by each maximum value of the SRS signal.
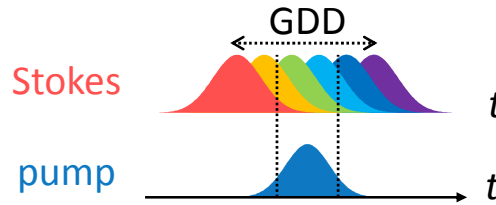
Fig. 5.8. The limitation of the effective wavelength tunable range by GDD. When the Stokes pulse has GDD, the pulse timings change depending on the passband wavelength. This leads to the limitation of the effective wavelength tunable range due to the timing mismatch between the pump and Stokes pulses.

I propose a simple method using DP-OBPF to compensate for GDD. Figure 5.9 illustrates the vicinity of the grating in the OBPF to show the proposed method. By shifting the OBPF's grating position, group delays are given to pulses depending on the wavelength; when the grating position is shifted backward, the path length of pulses with longer wavelengths increases, and vice versa.

Here, the DP-OBPF gives positive dispersion to the pulses, cancelling the negative dispersion of the Stokes pulse. The GDD of the Stokes pulse is then investigated. The method for GDD measurement is explained as follows: If the Stokes pulse has GDD, then SRS spectral intensity decreases depending on the timing mismatch. When the timing shift is given to the pump or Stokes pulses, thereby increasing the SRS spectral intensity to maximum, the amount of timing shift corresponds to the group delay at the wavelength. The amounts of the timing shift are subsequently measured. GDD is calculated by using the measured group delays.

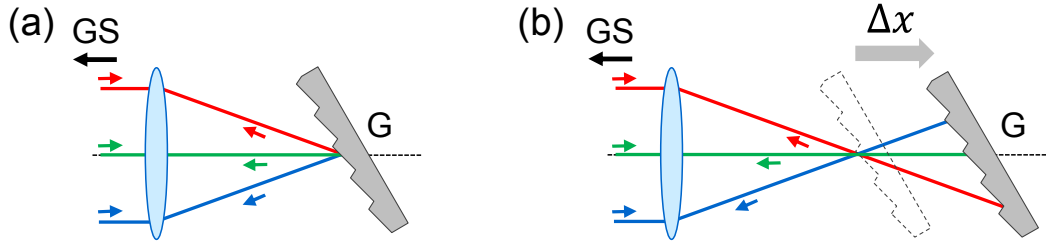**Fig. 5.9.** GDD compensation using OBPF. The image shows the vicinity of the grating in OBPF. (a) Group delays are constant with respect to the passband with the conventional setup. (b) Position shift of the grating give GDD to the pulses.

A PS bead was used as SRS signal source. The timing shift was given to the pump pulses by the DL. As strong SRS responses could be obtained from PS at Raman shifts of 2900, 2950, and 3050 cm^{-1}, the group delays were measured at corresponding wavelengths. Specifically, the wavelengths of Stokes pulses were set to 1020, 1025, and 1036 nm, while that of the pump was set to 787 nm. The pump wavelength was tuned by controlling the temperature of the periodically poled LiNbO$_3$ crystal.

Figure 5.10(a) shows the measured group delays with the various grating displacements, Δx. The inset shows measured GDD as a function of Δx and its fitting line (dashed line). The slope of the fitting line, which shows the amount of GDD per unit displacement, is 6.0 ps/nm/m. This is in rough agreement with the calculated value of 8.0 ps/nm/m (See Appendix B in detail). The possible reason for this difference may be the residual misalignment of the GS and of the relay lenses in the DP-OBPF.

Although we can compensate for the GDD by shifting the grating position, there is a tradeoff between the wavelength tunability and GDD compensation. Figure 5.10(b) shows output spectra, which were measured after GDD compensation. The wavelength tunability reached 230 cm^{-1} probably because of degradation of the coupling efficiency of the FCs according to the wavelength. The propagating direction of the pulses in the OBPF is slightly tilted in the vertical direction against the optical axis of the relay lenses to pick up the reflection of the grating. Since the grating shift gives different path lengths to pulses, the positions of the beam at the FCs are also slightly shifted vertically according to the wavelength. As a result, the coupled optical power in the wing of the Yb-FL spectrum weakens relative to that near the center spectrum. This may lead to narrowing of the wavelength tunability. Nevertheless, GDD compensation by the OBPF was successfully accomplished.
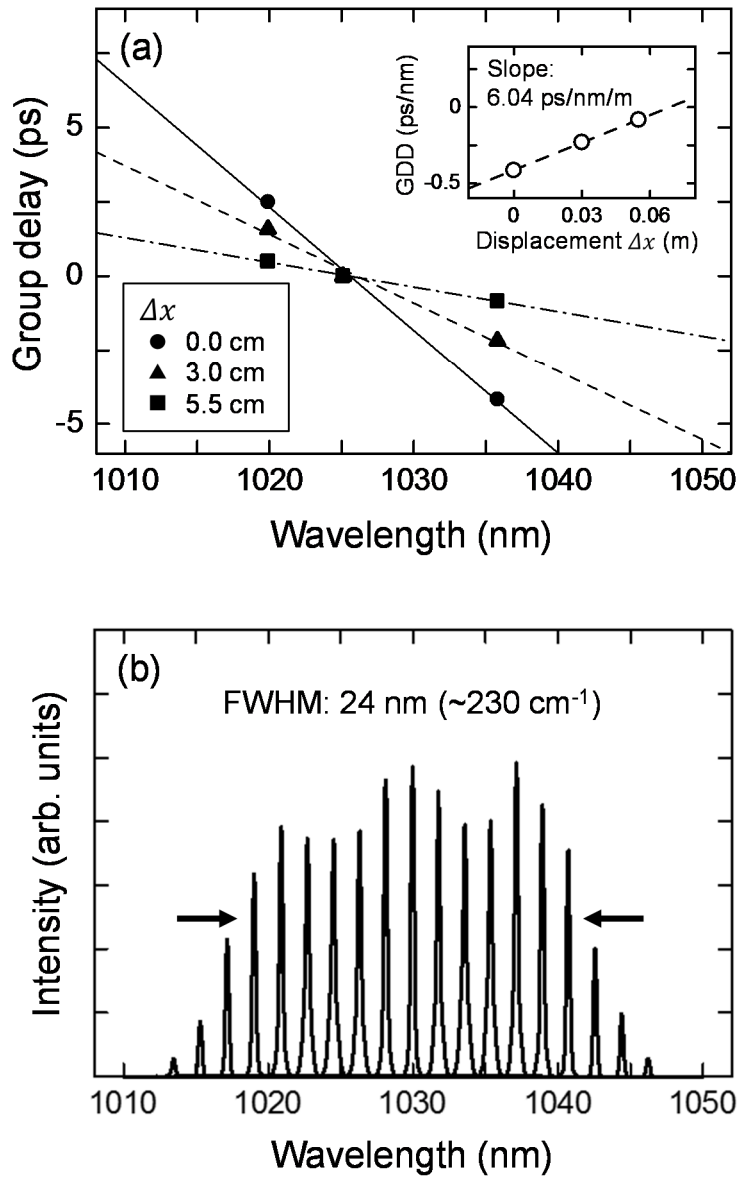
Fig. 5.10. Results of the experiment on GDD compensation. (a) Measured group delays with various grating displacements. The inset shows measured GDD as a function of the grating displacement, Δx. (b) Spectra of the wavelength-tunable source with GDD compensation when Δx was 5.5 cm.

5.4. Spectral imaging and microspectroscopy

The performance of the FL-SRS spectral microscope was characterized through spectral imaging and microspectroscopy. The sample was a mixture of 6 μm PMMA beads and 4.5 μm PS beads. The optical powers of the pump and Stokes pulses were ~6 and ~20 mW, respectively.

First, SRS spectral images were obtained in the wavenumber range of 2900 to 3050 cm^{-1} in steps of 50 cm^{-1}. Figures 5.11(a)–5.11(d) show the obtained SRS images. We can see a clear difference in image contrast dependent on the wavenumber. The pixel number and pixel dwell time were 256 × 256 pixels and 10 μs, respectively. As the total acquisition time was ~0.8 s/frame, the system could perform real-time imaging at high signal-to-noise ratio (SNR).

Next, SRS spectra of the polymer beads were obtained. Figure 5.11(e) shows SRS spectra of the PMMA and PS beads, which were obtained at locations indicated by red and blue arrows in Fig. 5.11(a), respectively. Scanning was done in the range of 2800 to 3100 cm^{-1} in wavenumber steps of 3 cm^{-1}. The acquisition time was set to be as long as 10 ms per step to achieve high SNR. Thus, a single scan was performed within ~1 s. The results show the intrinsic vibrational spectra of PMMA and PS, which caused the contrast of spectral images. Further reduction of the acquisition time is possible at the expense of SNR, but it is limited by the response time of the GS in the OBPF. For comparison, SRS spectra were obtained at an acquisition time of 100 μs per step, as shown in Fig. 5.11(f). Compared with those of the spectra shown in Fig. 5.11(e), the SNR is low, but we can obtain SRS spectra with a much shorter time (~15 ms). Note that these spectra were obtained from different experiments under the same experimental conditions except for the wavenumber steps (2 cm^{-1}).
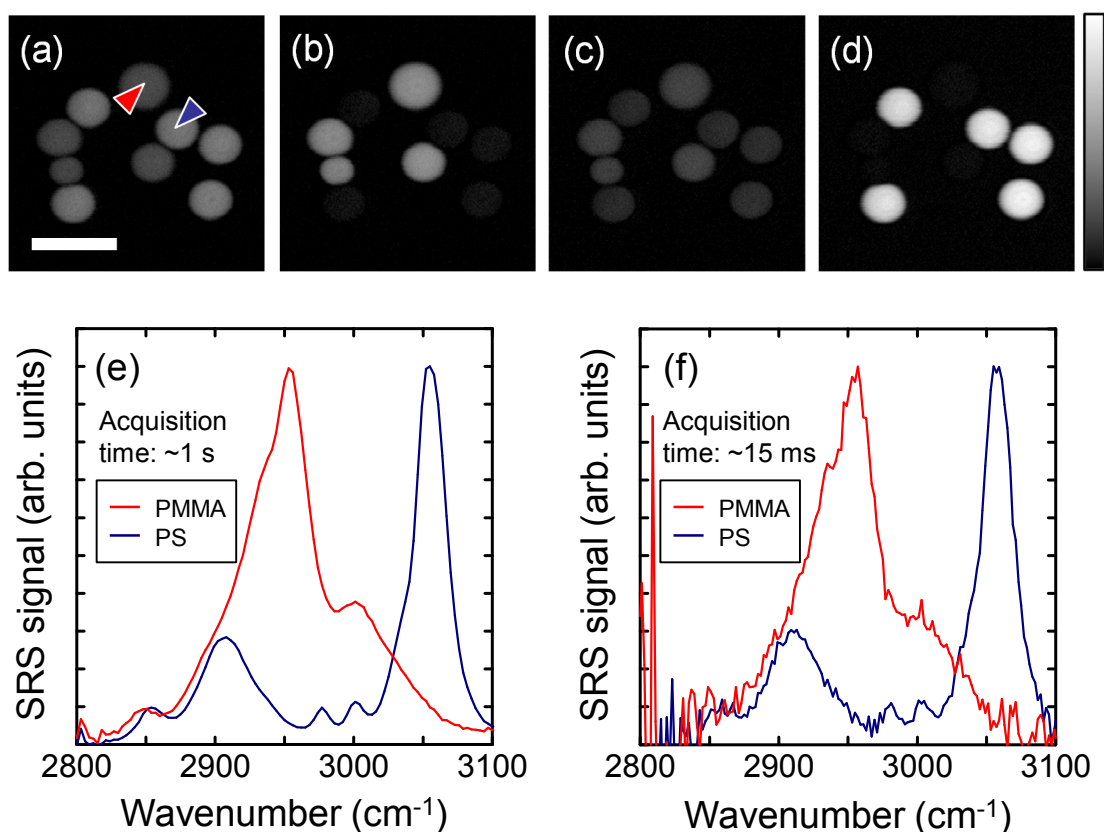
68

Fig. 5.11. SRS spectral images of PMMA and PS beads obtained at wavenumbers of (a) 2900, (b) 2950, (c) 3000, and (d) 3050 cm^{-1}. Pixel dwell time: 10 μs, number of pixels: 256 × 256, image size: 30 × 30 μm^2, pump: 6 mW, Stokes: 20 mW, scale bar: 10 μm. (e) SRS spectra of PMMA and PS obtained at the locations indicated by the red and blue arrows, respectively. Wavenumber range: 2800–3100 cm^{-1}, wavenumber steps: 3 cm^{-1}; signal acquisition time per step: 10 ms per step, pump: 6 mW, Stokes: 20 mW. (f) SRS spectra of PS and PMMA beads obtained in a different experiment with the same experimental conditions except for the wavenumber steps (2 cm^{-1}) and signal acquisition time per step (100 μs).

To further confirm the performance, HeLa cells cultured on a coverslip were observed. The pixel number of images and pixel dwell time were 512 × 512 pixels and 30 μs, respectively. The total acquisition time was ~10 s/frame. The optical powers of the pump and Stokes pulses were ~7 and ~50 mW at the focus, respectively. Figure 5.12(a) shows the lipid distribution based on the CH$_2$ stretching mode (2850 cm^{-1}). Figure 5.12(b) was visualized by targeting the CH$_3$ stretching mode (2930 cm^{-1}), which reflects both protein and lipid. Intensities of the images were normalized by each maximum. We can clearly see lipid droplets (LDs) in Fig. 5.12(a), as well as cytoplasmic and nucleus regions in Fig. 5.12(b). SRS spectra of a LD and a nucleus were also obtained. Scanning was done

in range of 2830 to 3050 cm^{-1} in wavenumber steps of 2 cm^{-1}. The acquisition time was set to 10 ms/step to achieve high SNR. Note that the sample was photodamaged at an optical power higher than 20 mW, when a single point was irradiated for microspectroscopy without scanning the focal point. Hence, the optical power of the Stokes pulse was reduced to 20 mW. Figure 5.12(c) shows SRS spectra obtained from a different cell on the same coverslip. The blue line shows the spectrum obtained from the nucleus, reflecting both protein and water. The red line shows the Raman spectrum obtained from the LD. We can clearly see the difference in their spectral shape. Compared with the original Raman spectrum of lipids in cells [1], the peak reflecting CH_2 stretching vibration is weak and the peak reflecting CH_3 stretching vibration is strong. Presumably, this is because of effect of the cytoplasm near the measured LD on the obtained spectrum due to its relatively large focal spot. Nevertheless, SRS spectral imaging by FL-SRS spectral microscopy with shot-noise sensitivity was successful.

5.5. Conclusion

A widely tunable FL-SRS spectral microscope has been developed. A DP-OBPF was proposed to realize wide tunability. Its effectiveness was confirmed through an experiment in which the tunability was extended from ~190 cm^{-1} to ~280 cm^{-1}. Spectral microscopy was performed by combining the tunable FL with an Er-FL-based pump pulse source. The DP-OBPF was also used to compensate for the GDD of the tunable FL. The wavelength tunability of the developed source reached ~230 cm^{-1} because of the tradeoff between GDD and the tunable range; nevertheless, this was sufficient to cover the region for CH stretching vibration, as confirmed through spectral imaging of polymer beads and of living samples. Notably, these results show that FL-SRS microscopy can compete with leading-edge SRS microscopy based on solid-state lasers [2], in terms of sensitivity and tunability of the Raman shift.
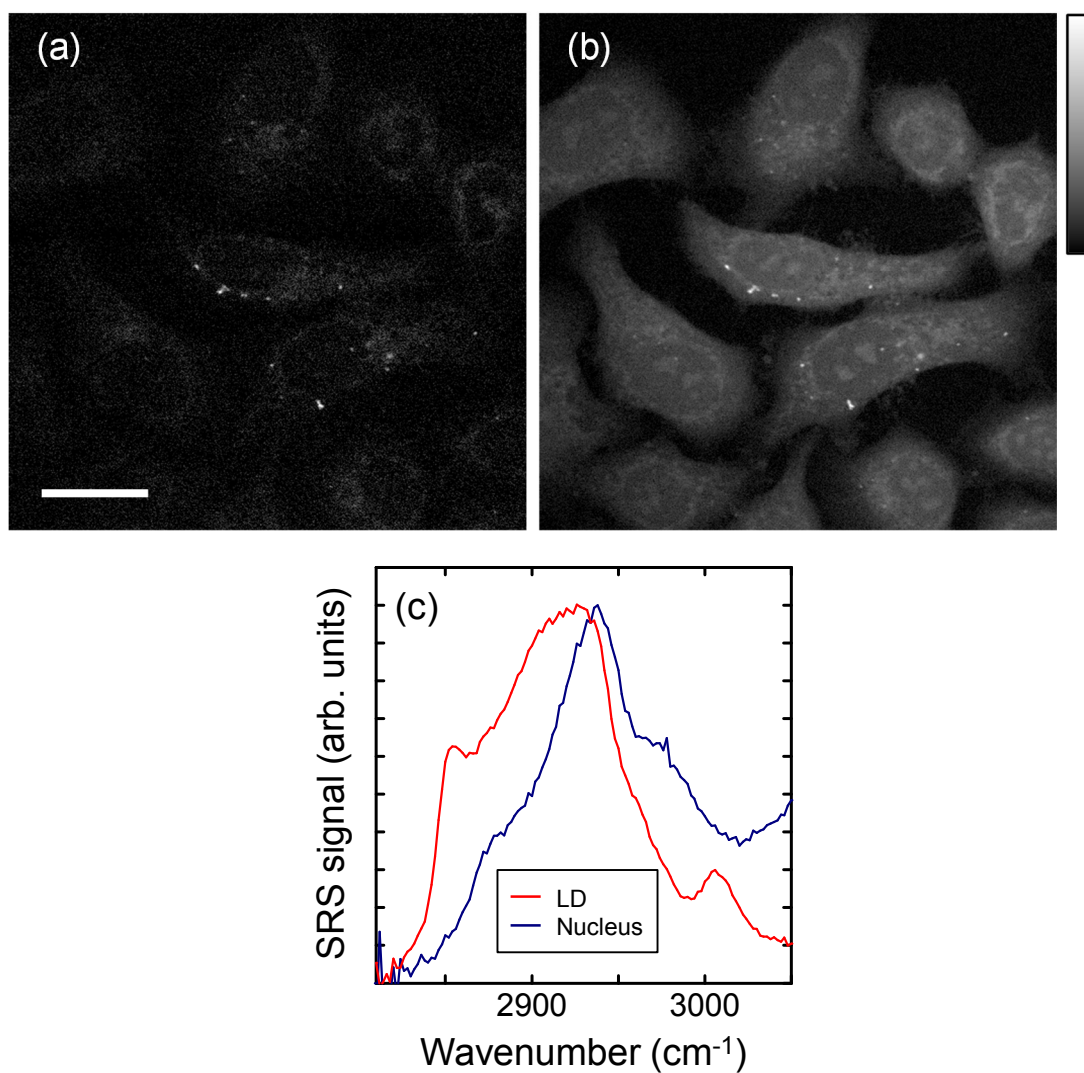
Fig. 5.12. SRS images of cultured HeLa cells obtained at wavenumbers of (a) 2850 and (b) 2930 cm^{-1}. Pixel dwell time: 30 μs, number of pixels: 512 × 512, image size: 100 × 100 μm^2, pump: 7 mW, Stokes: 50 mW, scale bar: 20 μm. (c) SRS spectra obtained from a LD (red) and nuclei (blue) of different cells on the same coverslip. Signal acquisition time: 10 ms/step, scanning range: 2830–3050 cm^{-1}, wavenumber step: 2 cm^{-1}, pump: 7 mW, Stokes: 20 mW.

References

[1] F. -K. Lu, M. Ji, D. Fu, X. Ni, C. W. Freudiger, G. Holtom, and X. S. Xie, *Mol. Phys.* **110**, 1927 (2012).

[2] Y. Ozeki, W. Umemura, Y. Otsuka, S. Satoh, H. Hashimoto, K. Sumimura, N. Nishizawa, K. Fukui, and K. Itoh, *Nat. Photonics* **6**, 845 (2012).

[3] K. Wang, D. Zhang, K. Charan, M. N. Slipchenko, P. Wang, C. Xu, and J. X. Cheng, *J. Biophotonics* **6**, 815 (2013).

[4] D. Fu, G. Holtom, C. Freudiger, X. Zhang, and X. S. Xie, *J. Phys. Chem. B* **117**, 4634 (2013).

[5] D. Zhang, P. Wang, M. N. Slipchenko, D. B-. Amotz, A. M. Weiner, and J. -X. *Cheng, Anal. Chem.* **85**, 98 (2013).

[6] L. Kong, M. Ji, G. R. Holtom, D. Fu, C. W. Freudiger, and X. S. Xie, *Opt. Lett.* **38**, 145 (2013).

[7] K. Seto, Y. Okuda, E. Tokunaga, and T. Kobayashi, *Rev. Sci. Instrum* **84**, 083705 (2013).

[8] Y. Ozeki, W. Umemura, K. Sumimura, N. Nishizawa, K. Fukui, and K. Itoh, *Opt. Lett.* **37**, 431 (2012).

[9] Y. Ozeki, Y. Kitagawa, K. Sumimura, N. Nishizawa, W. Umemura, S. Kajiyama, K. Fukui, and K. Itoh, *Opt. Express* **18**, 13708 (2010).

[10] K. Nose, Y. Ozeki, T. Kishi, K. Sumimura, Y. Kanematsu, and K. Itoh, *Proc. SPIE* **8588** (2013).

[11] K. Nose, T. Kishi, Y. Ozeki, Y. Kanematsu, H. Takata, K. Fukui, Y. Takai, and K. Itoh, *Jpn. J. Appl. Phys.* **53**, 052401 (2014).

Chapter 6

Conclusion

To realize practical stimulated Raman scattering (SRS) microscopy, a fiber-laser-based SRS (FL-SRS) spectral microscope is developed in this thesis. Achievements in each chapter are summarized as follows. The outlook is then discussed.

Summary

Chapter 1 is dedicated to the introduction of this thesis. The development of label-free imaging technique is indispensable in biology and medicine. Stimulated Raman microscopy is introduced as a key technology for label-free imaging. It is desirable in SRS microscopy that the microscope system is more practical and its molecular specificity is enhanced for its use in practice. The replacement of solid-state lasers by FLs and spectral imaging are attractive. To realize them, the technical issues were discussed.

Chapter 2 is presented to better understand this work. Here, fundamental theories related with the phenomena using in this thesis were explained. The interference effects was described to give the detailed explanation to the generation of optical pulse, coherent Raman scattering, and excess intensity noise, which hinders the use of FLs in SRS microscopy. In particular, spectral interference was explained to show the fundamental model of *collinear balanced detection* (CBD), which is proposed in Chapter 3. The difference between spontaneous Raman scattering and SRS was briefly introduced by showing the classical model of the relation between external electric fields and molecules. The principle of SRS microscopy was explained in detail. The sensitivity of SRS microscopy with respect to unavoidable photocurrent noises and the excess intensity noise of practical laser sources were discussed.

In Chapter 3, a new balanced detection technique, CBD, is proposed. CBD can suppress the photocurrent noise that comes from the intensity noise of optical pulses at a specific RF frequency by utilizing the interference of photocurrents. An important advantage over the ordinary balanced detection is its insusceptibility to optical loss. This feature may be effective for sensitive detection of SRS signals even when noisy optical

pulses are used. Experimentally, high-frequency noise originated from a FL-based pulse source was down to the shot-noise limit, indicating the effectiveness of CBD. Moreover, the compact CBD was then developed by replacing a free-space delay lines with polarization-maintaining fiber delay lines. It was confirmed that nonlinear spectral broadening, which is an important issue in fiber-based CBD, was negligible even when the average power of the laser source was sub-hundred milliwatt level sufficient for SRS microscopy. In this manner, the effectiveness of CBD in high-frequency noise suppression was demonstrated.

It was also demonstrated in Chapter 3 that CBD is general concept. The generality was investigated by applying into optical noises instead of optical pulses. It was experimentally confirmed the photocurrent spectrum is modulated with a modulation depth of 0.5, although interference between randomly polarized optical noises may not occur. The fringe period is inversely proportional to the delay as well as conventional spectral interferometry. This phenomenon is also supported by theoretical analysis. These demonstration show that photonic RF spectral modulation, which is a theoretical foundation of CBD, is a general concept, indicating the possibility of the wide application of the proposed technique.

In Chapter 4, a FL-SRS microscope with shot noise limited sensitivity was developed by applying CBD. In the demonstration, an SRS microscope was constructed from subharmonically synchronized Er- and Yb-doped FLs, which were oscillators to generate picosecond pump and Stokes pulse trains, respectively. For the synchronization between two FLs, a phase-locked loop with a two-photon absorption detection scheme was employed, resulting in sufficiently tight synchronization for SRS microscopy. The signal-to-noise ratio (SNR) was clearly improved by application of CBD, as confirmed by SRS imaging of HeLa cells. This demonstration indicates the possibility of practical SRS microscopy by the use of the FLs. It should be noted that this is the first study of FL-SRS microscopy with shot-noise-limited sensitivity.

In Chapter 5, SRS spectral microscopy was performed by extending the FL-SRS microscope. Wide-wavelength tunability is one of the most important requirements of SRS spectral imaging. Here, I propose the double-pass type optical band-pass filter (DP-OBPF) to develop a compact and rapidly tunable FL pulse source with extended

wavelength tunability. Compared with previous technique, which employs a single-pass type OBPF, the tunability was extended by a factor of 1.5 (from 190 to 280 cm^{-1}), indicating the effectiveness of the proposed technique. I also propose a simple method for GDD compensation using a DP-OBPF. The demonstration of the proposed method shows its effectiveness. By the combination of the developed-wavelength tunable source and a FL-based pulse source as for Stokes and pump sources, respectively, spectral imaging and spectroscopy of both polymer beads and HeLa cells were performed. The obtained spectra show good agreement with their original spectra and image contrasts, indicating successful development of the FL-SRS microscope with shot noise limited sensitivity and enhanced molecular specificity. The developed FL-SRS microscope can compete with leading-edge SRS microscopes using solid-state lasers.

To summarize, the work described in this thesis form a technical foundation for practical SRS microscopy with high sensitivity and high functionality. This research may open up SRS microscopy to non-professional researchers such as biologists and physicians, encouraging rapid growth of the label-free imaging technology based on vibrational spectroscopy.

Future outlook

In this thesis, practical SRS microscopy was developed. Issues that remain concern (1) the imaging speed, (2) the wavelength tunability for accessing other Raman bands, and (3) the practicality of the laser system. However, it may be possible to solve these issues by applying existing technologies. Approaches to solve these issues are discussed below.

(1)   *Imaging speed*

High imaging speed avoids artifacts and blurs due to sample motion during observation of living samples. To achieve high imaging speed with the FL-based system, there are two possible solutions.

One is the improvement of wavelength conversion efficiency. In our pump pulse source, only a portion of the fundamental pulse energy contributes to the narrowband second-harmonic-generation (SHG) pulses. This is because broadband pulses were used as fundamental pulses for SHG. As a result, the conversion efficiency was as low as

~12 %. If we could employ a narrowband FL oscillator as a fundamental pulse source, the conversion efficiency might be improved. Such a narrowband FL oscillator is achievable with the use of an optimized saturable absorber in the cavity [1].

The other solution is the use of a high-power and low-noise FL oscillator as the fundamental pulse source. Such an oscillator does not need strong optical amplification to generate high-power picosecond-SHG pulses, leading to superior noise performance. In such case, we do not have to employ CBD and we avoid the SNR drawback of 6 dB. FL locked in dissipative soliton mode realizes extremely high pulse energy and high peak for optical power [2, 3]. For example, fs pulses with a pulse energy as high as ~8.1 nJ was achieved by using a carbon-nanotube-based saturable absorber [4]. Such pulse energy is approximately 30 times that of the FL used in this thesis. As for the stability, a mode-locked FL oscillator that is close to shot noise level was reported [5]. However, such a FL has relatively low pulse energy (0.15 nJ) compared with that of the FL used here, thus leading to the need for strong optical amplification.

In conclusion, development of a FL that has picosecond duration, high power, and low noise is desirable.

(2)   *Wavelength tunability*

The wavelength tunability in this work is sufficient for covering the CH stretching vibration region (2850–3050 cm^{-1}). If we obtain tunability for a much broader wavelength, observation of another Raman band such as that of the OH stretching vibration region (3000–3400 cm^{-1}) is possible. In this work, the tunable FL suffers from the tradeoff between the wavelength tunability and the GDD compensation. This limitation may be avoided by employing external GDD compensation devices such as a grating compressor or a chirped fiber Bragg grating. Furthermore, optimizing the Yb-FL and polarization-maintaining Yb-doped fiber amplifier setups would extend the wavelength tunability to over 300 cm^{-1}. It seems difficult for a single-wavelength tunable Stokes pulse source to cover both CH and OH stretching vibration regions, but its combination with a tunable pump pulse source may allow access to both CH and OH bands. For example, such a tunable pump pulse may be achieved by using a periodically poled $LiNbO_3$ crystal with multiple periods [6–8].

76

Access to the fingerprint region (500–1800 cm^{-1}) is of interest, as it gives rich information on molecular vibrations. To access such a region, generating pump pulses in widely different wavelength regions is crucial.

(3) *Practicality of the laser system*

Even though the FL improves the practicality of SRS microscopy compared with that based on solid-state lasers, further improvement of the system's practicality is desirable. It remains complex; for instance, it requires synchronization between two FLs and bulky optics. Nonlinear interaction in optical fibers is a possible solution that simplifies the system. Indeed, several groups have reported pulse sources that generate two-color pulses from a single oscillator by using four-wave mixing [9], soliton self-frequency shift [10], and frequency doubling of a supercontinuum [6, 8]. It should be noted that CBD would be a key technology for achieving shot-noise-limited SNR when such single oscillators are used.

References

[1] M. Zirngibl, L. W. Stulz, J. Stone, J. Hugi, D. DiGiovanni, and P. B. Hansen, *Electron. Lett.* **27**, 1734 (1991).

[2] A. Chong, J. Buckley, W. Renninger, and F. Wise, *Opt. Express* **16**, 10095 (2006).

[3] W. H. Renninger, A. Chong, and F. W. Wise, *Phys. Rev. A* **77**, 023814 (2008).

[4] Y. Nozaki, N. Nishizawa, E. Omoda, H. Kataura, and Y. Sakakibara, *Opt. Lett.* **37**, 5079 (2012).

[5] J. Chen, J. W. Sickler, E. P. Ippen, and F. W. Kärtner, *Opt. Lett.* **32**, 1566 (2007).

[6] A. Gambetta, V. Kumar, G. Grancini, D. Polli, R. Ramponi, G. Cerullo, and M. Marangoni, *Opt. Lett.* **35**, 226 (2010).

[7] K. Nose, Y. Ozeki, T. Kishi, K. Sumimura, N. Nishizawa, K. Fukui, Y. Kanematsu, and K. Itoh, *Opt. Express* **20**, 13958 (2012).

[8] C. W. Freudiger, W. Yang, G. R. Holtom, N. Peyghambarian, X. S. Xie, and K. Q. Kie, *Nat. Photonics* **8**, 153 (2014).

[9] S. Lefrancois, D. Fu, G. R. Holtom, L. Kong, W. J. Wadsworth, P. Schneider, R. Herda, A. Zach, X. S. Xie, and F. W. Wise, *Opt. Lett.* **37**, 1652 (2012).

[10] E. R. Andresen, P. Berto, and H. Rigneault, *Opt. Lett.* **36**, 2387 (2011).

Appendix A:

Theoretical calculation of photonic RF spectral modulation by optical noise

A.1. Counterintuitive points in RF spectral modulation

As experimentally confirmed in Section 3.3, RF spectral modulation can be observed even when nonpolarized optical noise is used. Hence, there remain some counterintuitive points. In conventional spectral interferometry, identical states of polarization (SOPs) of the interfering lights are required. On the contrary, the SOP of light transmitted along the fibers changes because of residual birefringence of optical fibers. Since nonpolarized light is a group of wave packets with various SOPs, the SOPs of transmitted light are not always the same. Therefore, the following question arises: Why can the fringe be formed with nonpolarized amplified spontaneous emission (ASE) instead of polarized light? Moreover, why does the fringe have a visibility of ~0.5?

A.2. Analysis of the polarization states in the fiber delay line

We investigate the SOP of nonpolarized noises in the fiber delay line to determine why interference constantly occurs. We decompose the complex electric field vector of nonpolarized incident light $\boldsymbol{E}_{\text{in}}(t)$ in a single-mode fiber into two complex electric fields, $E_1(t)$ and $E_2(t)$, in mutually orthogonal SOPs:

$$\boldsymbol{E}_{\text{in}}(t) = E_1(t)\boldsymbol{V}_1 + E_2(t)\boldsymbol{V}_2, \qquad\qquad \text{(A-1)}$$

where $\boldsymbol{V}_1$ and $\boldsymbol{V}_2$ represent polarization states denoted by the Jones matrix notation. Here, $\boldsymbol{V}_1$ and $\boldsymbol{V}_2$ are chosen so that the following condition is satisfied: When the decomposed light is divided into two beams, which are then recombined after passage through different fiber paths, the beams have the same polarization. Thus, there exists a special set of SOPs for optical fibers. In the following calculation, propagation loss and polarization-dependent loss are neglected. Furthermore, it is assumed that the polarization mode dispersion is sufficiently small such that the frequency dependence of $\boldsymbol{V}_1$ and $\boldsymbol{V}_2$

is negligible in the bandwidth of the ASE.

To investigate the existence of the special set of SOPs represented by V_1 and V_2, let us consider how polarized light changes its polarization in the fibers. Figure A.1 shows a schematic model of our apparatus. For simplicity, lights transmitted from the short- and long-fiber arms are termed reference and signal, respectively. Denoting the Jones vectors of an arbitrary incident light, the reference, and the signal as V_{in}, V_{ref}, and V_{sig}, respectively, we may represent the Jones vectors of the transmitted lights as follows:

$$V_{ref} = \frac{1}{2} M_{ref} V_{in}, \tag{A-2}$$

$$V_{sig} = \frac{1}{2} M_{sig} V_{in}, \tag{A-3}$$

where M_{ref} and M_{sig}, which are Jones matrices of the reference and signal arms, respectively, are unitary. The factor 1/2 accounts for optical losses due to 3 dB couplers. If the SOPs of the transmitted lights are the same, then interference occurs. By using Eqs. (A-2) and (A-3), we can express this condition as follows:

$$M_{ref} V_{in} = \lambda M_{sig} V_{in}, \tag{A-4}$$

where λ is a constant. Equation (A-4) leads to

$$M_{sig}^{-1} M_{ref} V_{in} = \lambda V_{in}. \tag{A-5}$$

Equation (A-5) can be regarded as an eigenvalue equation. It gives two orthogonal eigenvectors and corresponding eigenvalues, since $M_{sig}^{-1} M_{ref}$ is also unitary. Therefore, λ_j $(j = 1, 2)$ can be defined as eigenvalues of Eq. (A-5). Note that $|\lambda_j| = 1$, because λ_j is the eigenvalue of the unitary matrix. When the eigenvectors in Eq. (A-5) are employed as the Jones vectors V_1 and V_2 in Eq. (A-1), the decomposed light is divided and recombined with the same polarization, as mentioned above.
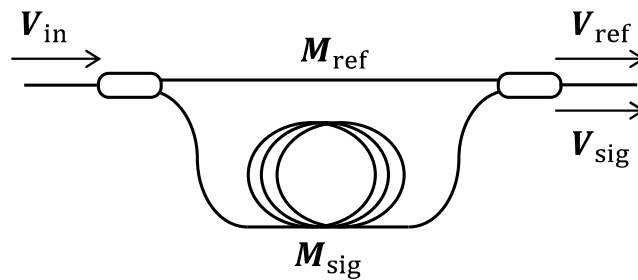

Fig. A.1. Schematic model of the analysis of the SOP in our apparatus.

A.3. Calculation of the photocurrent spectrum

To investigate how the RF spectrum is modulated, we obtained RF spectra of the photocurrents contributed by $E_1(t)$ and $E_2(t)$. Incident light is divided and recombined with the time delay difference τ. The electric field vector of the combined light is given by

$$\boldsymbol{E}'(t) = \frac{1}{2}\big[\boldsymbol{M}_{\text{ref}}\boldsymbol{E}_{\text{in}}(t) + \boldsymbol{M}_{\text{sig}}\boldsymbol{E}_{\text{in}}(t-\tau)\big]. \tag{A-6}$$

Substituting Eq. (A-1) into Eq. (A-6) and using the relationship expressed in Eq. (A-4), we can rewrite $\boldsymbol{E}'(t)$ with respect to $\boldsymbol{V}_1$ and $\boldsymbol{V}_2$:

$$\boldsymbol{E}'(t) = \frac{1}{2}\big\{[\lambda_1 E_1(t) + E_1(t-\tau)]\boldsymbol{M}_{\text{sig}}\boldsymbol{V}_1 \\ + [\lambda_2 E_2(t) + E_2(t-\tau)]\boldsymbol{M}_{\text{sig}}\boldsymbol{V}_2\big\}. \tag{A-7}$$

Thus, the complex amplitudes of the combined lights in each SOP are given by

$$E'_j(t) \propto \lambda_j E_j(t) + E_j(t-\tau). \tag{A-8}$$

Light is detected by the photodetector. The photocurrent is then given by

$$i_j(t) \propto \big|E'_j(t)\big|^2, \tag{A-9}$$

where the photocurrents contributed by $E_1(t)$ and $E_2(t)$ are denoted as $i_1(t)$ and $i_2(t)$, respectively. The Fourier transform of Eq. (A-9) gives the expression for the photocurrent spectrum, which can be described by autocorrelation of the spectrum of the combined light:

$$i_j(\omega) \propto \int E'_j(\Omega)E'^*_j(\Omega-\omega)d\Omega, \tag{A-10}$$

where $E'_j(\Omega)$ is the Fourier transform of the combined light, Ω is the angular optical frequency, ω is the angular RF frequency, and the symbol "*" denotes complex conjugation. The spectrum of the combined light can be obtained by Fourier transform of Eq. (A-8):

$$E'_j(\Omega) \propto E_j(\Omega)\{\lambda_j + e^{i\Omega\tau}\}, \tag{A-11}$$

where $E_j(\Omega)$ is the Fourier transform of $E_j(t)$. Substituting Eq. (A-11) into Eq. (A-10), we obtain the photocurrent spectrum from

$$i_j(\omega) \propto \int E_j(\Omega)E^*_j(\Omega-\omega) \\ \times \big[1 + \lambda^*_j e^{i\Omega\tau} + \lambda_j e^{-i(\Omega-\omega)\tau} + e^{i\omega\tau}\big]d\Omega. \tag{A-12}$$

APPENDIX A: Theoretical calculation of photonic RF spectral modulation by optical noise

From Eq. (A-9), the RF spectrum can be described as follows:

$$\left|\tilde{i}_j(\omega)\right|^2 \propto \int E_j(\Omega)E_j^*(\Omega-\omega)$$
$$\times\left[1+\lambda_j^* e^{i\Omega\tau}+\lambda_j e^{-i(\Omega-\omega)\tau}+e^{i\omega\tau}\right]d\Omega$$
$$\times\int E_j^*(\Omega')E_j(\Omega'-\omega) \tag{A-13}$$
$$\times\left[1+\lambda_j^* e^{i\Omega'\tau}+\lambda_j e^{-i(\Omega'-\omega)\tau}+e^{i\omega\tau}\right]^* d\Omega'.$$

Since Eq. (A-13) is the product of integrals, we can expand it to quadratic terms at the same frequency and cross terms between different frequencies. Note that there is no correlation among different frequency components because we use an optical-noise source. Therefore, the cross terms reach zero and only the quadratic terms remain. Exponential terms including Ω are zero in the integration with respect to Ω. As a result, the RF spectra of the photocurrents are given by

$$\langle\left|i_j(\omega)\right|^2\rangle \propto (2+\cos\omega\tau)$$
$$\times\int\langle\left|E_j(\Omega)\right|^2\rangle\langle\left|E_j(\Omega-\omega)\right|^2\rangle\,d\Omega\,, \tag{A-14}$$

which implies that the visibility is 0.5 and that the RF spectrum is modulated by a cosine function, the period of which is inversely proportional to τ.

A.4. Interpretation of the calculation results

When $E_1'(t)$ and $E_2'(t)$ are simultaneously detected by a photodetector, the RF spectrum of the photocurrent is simply the sum of the RF spectra expressed in Eq. (A-14). This point is explained as follows. Since there is no optical interference between $E_1'(t)$ and $E_2'(t)$, the resultant photocurrent is the sum of $i_1(t)$ and $i_2(t)$. Furthermore, there is no correlation between $i_1(t)$ and $i_2(t)$ because the noises expressed as $E_1'(t)$ and $E_2'(t)$ are independent of each other. Therefore, the power spectrum of the total photocurrents is simply the sum of the power spectra of each photocurrent. If any change is induced in the state of optical fibers, there are corresponding changes in Jones matrices and eigenvectors. Therefore, we can decompose the ASE with the changed eigenvectors to show that the RF fringe is expressed by Eq. (A-14). This is why the RF spectrum is

modulated to a visibility of 0.5 regardless of the polarization state of the transmitted light. Note that the resolution bandwidth of the RF spectrum analyzer and the bandwidth of the tunable optical band pass filter are not involved. These parameters affect the amplitude and signal-to-noise ratio of the RF modulation fringe. of This point will be further analyzed in future work.

Appendix B:

Mathematical description of dispersion compensation using the spectral filter

In Chapter 5, we show that the optical band-pass filter (OBPF) can also be used to compensate for group delay dispersion (GDD). Here, the amount of GDD given by the OBPF is calculated by referring to Fig. B.1. The focal point on the optical axis of the latter lens in the 4-f system is denoted as the origin (O). The cross point between the incident beam and the shifted grating plane is denoted as P. When the incident angle is θ_i, the path length $\overline{OP}$ is represented as $l(\theta_i)$, which is given by

$$l(\theta_i) = \sqrt{x^2 + y^2} = \frac{1}{(1 - \tan\theta_i\tan\theta_g)\cos\theta_i}\Delta x, \tag{B-1}$$

where Δx is the displacement of the grating, and θ_g is the angle between the optical axis of the lens and the normal of the grating plane. When the incident angle is slightly changed, the amount of change in path length is given by

$$\frac{dl}{d\theta_i} = \frac{(\tan\theta_i + \tan\theta_g)}{(1 - \tan\theta_i\tan\theta_g)^2 \cos\theta_i}\Delta x. \tag{B-2}$$

From the grating equation, the relation between the Littrow wavelength (λ_L) and the incident angle (θ_i) is given by

$$2d\sin(\theta_i + \theta_g) = m\lambda_L, \tag{B-3}$$

where d is the grating constant and m is the diffraction order. Since the first-order diffraction beam is used in this work, $m = 1$ is employed. By employing the chain rule for Eq. (B-2) and the $d\theta_i/d\lambda_L$ obtained from Eq. (B-3), the relation between the path length and the Littrow wavelength is given by

$$\frac{dl}{d\lambda_L} = \frac{dl}{d\theta_i}\frac{d\theta_i}{d\lambda_L} = \frac{\tan\theta_i + \tan\theta_g}{2d(1 - \tan\theta_i\tan\theta_g)^2 \cos\theta_i \cos(\theta_i + \theta_g)}\Delta x. \tag{B-4}$$

Note that the propagation length is quadruple of that obtained by using Eq. (B-4) because of the forward and backward propagations and the double-pass configuration. Assuming that the incident angle is very small ($|\theta_i| \ll 1$), we obtain the amount of GDD from

$$\frac{\mathrm{d}\tau}{\mathrm{d}\lambda_{\mathrm{L}}} = \frac{4}{c}\frac{\mathrm{d}l}{\mathrm{d}\lambda_{\mathrm{L}}} \sim \frac{2\tan\theta_{\mathrm{g}}}{cd\cos\theta_{\mathrm{g}}}\Delta x, \tag{B-5}$$

where τ and c are the group delay and speed of light in vacuum. In our case, we used a grating for which $d = 1/1200$ mm. The angle of the grating was $\theta_{\mathrm{g}} = 0.67$ rad. The GDD per unit displacement $(1/\Delta x)(\mathrm{d}\tau/\mathrm{d}\lambda_{\mathrm{L}})$ was found to be 8.0 ps/nm/m.
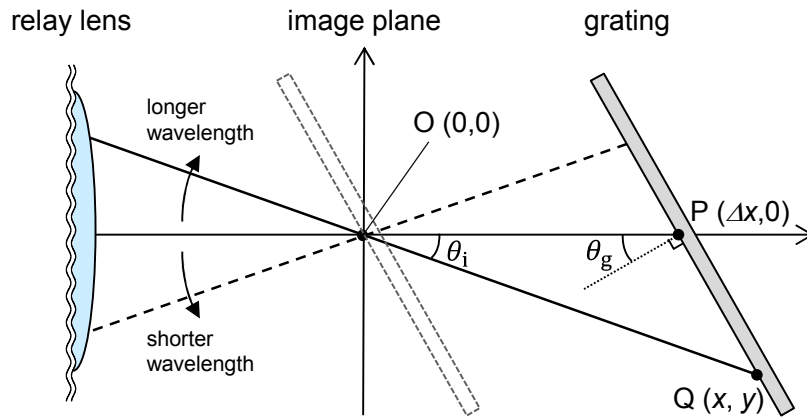

Fig. B.1. Geometrical arrangement near the grating in the OBPF.

Appendix C:

The relation of pulse duration and its bandwidth

Theoretically, the bandwidth of optical pulses is related to the duration of the pulses and their temporal phase. By assuming for simplicity that the temporal phase is constant, the relationship between the duration and the bandwidth is explained mathematically.

The electric field of the optical pulse is denoted as follows:

$$E(t) = A(t)e^{-i(\omega_0 t - \phi(t))} = A(t)e^{i\Phi(t)}, \tag{C-1}$$

where $A(t)$ is the temporal amplitude of the optical pulse, ω_0 is the center angular frequency, and $\Phi(t)$ is the temporal phase. The pulse duration Δt is defined as the full width at half-maximum (FWHM) of the intensity, $I(t) = |A(t)|^2$.

The Fourier transform of Eq. (C-1) gives the spectrum of the pulse:

$$E(\omega) = \int_{-\infty}^{\infty} E(t)e^{i\omega t}dt = A(\omega)e^{i\psi(\omega)}, \tag{C-2}$$

where $A(\omega)$ is the spectral amplitude function and $\psi(\omega)$ is the spectral phase function. The bandwidth Δv is defined as the FWHM of its power spectrum $S(\omega) = |A(\omega)|^2$. The product between the time duration and the bandwidth is given by

$$\Delta t \Delta v \geq \text{const.} \tag{C-3}$$

The constant is approximately 1 and is dependent on the envelope function of the pulse. When the spectral phase $\psi(\omega)$ is fixed over the entire spectrum, termed as the Fourier transform limited, the minimum pulse duration is reached.

For example, an ideal Gaussian pulse, i.e., its temporal phase, is constant. The temporal amplitude is given by

$$A(t) = A_0 e^{-\frac{1}{2}\left(\frac{t}{\tau}\right)^2}, \tag{C-4}$$

where A_0 and τ are the amplitude and time constant of the envelope, respectively. In accordance with the definition given above, the pulse width is given by

$$\Delta t = 2\sqrt{\ln 2}\, \tau. \tag{C-5}$$

The spectral amplitude is given by the Fourier transform of Eq. (C-4):

$$\tilde{A}(\omega) = \int_{-\infty}^{\infty} A(t)e^{-i\omega t} = \sqrt{2\pi}\tau A_0 e^{-\frac{(\tau\omega)^2}{2}}. \tag{C-6}$$

Thus, the spectral width is also given by

$$\Delta\nu = \frac{\Delta\omega}{2\pi} = \frac{1}{\pi}\left(\frac{\sqrt{\ln 2}}{\tau}\right). \tag{C-7}$$

Upon substitution of Eqs. (C-6) and (C-7) into Eq. (C-3), the time–bandwidth product of Gaussian pulse is 0.441. When the envelope function is $\mathrm{sech}(t)$, as is in the case of optical soliton in fibers, the time-bandwidth product is 0.315. Gaussian pulses and soliton pulses are typical waveforms in fiber lasers.

Publication list

Original papers

[1] <u>Keisuke Nose</u>, Yasuyuki Ozeki, Tatsuya Kishi, Kazuhiko Sumimura, Norihiko Nishizawa, Kiichi Fukui, Yasuo Kanematsu, and Kazuyoshi Itoh, "Sensitivity enhancement of fiber-laser-based stimulated Raman scattering microscopy by collinear balanced detection technique," Optical Express, Vol. 20, No. 13, 13958–13965 (2012).

[2] <u>Keisuke Nose</u>, Tatsuya Kishi, Yasuyuki Ozeki, Yasuo Kanematsu, Hideaki Takata, Kiichi Fukui, Yoshizo Takai, and Kazuyoshi Itoh, "Stimulated Raman spectral microscope using synchronized Er- and Yb-fiber lasers," Japanese Journal of Applied Physics, Vol. 53, No. 5, 052401 (2014).

[3] <u>Keisuke Nose</u>, Yasuyuki Ozeki, Yasuo Kanematsu, Yoshizo Takai, and Kazuyoshi Itoh, "RF spectral modulation caused by delayed interference and photodetection of optical noise," Optical Review, Vol. 21, No. 4, 425–428 (2014).

Co-author

[1] Yasuyuki Ozeki, Tatsuya Kishi, <u>Keisuke Nose</u>, and Kazuyoshi Itoh, "Real-time stimulated Raman scattering microscopy using fiber-laser sources," The Review of Laser Engineering, Vol. 41, No. 8, 619–621, (2012). (in Japanese)

Patent list

Domestic

[1] 小関泰之，伊東一良，能勢啓輔，"ラマン散乱計測装置および誘導ラマン散乱検出方法，" 特願 2013-540135 号，特開 2014-507627，（出願中）.

[2] 小関泰之，伊東一良，能勢啓輔，"ラマン散乱計測装置およびラマン散乱計測方法，" 特願 2013-046362 号，特開 2014-173973（出願中）.

International

[1] Yasuyuki Ozeki, Kazuyoshi Itoh, Keisuke Nose. 2012. Stimulated Raman scattering detection apparatus. U.S. Patent Application 20140043606, filed March 2, 2012, and issued February 13, 2014.

[2] Yasuyuki Ozeki, Kazuyoshi Itoh, Keisuke Nose. 2014. Raman scattering measuring apparatus and Raman scattering measuring method. U.S. Patent Application 20140253918, filed March 6, 2014, and issued September 11, 2014.

Presentations at international conference

[1] <u>Keisuke Nose</u>, Yasuyuki Ozeki, and Kazuyoshi Itoh, "Development of pulsed fiber laser sources for stimulated Raman scattering microscopy," 4th international symposium on atomically controlled fabrication technology, P21, Osaka, Japan (November 2011).

[2] <u>Keisuke Nose</u>, Yasuyuki Ozeki, Tatsuya Kishi, Kazuhiko Sumimura, Norihiko Nishizawa, Yasuo Kanematsu, and Kazuyoshi Itoh, "Sensitivity enhancement of fiber-laser-based stimulated Raman scattering microscopy by intensity noise suppressor," Conference on Lasers and Electro Optics (CLEO), JW3G.6, San Jose, USA (May 2012).

[3] <u>Keisuke Nose</u>, Yasuyuki Ozeki, and Kazuyoshi Itoh, "A fiber-laser-based stimulated Raman scattering microscope," Fifth International Symposium on Atomically Controlled Fabrication Technology, P96, Osaka, Japan (October 2012).

[4] <u>Keisuke Nose</u>, Yasuyuki Ozeki, Tatsuya Kishi, Kazuhiko Sumimura, Yasuo Kanematsu, and Kazuyoshi Itoh, "A fiber-laser-based stimulated Raman scattering spectral microscope," Photonics West BiOS, 8588-35, San Francisco, USA (February 2013).

[5] <u>Keisuke Nose</u>, Tasuya Kishi, Yasuyuki Ozeki, Yasuo Kanematsu, and Kazuyoshi Itoh, "Extended wavelength tunability of a picosecond pulse source by double-pass spectral filter for fiber-laser-based stimulated Raman spectral microscopy," Conference on Lasers and Electro Optics (CLEO), CTu2M.1, San Jose, USA (June 2013).

[6] <u>Keisuke Nose</u>, Tatsuya Kishi, Yasuyuki Ozeki, Yasuo Kanematsu, and Kazuyoshi Itoh, "Fiber-laser-based stimulated Raman microspectroscopy with shot-noise limited sensitivity," The 10th conference on Lasers and Electro-Optics Pacific Rim (CLEO-PR), TuF4-2, Kyoto, Japan (July 2013).

[7] Yasuyuki Ozeki, <u>Keisuke Nose</u>, and Kyoya Tokunaga, "Group delay compensation of spectrally-filtered picosecond pulses for stimulated Raman microscopy," Conference on Lasers and Electro Optics (CLEO), JTh2A.30, San Jose, USA (June 2014).

90

Presentations at domestic conference

[1] 能勢啓輔, 小関泰之, 兼松泰男, 伊東一良, "光雑音の遅延干渉による光電流スペクトル変調とその群遅延測定への応用," 第 71 回 応用物理学会学術講演会, 14p-NK-15, 長崎, 2010 年 9 月.

[2] 能勢啓輔, 小関泰之, 住村和彦, 西澤典彦, 兼松泰男, 伊東一良, "強度雑音スペクトル整形によるファイバーレーザーの雑音低減," 第 58 回 応用物理学関係連合講演会, 24p-KG-6, 神奈川, 2011 年 3 月.

[3] 能勢啓輔, 小関泰之, 岸達也, 住村和彦, 兼松泰男, 伊東一良, "誘導ラマン散乱顕微法のためのピコ秒パルスファイバーレーザーの高調波同期," 第 72 回 応用物理学会学術講演会, 山形, 30p-ZH-9, 2011 年 8 月.

[4] 能勢啓輔, 小関泰之, 岸達也, 住村和彦, 西澤典彦, 兼松泰男, 伊東一良, "同軸型バランスド検出法と高調波同期法を用いたファイバーレーザーベース誘導ラマン散乱顕微鏡," 第 59 回 応用物理学関係連合講演会, 6p-B9-13, 東京, 2012 年 3 月.

[5] 能勢啓輔, 小関泰之, 岸達也, 兼松泰男, 伊東一良, "ファイバーレーザー誘導ラマン散乱顕微鏡のためのファイバー遅延線による同軸型バランス検出法," 第 73 回応用物理学会学術講演会, 14a-B2-1, 松山, 2012 年 9 月.

[6] 岸達也, 能勢啓輔, 小関泰之, 兼松泰男, 伊東一良, "誘導ラマン散乱顕微鏡用ファイバー光源におけるパルスの高強度化と雑音特性の検討," Optics & Photonics Japan 2012 (OPJ 2012), 25aA6, 東京, 2012 年 10 月.

[7] 能勢啓輔, 小関泰之, 岸達也, 住村和彦, 兼松泰男, 伊東一良, "ファイバー光源による誘導ラマン散乱分光顕微鏡," Optics & Photonics Japan 2012 (OPJ 2012), 25aA7, 東京, 2012 年 10 月.

[8] 能勢啓輔，小関泰之，岸達也，兼松康男，伊東一良，"ダブルパス型フィルターの適用による誘導ラマン分光顕微鏡用ピコ秒パルス光源の波長可変域拡大，" 第 60 回応用物理学会春季学術講演会，29a-A2-1，東京，2013 年 3 月.

[9] 徳永京也，能勢啓輔，小関泰之，"誘導ラマン分光顕微鏡用波長可変パルス光源の強度安定化，" 第 74 回応用物理学会秋季学術講演会，17p-C1，京都，2013 年 9 月.

Acknowledgements

I would like to express my gratitude to Professor Kazuyoshi Itoh at Graduate School of Engineering, Osaka University for his kind guidance, helpful suggestions and constant encouragement throughout this study.

My gratitude also goes to Professor Yoshizo Takai at Graduate School of Engineering, Osaka University for his constructive comments, helpful suggestions, and warm encouragement.

I truly appreciate the valuable feedback throughout this study offered by Professor Yasuo Kanematsu at Graduate School of Engineering, Osaka University.

I would like to express my sincere appreciation to Professor Heiji Watanabe at Graduate School of Engineering, Osaka University for his careful reviewing of this thesis and valuable suggestions.

Similarly, I also appreciate Professor Norihiko Nishizawa at Graduate School of Engineering, Nagoya University for his valuable suggestions and helpful comments.

I would like to express profoundly grateful to my research adviser, Associate Professor Yasuyuki Ozeki at Graduate School of Engineering, The University of Tokyo for his guidance, advice, and continuous encouragement in my daily study during my 5 years. What I have learned under his direction will be invaluable to me throughout my life.

I am heartily grateful to Associate Professor Tsuyoshi Konishi and Yoshihide Kimura at Graduate School of Engineering, Osaka University for their helpful comments and suggestions.

Similarly, I am also grateful to Professor Kiichi Fukui and Assistant Professor Hideaki Takata for providing living samples and their helpful comments.

I appreciate Professor Kazuro Kikuchi and Assistant Professor Kazuhiro Katoh for taking time to give me useful suggestions and helpful advices.

Special thanks to all the members of Itoh laboratory, Kikuchi/Ozeki laboratory, and Takai laboratory for their help, valuable suggestions, and kindly friendship. There are not enough words to express how grateful I am to you all.

I am also grateful to the Global COE program "Center of Excellence for Atomically Controlled Fabrication Technology" for their support through scholarships.

Finally, I would like to sincere acknowledgement my friends and family for their continuous encouragement and support.